

**Safety Factor Against Burst Speed Of Turbomachinery
Rotating Disks**

BY

STEFANO CHIANESE

B.S., Politecnico di Torino, Turin Italy, October 2011

THESIS

Submitted as partial fulfillment of the requirements
for the degree of Master of Science in Mechanical Engineering
in the Graduate College of the
University of Illinois at Chicago, 2013

Chicago, Illinois

Defense Committee:

Thomas Royston, Chair and Advisor

Ahmed Shabana

Muzio Gola, Politecnico di Torino

ACKNOWLEDGMENTS

I would like to spend few words to thank the people that made this thesis become real.

First of all I acknowledge the great role of my advisor, prof. Muzio Gola, for being such a great teacher, for inspiring me in the field of machine design and for having proposed me this research thesis.

I want also to express my gratitude to all the people that assisted me during the period in which I worked on this thesis: Dr. Christian Maria Firrone, which guided the whole research with great experience; Nicola Squarcella, that helped me in learning the software; and the Avio group, and in particular Ing. Marco Allara, commissioner of this research, which continuously invest on young people and very interesting research fields.

A last word, finally, goes to my family and all my friends who always encouraged and supported me during these hard years of study.

SC

TABLE OF CONTENTS

<u>CHAPTER</u>		<u>PAGE</u>
1	INTRODUCTION	1
2	THE PROBLEM OF DISK BURST	6
2.1	Rotating disks: loading conditions	6
2.2	Materials	9
2.3	Types of failure	13
2.4	International standars for rotor integrity	18
2.5	Finite Elemet Method	20
3	CONSTITUTIVE EQUATIONS OF ROTATING DISKS	23
3.1	Equation of equilibrium	25
3.2	Strain-Displacement relations	30
3.3	Elastic field: Hooke's law	32
3.4	Thermal expansion term	33
3.5	Equations for disks in the elastic field	34
3.5.1	Rotating disks of constant thickness	34
3.5.2	Rotating disks of variable thickness	37
3.6	Plastic field models	38
3.6.1	Elastic perfectly plastic model	41
3.6.2	Ramberg-Osgood model	43
3.7	Equations for annular disks in the plastic field (constant thick- ness)	45
3.8	Failure criteria for rotating disks	50
3.8.1	Robinson Criterion	50
3.8.2	Critical strain criterion (inertial instability)	52
4	FINITE ELEMENT MODEL USING ANSYS	55
4.1	The finite element method general formulation	55
4.2	Setup of a finite element analysis using Ansys	58
4.2.1	Preprocessing: model generation and mesh properties	58
4.2.2	Processing: load increasing simulations	60
4.3	Elasto-plastic calculations in Ansys	63
5	COMPUTATION OF INERTIAL INSTABILITY OF ROTAT- ING DISKS	73
5.1	Rotating beam with tip mass	75
5.2	Rotating disk of uniform thickness	80

TABLE OF CONTENTS (continued)

<u>CHAPTER</u>		<u>PAGE</u>
6	COMPARISON BETWEEN TWO-DIMENSIONAL AND THREE-DIMENSIONAL MODELS	86
6.1	Two-dimensional model	87
6.2	Three-dimensional model	88
6.3	Finite element analysis of the burst limit	92
6.3.1	Small displacement simulations	93
6.3.2	Large displacement analysis	99
6.4	Comparison with Robinson's criterion	110
7	THREE-DIMENSIONAL MODEL WITH HOLES	116
7.1	Model description	116
7.2	Burst speed analyses	119
7.2.1	Variation of the number of holes	119
7.2.2	Variation of the holes dimension	133
8	EQUIVALENT TWO-DIMENSIONAL MODEL FOR HOLED DISKS	148
8.1	Model description: geometry and material properties	149
8.2	Burst limit comparison with the 3D model and the Robinson's criterion	151
9	CONCLUSIONS AND FURTHER DEVELOPMENTS	160
	CITED LITERATURE	164
	VITA	166

LIST OF TABLES

<u>TABLE</u>		<u>PAGE</u>
I	ROTOR INTEGRITY CONDITIONS	19
II	CRITICAL VALUES OF K VS MASS RATE	78
III	INSTABILITY BURST SPEED OF A ROTATING BEAM: COM- PARISON BETWEEN ANALYTIC AND NUMERIC RESULTS . .	80
IV	INSTABILITY BURST SPEED OF A ROTATING DISK: COM- PARISON BETWEEN ANALYTIC AND NUMERIC RESULTS . .	85
V	SMALL DISPLACEMENT ANALYSIS: BURST SPEED	95
VI	VARIATION OF BURST SPEED	101
VII	COMPARISON BETWEEN MEAN REAL CURVE AND WORST OCCURRENCE	109
VIII	BURST SPEED CALCULATED USING ROBINSON FOR REAL CURVES	114
IX	VARIATION OF BURST SPEED WITH THE NUMBER OF HOLES - CURVE 1	121
X	VARIATION OF BURST SPEED WITH THE NUMBER OF HOLES - CURVE 2	125
XI	VARIATION OF BURST SPEED WITH THE NUMBER OF HOLES - REAL CURVE	129
XII	VARIATION OF BURST SPEED WITH HOLES DIMENSION - REAL CURVE	134
XIII	BURST SPEED FOR HOLED DISKS USING ANSYS 2D, ANSYS 3D AND ROBINSON'S CRITERION	153

LIST OF FIGURES

<u>FIGURE</u>		<u>PAGE</u>
1	Turbojet engine	1
2	Disk burst on a Qantas A380	2
3	Rotor disk burst on an American Airlines Boeing 787	4
4	Cross-section view of a turbofan engine	7
5	Temperature and pressure profiles inside a turbo engine	10
6	Principal kind of materials used in a turbo engine	11
7	Variation of the specific strength of metal alloys as temperature changes	12
8	Example of a turbine disk	13
9	Fracture modes	15
10	Propagation of Lüders' bands into a notched disk	17
11	Comparison of burst between notched and unnotched disk	17
12	Plane stress vs plane strain	24
13	Axisymmetric disk under axisymmetric load	26
14	Infinitesimal element on a disk	27
15	Local cartesian axes	28
16	Stresses on the infinitesimal element	28
17	Equilibrium	29
18	Radial displacement	31
19	Annular disk	36

LIST OF FIGURES (continued)

<u>FIGURE</u>		<u>PAGE</u>
20	Typical material behaviours	40
21	EPP material compared to hardening material	42
22	Stress-strain curve and offset line using Ramberg-Osgood model	45
23	Partially plasticized disk	47
24	True stress versus engineering stress	51
25	Loading sequence and division in substeps	62
26	Newton-Raphson method vs arc length method	63
27	Update of the matrix $[K]$ at each iteration	65
28	Yield criteria	66
29	Models for updating σ_0	68
30	Amplification of the allowable ellipse due to cumulated plastic deformation	69
31	Update of the yielding surface	71
32	Plastic deformations prior to fracture	74
33	View of the fracture surface of a disk showing evident necking	74
34	Divergence of stresses for varying k and mass rates	77
35	Ansys model for the rotating beam with mass on tip	79
36	Comparison between analytic and numeric results	79
37	Divergence of stresses for different Ω and geometry rates	83
38	Comparison between Ansys results and analytic model: LD option	84
39	Comparison between Ansys results and analytic model: KSPIN option	85
40	<i>Plane42</i> element	87

LIST OF FIGURES (continued)

<u>FIGURE</u>		<u>PAGE</u>
41	Bidimensional model	88
42	Basic Sector	89
43	Elements used in the three-dimensional case	90
44	Three-dimensional model mesh	91
45	Three-dimensional: lines and boundary condition	92
46	Bi-linear material curves used in the SD analysis	94
47	Comparison of principal stresses tendencies before burst (SD)	95
48	Comparison of equivalent stresses tendencies before burst (SD)	96
49	Contour plots of the principal stresses, SD analysis	97
50	Loading evolution of the σ_{eq}	98
51	Bi-linear material curves used in the LD analysis	100
52	Burst speed trend as function of ε_{UTS}	101
53	Comparison of principal stresses tendencies before burst (LD)	102
54	Comparison of equivalent stresses tendencies before burst (LD)	103
55	Comparison of the equivalent stresses in loading for curve 2 and curve 5 (LD)	104
56	Displacements at rim for curve 5	106
57	Experimental material curve with variation ranges	107
58	Mean curve and modified curve	108
59	Displacement at the rim for real material curves	109
60	Equilibrium on a half-disk	111
61	Displacements at rim for the different curves compared with Robinson	113

LIST OF FIGURES (continued)

<u>FIGURE</u>		<u>PAGE</u>
62	Displacements at rim for real curves compared with Robinson	115
63	Basic sector with the hole: volume division	118
64	Mesh of the holed disk	118
65	Bi-linear material curves	120
66	Variation of burst speed with the number of holes (curve 1)	122
67	Comparison of equivalent stresses before burst (curve 1, path 1)	123
68	Comparison of equivalent stresses before burst (curve 1, path 2)	124
69	Variation of burst speed with the number of holes (curve 2)	126
70	Comparison of equivalent stresses before burst (curve 2, path 1)	127
71	Comparison of equivalent stresses before burst (curve 2, path 2)	127
72	Mean real material curve	128
73	Variation of burst speed with the number of holes (real curve)	130
74	Comparison of equivalent stresses before burst (real curve, path 1)	131
75	Comparison of equivalent stresses before burst (real curve, path 2)	132
76	Evolution of equivalent stress in loading (5 holes, real curve)	133
77	Comparison of equivalent stress before burst as dimension of holes varies (12 holes, path 1)	135
78	Comparison of equivalent stress before burst as dimension of holes varies (12 holes, path 2)	135
79	Principal stresses along path 1 for varying holes dimensions (12 holes)	137
80	Circumferential path	138
81	Disk with 5 holes of 10mm diameter	139

LIST OF FIGURES (continued)

<u>FIGURE</u>		<u>PAGE</u>
82	Comparison of stresses along different paths (5 holes, $d = 10\text{ mm}$) . . .	139
83	Disk with 5 holes of 30 mm diameter	140
84	Comparison of stresses along different paths (5 holes, $d = 30\text{ mm}$) . . .	140
85	Disk with 5 holes of 50 mm diameter	141
86	Comparison of stresses along different paths (5 holes, $d = 50\text{ mm}$) . . .	141
87	Disk with 12 holes of 10 mm diameter	142
88	Comparison of stresses along different paths (12 holes, $d = 10\text{ mm}$) . . .	142
89	Disk with 12 holes of 30 mm diameter	143
90	Comparison of stresses along different paths (12 holes, $d = 30\text{ mm}$) . . .	143
91	Disk with 12 holes of 50 mm diameter	144
92	Comparison of stresses along different paths (12 holes, $d = 50\text{ mm}$) . . .	144
93	Deformed and undeformed shapes	145
94	Contour plot of the equivalent stress: disk with 36 holes ($d = 50\text{ mm}$) .	146
95	Contour plot of the equivalent stress: disk with 12 holes ($d = 50\text{ mm}$) .	147
96	Bi-dimensional model with orthotropic material in the holes region . .	149
97	Comparison 2D model vs 3D model	154
98	Stress along the radius - 2D model (5 holes, $d = 30\text{ mm}$)	155
99	Stress paths along the radius - 3D model (5 holes, $d = 30\text{ mm}$)	156
100	Comparison Robinson vs 3D model	157

LIST OF ABBREVIATIONS

DIMEAS	Department of Mechanical and Aerospace Engineering
EASA	European Aviation Safety Agency
FAA	Federal Aviation Administration
FAR	Federal Aviation Regulation
CS-E	Certification Specifications for Engines
OEI	One Engine Inoperative
FEM	Finite Element Method
FE	Finite Element
NACA	National Advisory Committee for Aeronautics
EPP	Elastic Perfectly Plastic
DTIC	Defense Technical Information Center
UTS	Ultimate Tensile Strength
SD	Small Displacement
LD	Large Displacement.

SUMMARY

This thesis work was performed within the “AERMEC” and the “GreatLab” laboratories of Politecnico di Torino.

The Great Lab works in collaboration with Avio S.p.A in order to develop new aeronautical engines for civil transportation within the project GREAT 2020, which aims to meet the requirements established by the European committee for Horizon 2020, in order to reduce emissions and produce more efficient and environmentally friendly engines.

The objective of this thesis is the study of burst speed of turbomachinery rotating disks, considering the presence of non-axisymmetry in them.

In particular, this work is focusing on the certification against burst used in the design of rotating disks, which are among the most stressed parts in a aeronautic turbine.

The first part of the work presents the theory of rotating disks and the current practice used by Avio and most of the competitors in order to validate the rotor against burst speed. In the second part of the thesis, the numerical models developed during this work are presented. The idea is to perform elasto-plastic analysis in order to consider the effect of large deformations and the plastic behavior of materials when studying the burst. This leads to the validation of the use of a numerical method to find the burst limit based upon the hypothesis of inertial instability of rotating disks.

CHAPTER 1

INTRODUCTION

Most modern airplanes are equipped with air-breathing turbo-engines that guarantee high performance at relatively acceptable costs. A typical kind of air-breathing turbo-engine is, for example, the *Turbojet engine* (Figure 1) which is made by a compressor, a combustor, a turbine and an exhaust nozzle. Air is compressed in the compressor, then combustion occurs into the combustion chamber, and finally hot gasses are expanded into the turbine stages and expelled through the nozzle to produce thrust.^[1]

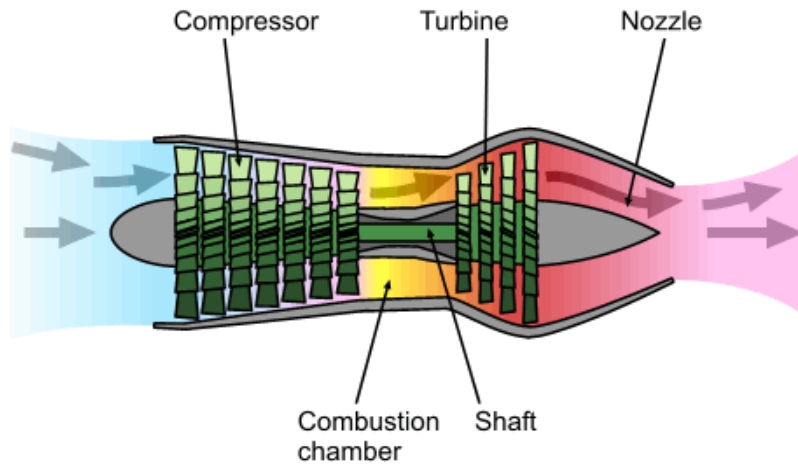


Figure 1: Turbojet engine

Turbines, are among the most stressed components of the entire engine: they suffer very high stresses due to temperature gradient (hot gasses coming from the combustor and very low external temperatures), corrosive environment (combusted gasses) and high rotational speed.

The object of the study done in the present thesis work are the turbomachinery rotating disks which are in charge to carry the blades invested by the fluid and to transmit the power to the shaft. In particular the research is focused on the prediction of the maximum angular velocity that those disks can suffer before failing because of burst.

Rotor burst is one of the most important issues to care about whenever it comes to design a turbomachinery disk: the consequences of a failure can, in fact, be dramatic, since the disk disintegrates into multiple pieces and they are flung away in all the direction at very high speed.



Figure 2: Disk burst on a Qantas A380

The problem with the burst of a rotating disk is that the pieces in which it breaks have huge inertia: they can destroy the engine and, eventually, pass through the nacelle (as it is possible to see in Figure 2 and Figure 3).

Prevent turbine disks from failure in *overspeed conditions* is, for this reason, one of the key-point of the safety certifications from both EASA in Europe and FAA in the US. Those certifications ask to test the failure of the rotor disk considering it as separated from the rest of the turbine system and to find the maximum velocity that satisfy their requirements. For this reason the bust study is conducted on a single disk in rotation around its axis.

The innovative approach proposed in this research is to consider the real behavior of the material and validate a consistent model in which plastic deformations are taken into account. The numerical model implemented in Ansys, then, has been built in order to consider the large displacement related to the plastic deformations and simulate the real behavior at burst of a rotating disk.

The validation of such a numerical model passes through the study of the theory of rotating disks and a brief description of the *Finite Element Method*.

Previous works^[2] were focused on the validation of a bi-dimensional model for axisymmetric disks, using a planar description with elements that consider the symmetry around the rotational axis, and justifying the results obtained performing the FEM analysis with the condition

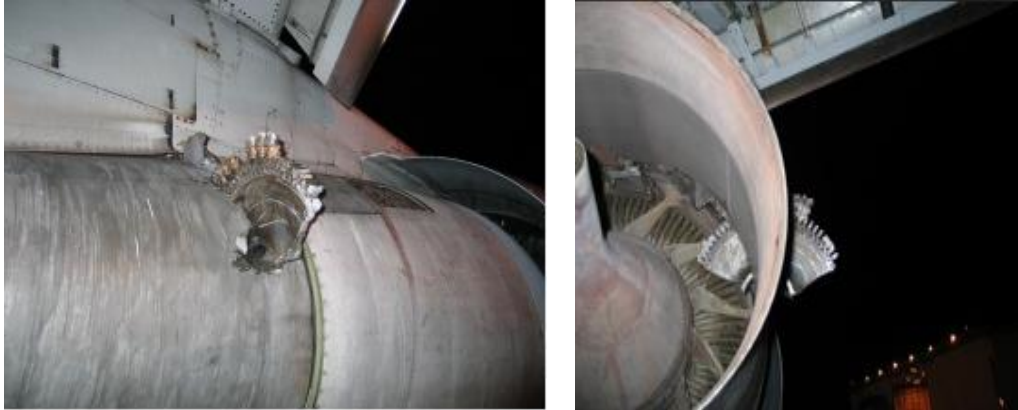


Figure 3: Rotor disk burst on an American Airlines Boeing 787

of inertial instability that is causing the divergence of the numerical results at burst.

The object of the discussion presented in this thesis is, instead, to deeply analyze the burst conditions of non-axisymmetric disks focusing on failures in the *hoop mode*. Those simulations need the definition of a three-dimensional model, so, only after that it has been proved that this kind of model gives consistent results, the study will be focused on holed disks, comparing again the results obtained with those given by the analytic formula.

Different geometrical models are going to be implemented in the numerical code in order to evaluate the maximum angular velocity that different disks can withstand before failing and to compare those results with those obtained using the analytic formula that is currently adopted (with very little corrections) by many companies in the aerospace industries. Thus, the limits of this current practice are going to be highlighted, discussing whether the use of a Finite Element

might be more accurate and a preferable choice when designing rotating disks.

Finally, since the Finite Element analysis of three-dimensional structures is much more time demanding than the one performed in two-dimensions, the aim of the research is also to provide a valid alternative solution that allows to consider the presence of holes also in the two-dimensional model of the disk. In this way it might be possible to perform a much faster study without having to model a complex body, with reasonably accurate results.

CHAPTER 2

THE PROBLEM OF DISK BURST

This chapter presents a general overview on the turbine rotor disks in order to outline the main reasons that foster the research in this field, focusing mainly on the different loading conditions, on the materials and on the limiting conditions that rotor disks have to tolerate in order to satisfy the international standards.

A brief introduction to the use of finite elements codes, finally, is shown in order to consider the pros and the cons of this kind of numerical simulation, while the actual presentation of the non linear analysis is done later on in this thesis.

2.1 Rotating disks: loading conditions

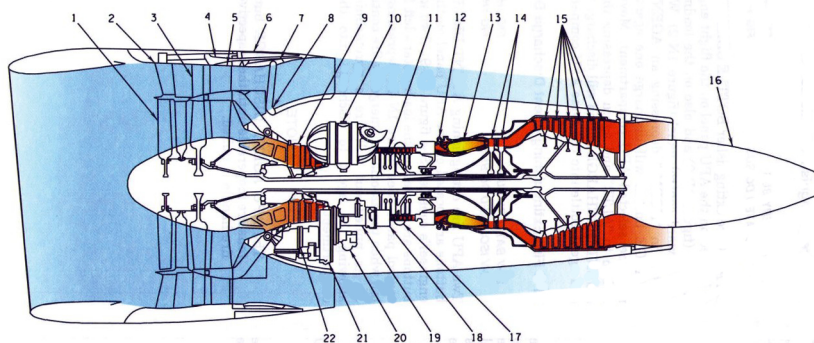
Rotating disks are very common rotating devices used both in compressors and turbines to transmit power between the shaft and the blades. They can be used at very high speed, especially when used in turbines, so that it is possible to produce more power or greater centrifugal fields.

The mechanical stresses they suffer depend on the particular working conditions and not all of them are related to the angular velocity. Loads affected by rotational speed are all the inertia forces: centrifugal field, gyroscopic moments and angular acceleration; while axial loads, torque and fitting loads are independent from angular velocity. Among the other factors that influence the distribution of stresses in rotating disks are the presence of a thermal field and the variation

in geometry (sharp variation and holes imply the presence of notch effects and higher stresses).

This research is focusing, as said in the introduction, on turbine disks, which are much different from the compressor ones, especially because the working condition turbines experience are much more stressful in terms of temperature gradients and transmitted power.

The Engine



TYPE TF39-GE-1C

- | | | |
|-------------------------------|--|---|
| 1. FIRST STAGE FAN (N_1) | 9. HIGH PRESSURE COMPRESSOR INLET GUIDE VANE | 15. LOW PRESSURE TURBINE |
| 2. FAN INLET GUIDE VANE | 10. ENGINE OIL TANK | 16. EXHAUST CONE |
| 3. SECOND STAGE FAN (N_1) | 11. HIGH PRESSURE COMPRESSOR (N_2) | 17. 13th STAGE BLEED AIR MANFOLD |
| 4. TRANSLATING COWL ACTUATOR | 12. FUEL NOZZLE | 18. FUEL CONTROL |
| 5. FAN AIR EXIT VANE | 13. COMBUSTION CHAMBER | 19. FUEL PUMP |
| 6. TRANSLATING COWL | 14. HIGH PRESSURE TURBINE | 20. LUBE SCAVENGE PUMP AND N_2 TACHOMETER |
| 7. BLOCKER FLAP | | 21. ACCESSORY DRIVE GEARBOX |
| 8. BLOCKER LINK | | 22. TRANSFER GEARBOX |

CSFM-1-2-006

Figure 4: Cross-section view of a turbofan engine

Once that loading conditions are described, it is possible to define the exact geometry of the disk and proceed with the design optimization. This optimization is made considering in first analysis the burst speed of the disk and the fatigue life, but also caring about lightness and other dimensional constraints that have to be taken into account in case of aeronautic turbines.

For what concerns the safety factor of turbine rotating disks against burst, the study is performed taking into account three main kind of load: thermal field, blades load and centrifugal load.^[3]

1. **Thermal loads:** produced by the non uniform distribution of temperature in the disk when it is working. The external region of the rotor that is closer to the hot gasses, in fact, is hotter than the internal area. This non uniform temperature gradient causes a deformation of the material, related to the coefficient of thermal expansion.
2. **Influence of the blades and slots:** that are on the external rim of the disk. The presence of those bodies on the external ring causes an additional traction load in the radial direction, since blades and slots behave like concentrated masses under the effect of the centrifugal field.
3. **Centrifugal forces:** originated in the rotor, as an inertial body with not negligible mass. So whenever it rotates, a centrifugal load associated with the angular velocity is originated.

Once the loading conditions are known, the optimization of the disk geometry is carried out taking into account mainly two factors: costs and weight. The idea is to reduce the material

used, in order to obtain a sufficient light rotor with the highest strength (according to the standards), but it is important also to consider the production costs and the fact that usually those turbine disks are made of very expensive materials, so every machining process has to be made taking care about containing the total cost of the device.

2.2 Materials

Another very important thing to consider in order to improve the design of a turbomachinery disk is the choice of the material and the manufacturing techniques. As said before, the values of temperature and pressure in the different parts of the engine are varying a lot as is possible to see in the Figure 5.

Both pressure and temperature reach their maximum right into the combustor, due to the high temperature of the combustion process. The pressure tendency is roughly symmetric: air is compressed while it passes through the compressor stages, while combusted gasses are expanded into the turbines. On the other hand, the temperatures occurring in the compressor are much lower than the turbine (turbines work at temperature around 1000°C).

The presence of higher temperature and, more in general, of a more stressful environment (corrosive gasses, higher rotational speeds, etc.) justify the use of different material for compressors and turbines.

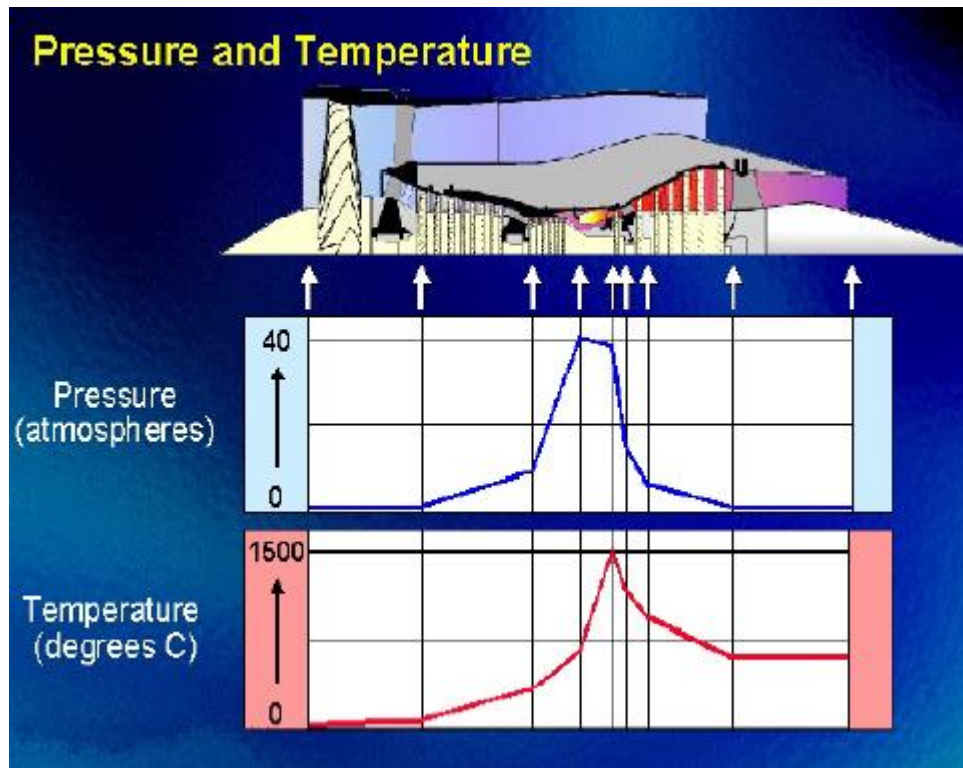


Figure 5: Temperature and pressure profiles inside a turbo engine

In Figure 6 it is possible to look at the different kind of materials used for the principal components of a turbofan engine. At a first glance it is clear that the use of nickel alloys for both combustors and turbine is due to the higher temperatures occurring in those parts.

Turbine disks and their blades are usually made of nickel super-alloys, while compressor ones are made of titanium alloys. The term super-alloy (made by nickel, cobalt or nickel+steel) is used to refer to those metal alloys that keep their mechanical properties constant at very high temperature and are more resistant to corrosion due to corrosive environment (look at Figure

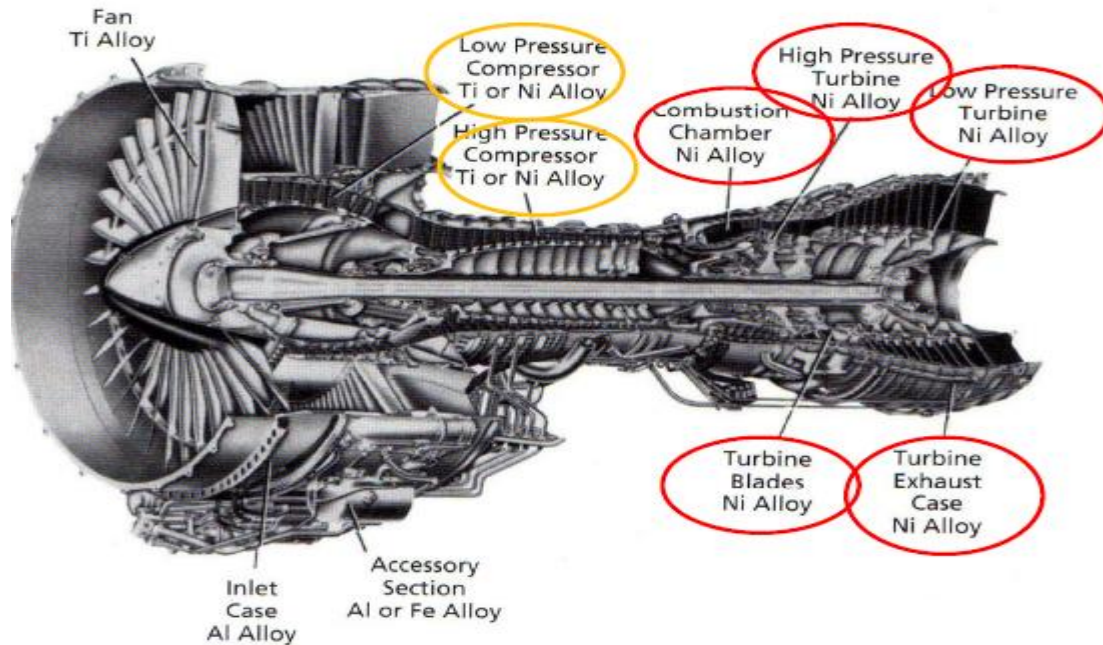


Figure 6: Principal kind of materials used in a turbo engine

7). The capacity of preserving a very high strength at temperature that are close to the 80% of the melting point temperature explain why nickel super alloys are used to build turbine components, in which very hot and chemically harsh gasses are expanded. A very common nickel super-alloy used for turbine disks is, for instance, the “INCONEL[®] 718”, which is the commercial name, property of *Special Metals Corporation*, of a very complex alloy characterized by the presence of a elevate number of metals (principally Nickel, Chromium, Iron, Titanium, Cobalt and Aluminum). The elevate number of elements in the alloy is the characteristic that guarantees the high strength of this material, because of the precipitation at grain boundary.

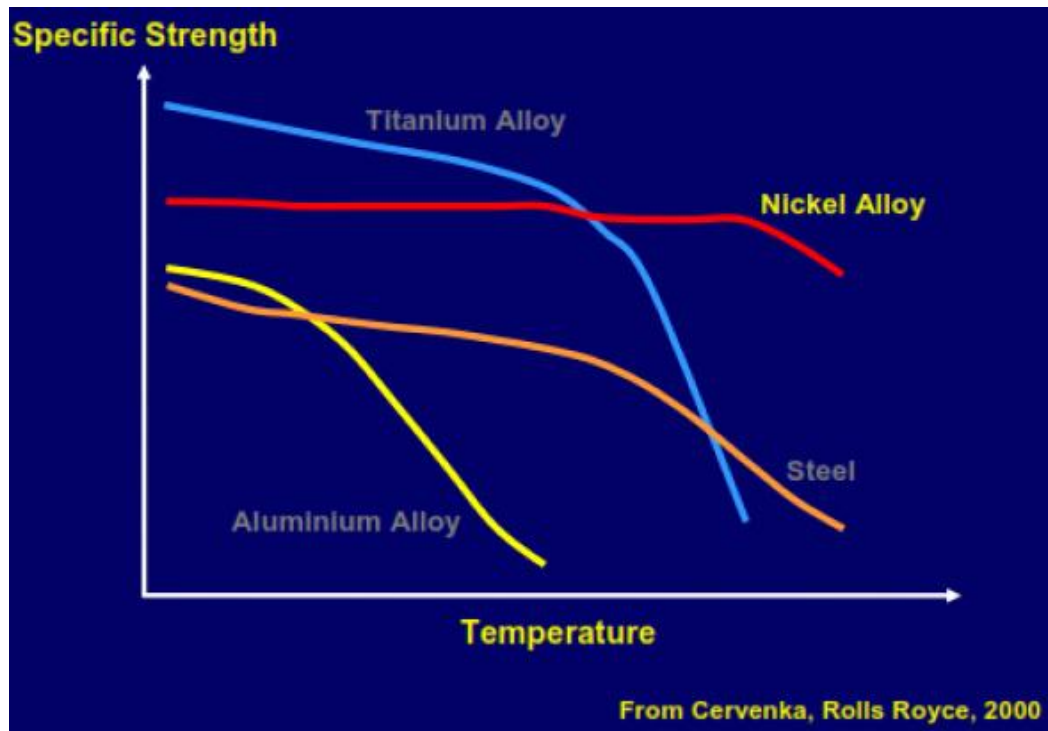


Figure 7: Variation of the specific strength of metal alloys as temperature changes

This precipitate prevents slip and thereby increases the resistance of the material.

Regarding production techniques, it is interesting to notice the different methods used for disks and blades: disks are manufactured by forging, in order to obtain a poly-crystalline with smaller grains; blades, instead, are produced by casting controlling the cooling in order to obtain a mono-crystalline structure. Finally, slots on the external rim of the disk are realized by broaching, thus by removing material until the desired shape is realized.



Figure 8: Example of a turbine disk

2.3 Types of failure

As said before, the burst of a rotor disk is a very dangerous phenomenon and, for this reason, has been strictly regulated by international agencies (EASA and FAA. Producers have to satisfy strict safety requirements in order to obtain the certification to flight. Many experimental tests were conducted with the purpose of understanding what causes failure in a rotating disk and the fracture modes.

If we consider the studies concerning response of disks to centrifugal loads two main phenomena can be identified as the ones that cause burst^[4,5].

- Elastoplastic instability;
- Propagation of a fatigue crack that leads to an unexpected burst.

The first case is verified whenever the stresses induced by an high rotational speed (higher than the working speed) are so elevated that they exceed the yield point. This leads to high radial deformation into the disk, which causes an increase of the centrifugal load and, finally, the structure reaches a critical condition. In the FE method used in this thesis a static analysis is conducted for increasing rotational speeds, investigating the case of elastic instability when the analysis stops because of a not converging solution and the burst speed is taken equal to the one used for the last step.

In case of fatigue failure, instead, burst is caused by the propagation of a fatigue crack (due to cyclic loading) at normal operating speed. Several examples^[6] available in literature deal with the propagation of fatigue cracks and they all verified that generally fatigue develop in the most stressed areas: fir-tree rim region, the hub region, and the assembly holes.

Another very important issue to be concerned about is to determine how the disks behave in the post critical condition, or in other words, how they break and evaluate the number of fragments generated by the burst. The studies conducted by Dhondt (1993), Bert and Paul (1995), Dhondt and Kohl (1999) focus on this theme. They demonstrated that the larger the fragments are, the more translation energy is possessed by them.^[7] For this reason the research has also to predict the number of fragments and their kinetic energy (dependent on the angular velocity) and study various techniques to improve the disk safety, such as the autofrettage,

which induces a compressive layer in the internal region of the rotor.

Fracture can occur in two different ways as shown in Figure 9:

- *rim peel burst*;
- *hoop mode burst*.

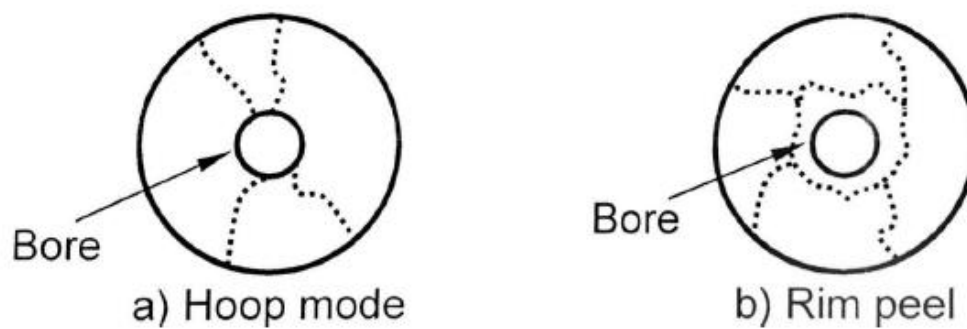


Figure 9: Fracture modes

The first fracture mode, the *rim peel burst*, usually appears in presence of high radial stresses in the web area (especially when holes are present): a circumferential crack causes the detachment of the external part of the disk from the internal one; the internal part usually does not fragment itself into pieces, while the remaining part disintegrates in many parts.

On the other side, the elevated centrifugal load proportional to the square angular velocity causes the *hoop mode burst*: a fracture in which the detachment surfaces develops radially from the bore to the external rim.

Other experimental works (Shikida and Kanayama, 1980) study the critical condition at burst in case of notched disks, in order to understand, looking at the propagation of the Lüders' bands, the plasticization areas of the material for both notched and unnotched disks and, eventually, the fragment generated when the disk fails.

In case of unnotched disks, the Lüders' lines “originate at the bore and spread rapidly toward the outside”^[8], therefore the disk plastic deformation has a quasi-circular shape.

In the notched disks, plastic deformation appears in the region of the notch root and spreads from the notch tips to the outside of the disk, so three distinct plastic areas can be identified studying the Lüders bands (Figure 10). It was also demonstrated that notched disks broke in two distinct parts along the diameter contained in the notch roots (Figure11(b)).^[8]

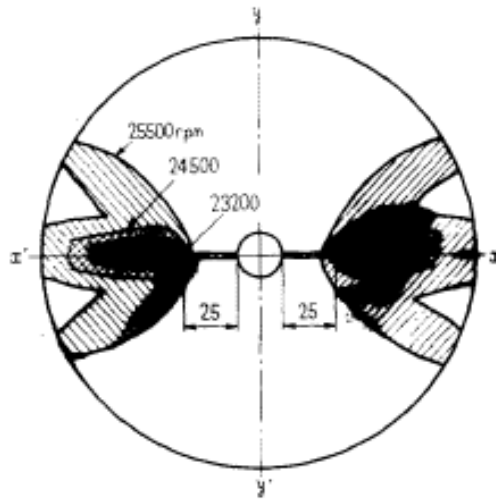
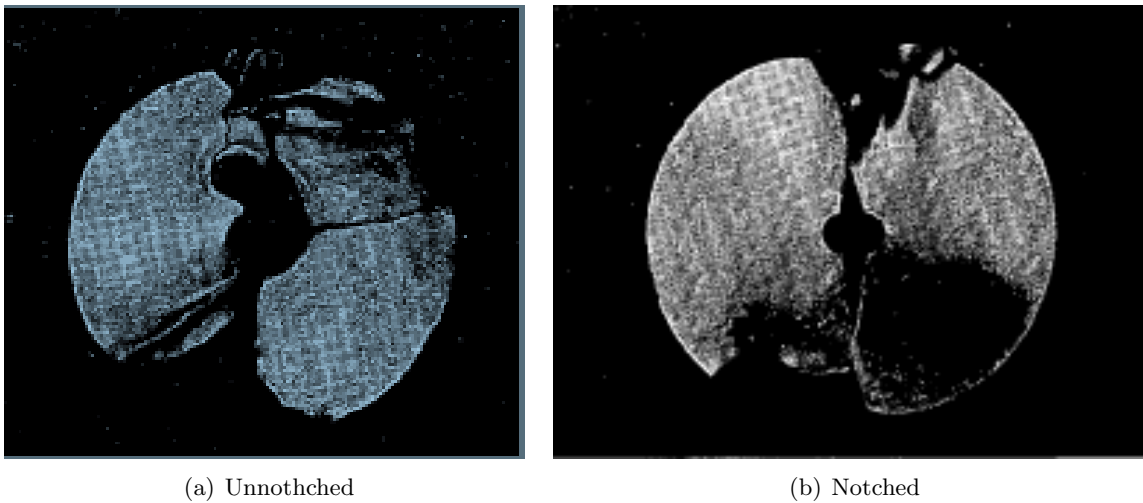


Figure 10: Propagation of Lüders' bands into a notched disk



(a) Unnotched

(b) Notched

Figure 11: Comparison of burst between notched and unnotched disk

2.4 International standards for rotor integrity

The two main international authorities that regulates the safety of air transportation, the *European Aviation Safety Agency* in Europe and the *Federal Aviation Administration* in the USA, had set the requirements that turbine disks have to satisfy in order to be used for civil air transportation. Military regulation, instead, can vary from a country to another, since they depend only on internal regulations, but generally this internal regulations are very similar to the two international ones cited above.

The condition that the turbine disks have to satisfy are listed in the two certification reported in the Table I for the “*CS-E 840 - Rotor Integrity*”^[9] and the “*FAR 33.27 - Turbine, compressor, fan, and turbosupercharger rotor overspeed*”^[10].

They both aim to guarantee the integrity of the turbine in case they have to operate in overspeed conditions.

All the turbines used in civil airplanes have to satisfy all the conditions listed in the table in order to obtain the certification to flight, and after the test disks have to remain intact, with no residual plastic deformations.

The first line of Table I refers to the highest velocity at which the rotor can rotate in a normal mission (e.g. takeoff rotational speed of the rotor), defined during the thermodynamic design. The second entries are intended to consider the maximum velocity that cause failure of some component into the motor, bringing the rotor to over-speed. The last line of the table, finally, consider as maximum velocity the one that arises when a critical component breaks and, meanwhile, another failure is verified.

TABLE I: ROTOR INTEGRITY CONDITIONS

EASA CS-E 840	FAR 33.27
120% of the maximum permissible rotor speeds associated with any of the ratings except OEI ratings of less than 2 1/2-minutes.	120 percent of its maximum permissible r.p.m. if tested on a rig and equipped with blades or blade weights.
115% of the maximum permissible rotor speeds associated with any OEI ratings of less than 2 1/2-minutes.	115 percent of its maximum permissible r.p.m. if tested on an engine.
105% of the highest rotor speed that would result from the failure of the component or system which is the most critical with respect to over-speeding	105 percent of the highest speed that would result from failure of the most critical component or system in a representative installation of the engine.
100% of the highest rotor speed that would result from the failure of the component or system which, in a representative installation of the engine, is the most critical with respect to over-speeding when operating at any OEI ratings of less than 2 1/2-minutes.	The highest speed that would result from the failure of any component or system in a representative installation of the engine, in combination with any failure of a component or system that would not normally be detected during a routine preflight check or during normal flight operation.

The conditions listed in the table have to be verified through experimental tests in which the engine is run for at least 5 minutes, measuring the deformation of the rotor disk and verifying that tolerances and material properties are still acceptable in any of those conditions. The time constraint is very important for the testing purpose, even if the burst phenomenon is not supposed to be time dependent. Safety normatives have to ensure that engines are not stopping their run in any of those conditions, besides, all the mechanical components (e.g. bolts, flanges, etc.) at their first run have time to adapt and this makes possible to measure the variation

from working conditions.

Eventually, it is important to point out that the certification of a disk against burst requires to run it for 5 minutes at the estimated value of burst speed (calculated analytically or by numerical models like in this thesis), but in order to be sure that the set value is not oscillating under the desired one, tests are usually run at higher speed than the estimated one, so that it is possible to ensure the safety conditions also in presence of some little imperfections.

2.5 Finite Element Method

The FEM (Finite Element Method) Analysis is nowadays one of the most used method to study complex systems both in academical and industrial field. This kind of analysis can be used for structural analysis (both static and dynamic) as well as for fluids or electrical field.

The goal of this method is to use the high calculation capacity of modern computers in order to solve problems that usually require the solution of partial differential equations are and are too complex to be solved analytically.

The mathematical procedure behind that is based on the division of the domain into a large number of very small elements that are easier to solve: the solution is obtained by defining a local stiffness matrix (on each element), then, assembling all the elemental matrices into a global stiffness matrix that is representing the equilibrium problem and, finally, expand, through continuity, the solution to the whole system.

The great advantage of using this kind of calculation is to provide solution for every kind of system, no matter how complex it might be. However, it is important to point out that in

order to correctly study a problem using this method the users have to precisely understand how the code operates and interpret the result considering the physical meaning of it.

Therefore, the main advantage of the FEM (the discretization over a large number of small elements), turns it self into the main drawback. In fact, the solution of the problem is approximated because the real problem has been reduced to an algebraic system and the solution is simulating, using appropriate shape functions, the displacement of the nodes of each element. The numerical solution of this matricial problem is correct (unless mathematical approximations) only on the nodes of the elements, while for the rest of the element the mean is calculated. Hence, great importance is given to the preliminary analysis of the problem, since the mesh has to be correctly dimensioned in order to be small enough to fit the smaller geometry perturbations and to produce the most accurate solution, but, on the other side, the increase of the number of elements requires longer calculation time and more powerful computers.

For this thesis, the commercial code Ansys has been used in order to build a finite element model of a disk that follows in the most accurate way the behavior of a real turbine disk.

Ansys is one of the most famous commercial FEM code and it offers a large variety of elements and different solution options that were used to study the part in different ways, as it will be described later in this thesis.

Researches carried out previously^[2] on this topic were focused on validating the use of such a method and the comparison of it with some analytic analysis present in literature. Some easy model were studied and the results confirmed the robustness of the hypothesis used to model

this kind of problem.

On the other side, a comparison can be made also between the values given by the practice used by Avio group and the results obtained from the FEM, looking at the different approaches that justify the failure in the over-speed conditions.

Starting from those key-points the present study aims to develop a three dimensional FE model of a real disk using both *Small Displacement* and *Large Displacement* calculations in order to find the burst limit when the plasticity of the material is taken into account.

Again, a discussion on the safety design of rotating disk will originate from the comparison of the results in terms of burst speed of the disk obtained using the numerical method and the same values obtained with the analytic approaches present in literature.

CHAPTER 3

CONSTITUTIVE EQUATIONS OF ROTATING DISKS

Most of the structural problems are tridimensional problems, usually complex to solve analytically and, for this reason, treated in easier ways from the designers. Therefore, some simplifications can be made in order to reduce the set of equations needed to only one equation to use for solving the problem of rotating disks using an analytic approach: for example it is possible to reduce the 3D problem to a bi-dimensional one and apply the equilibrium and the stress-strain relations.

Not all the disks geometries allow this kind of simplification and for this reason numerical models, like the one developed for this thesis, are sometimes needed in order to carry out the complete calculation. It is, however, interesting to show in this chapter the stresses induced by rotation in an axisymmetric disk and discuss the failure theories on which the practice currently used by Avio S.p.A. to design turbine rotors is based.

The hypothesis that allow to develop a simplified equation in two-dimensions is based on two conditions: the *axisymmetry*, and *plane stress*.

The conditions necessary in order to satisfy the hypothesis of *axisymmetry* are:

- Isotropic material, or axisymmetric orthotropic material;
- Axisymmetric geometry of the body;

- Axisymmetric applied load.

The second simplification used to study the rotating disks is to consider the problem as a *plane stress* one, even if this assumption should be used only for thin disks (constant thickness much lower than the radius), while for thick disks the *plane strain* case is more adequate.^[3]

Such a problem can be classified as a *plane stress* one if the following conditions are verified:

- Homogeneous and isotropic material;
- No body forces on the axial direction;
- Plane body forces can vary only in the plane and not in the axial direction;
- Boundary conditions are not varying along the axial direction.

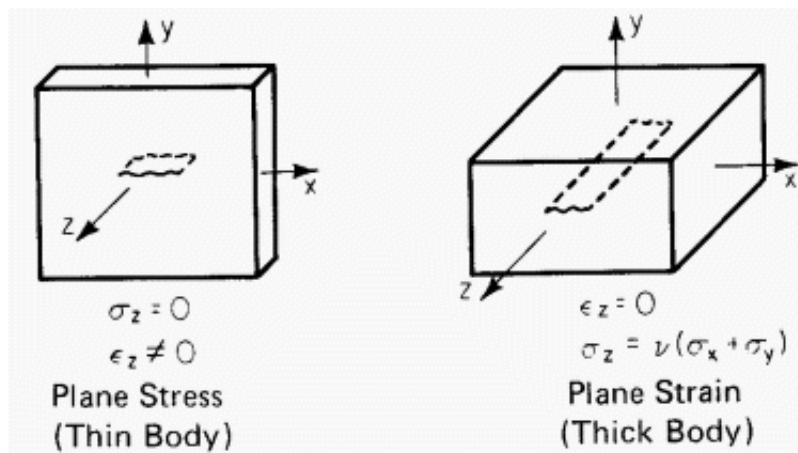


Figure 12: Plane stress vs plane strain

It is, however, possible to show that in case of zero body forces the plane stress and the plane strain theories bring to the same expression of stresses in the plane.

Thanks to the two simplification explained above it is possible to find an analytical solution to the simplified problem, where all the quantities vary only as a function of the radial coordinate, r , and do not depend on both θ (axisymmetry) or z (plane stress). Hence $\tau_{rc} = \gamma_{rc} = 0$, meaning that σ_r and σ_c are principal stresses, while σ_a is zero in case of plane stress and not zero in case of plane strain.

This chapter presents a very common analytical dissertation on rotating disk, showing that the assumptions made above lead to only one non trivial equation of equilibrium. It is also shown how to derive the equation for radial and circumferential stress in case of elastic materials and plastic materials. This theoretical basis was fundamental to start the development of an advanced FEM calculation on parts that are impossible to solve analytically. In particular, the comparison between the numerical and the analytic solutions was object of previous studies on the FE model and proved the accuracy of the model and validated the numerical approach with Ansys.^[11]

3.1 Equation of equilibrium

Considering to the two hypotheses listed before, the problem we are dealing with is the study of a bi-dimensional problem in a cylindrical coordinate system, where both the geometry

and the load are axisymmetric (look for example the disk in Figure 13).

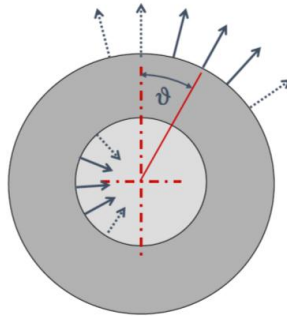


Figure 13: Axisymmetric disk under axisymmetric load

If we consider an infinitesimal element obtained cutting the disk with two radii that form an infinitesimal angle $d\theta$ and included in two circumferences distant dr like done in Figure 14, it is possible to write the equations of equilibrium, and, consequently, find the stresses in the rotating disk.

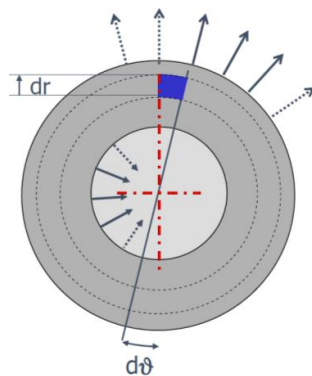


Figure 14: Infinitesimal element on a disk

Once that the appropriate reference system is defined, a set of three local cartesian axes can be identified for the infinitesimal element (Figure 15):

- An axis a parallel to the revolution axis of the disk;
- An axis r in the radial direction;
- A circumferential axis c , tangent to the circle that passes through the center of mass of the infinitesimal element.

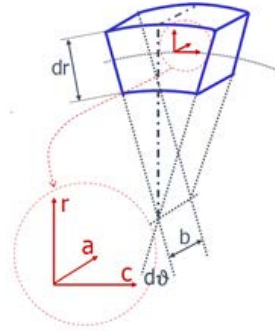


Figure 15: Local cartesian axes

In this reference system the stresses along the Cartesian axes: σ_a , σ_r and σ_c (Figure 16) are principal and it is possible to write the six equations of equilibrium.

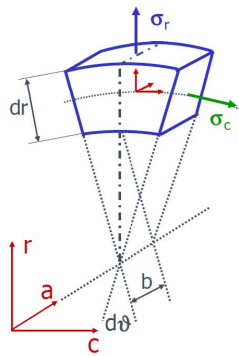


Figure 16: Stresses on the infinitesimal element

Five out of six equations of equilibrium are satisfied by the hypotheses made before. In particular the equilibrium of forces along the axis a and moments about the axes r and c are satisfied thanks to the plane stress assumption, while the equilibrium of the moment about the a axis and the forces along the c axis are satisfied because all the forces in the plane are axisymmetric.

Thus the only remaining equation is the equilibrium of forces along the radial direction r . In Figure 17 it is possible to look at the equilibrium of forces on the infinitesimal element, where b is the thickness of the element, σ_r is the radial stress, σ_c is the circumferential (or hoop) stress and Φ_V is the body force per unit volume (centrifugal force in case of rotating disks).

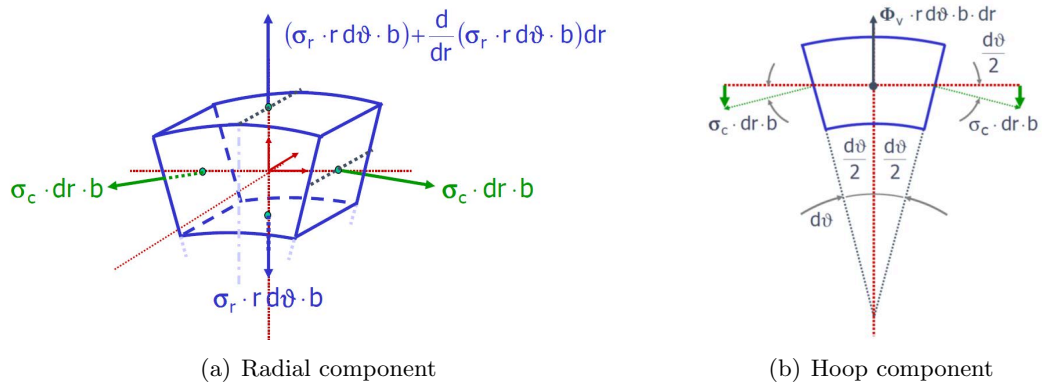


Figure 17: Equilibrium

Three components have to be considered when considering the radial equilibrium:

1. A radial component due to σ_r (Figure 17(a)):

$$\frac{d}{dr}(\sigma_r r d\theta b) dr \quad (3.1)$$

2. The radial component of the hoop stress σ_c :

$$2 \sigma_c dr b \sin\left(\frac{d\theta}{2}\right) \cong 2 \sigma_c dr b \frac{d\theta}{2} = \sigma_c dr b d\theta \quad (3.2)$$

3. A radial body force (Figure 17(b)):

$$\Phi_V r d\theta b dr \quad (3.3)$$

Grouping all the terms together, the equation of equilibrium along the radial direction r is:

$$\frac{d}{dr}(\sigma_r r d\theta b) dr - \sigma_c b d\theta dr + \Phi_V r b d\theta dr = 0 \quad (3.4)$$

3.2 Strain-Displacement relations

Consider now the deformation of the infinitesimal element, denoting the r displacement by u . The general deformation experienced by the element in the radial direction is shown in Figure 18.

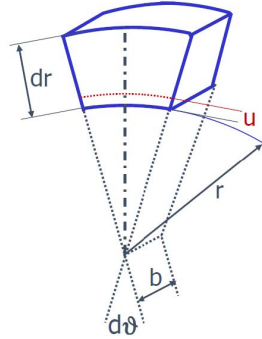


Figure 18: Radial displacement

The radial strain ε_r is associated with the u displacement, and the relationship between them is the following:

$$\varepsilon_r = \frac{du}{dr} \quad (3.5)$$

The tangential strain owing to u (deformation per unit length) is:

$$\varepsilon_c = \frac{(r + u) d\theta - r d\theta}{r d\theta} = \frac{u}{r} \quad (3.6)$$

Combining the two equations (Equation 3.5 and Equation 3.6) it is possible to rewrite ε_r as:

$$\varepsilon_r = \frac{d(\varepsilon_c r)}{dr} \quad (3.7)$$

Two equivalent formulation of the compatibility equation are, therefore, derived:

$$\frac{d}{dr} (\varepsilon_c r) - \varepsilon_r = 0 \quad (3.8a)$$

$$\frac{d\varepsilon_c}{dr} r - (\varepsilon_r - \varepsilon_c) = 0 \quad (3.8b)$$

3.3 Elastic field: Hooke's law

In case the study is conducted only on the elastic part of the stress-strain curve, neglecting the plasticization of the structure, the *Hooke's law* is used to express the relation between stresses and strains. In particular, for elastic materials under the yield point, this relation is linear and the constant of proportionality is the *Young's modulus*. Hence $\sigma = E \varepsilon$.

To write Hooke's law in polar coordinates in the case of plane stress, it is necessary to consider $\sigma_a = 0$. So the direct (Equation 3.9) and inverse (Equation 3.10) stress-strain relationships are expressed as follows:

$$\text{Direct relationship} \quad \begin{cases} \varepsilon_r = \frac{1}{E} (\sigma_r - \nu \sigma_c - \nu \sigma_a) = \frac{1}{E} (\sigma_r - \nu \sigma_c) \\ \varepsilon_c = \frac{1}{E} (\sigma_c - \nu \sigma_r - \nu \sigma_a) = \frac{1}{E} (\sigma_c - \nu \sigma_r) \end{cases} \quad (3.9)$$

$$\text{Inverse relationship} \quad \begin{cases} \sigma_r = \frac{E}{1 - \nu^2} (\varepsilon_r + \nu \varepsilon_c) \\ \sigma_c = \frac{E}{1 - \nu^2} (\varepsilon_c + \nu \varepsilon_r) \end{cases} \quad (3.10)$$

The third constitutive equation of the material represents the strain in the axial direction due to the planar stress:

$$\varepsilon_a = \frac{1}{E} (\sigma_a - \nu \sigma_r - \nu \sigma_c) = \frac{-\nu}{E} (\sigma_r + \sigma_c) \quad (3.11)$$

3.4 Thermal expansion term

Considering an unconstrained elastic body, the effects of the increase or decrease of the temperature result in an expansion or contraction of the solid. Two cases have to be separately considered.

In case the body is heated in such a way to produce a non uniform temperature field and the material exhibits an anisotropic behavior, or the boundary conditions are preventing the free expansion in some direction, then the thermal effects are translated into additional stresses.

On the other side, if the material is isotropic and free to expand, there is an additional strain component ε_t to be taken into account and it is equal in all the directions:

$$\varepsilon_t = \alpha \Delta T \quad (3.12)$$

where α is the coefficient of linear thermal expansion, and ΔT is the change in temperature.

Regarding the case of the rotating disks discussed here, where a plane stress problem and isotropic material is considered, the thermal strain ε_t can be added to the strains defined in the Equation 3.9 that is updated as follows:

$$\begin{cases} \varepsilon_r = \frac{1}{E} (\sigma_r - \nu \sigma_c) + \alpha \Delta T \\ \varepsilon_c = \frac{1}{E} (\sigma_c - \nu \sigma_r) + \alpha \Delta T \end{cases} \quad (3.13)$$

3.5 Equations for disks in the elastic field

Considering the elastic behavior of the material, thus relying on the Hooke's law, the equations of equilibrium can be used to solve simple problems like the two easy cases reported below.

3.5.1 Rotating disks of constant thickness

The equation of equilibrium, Equation 3.4, can be used to treat the case of rotating disks of constant thickness. In this particular case, the thickness b is constant and can be carried out from the derivative and simplified, while the body force has to be taken into account and it is equal to the centrifugal force. The body force per unit volume is $\Phi_V = \rho \omega^2 r$, where ρ is the mass density and ω is the angular velocity.

By carrying out b , substituting the definition of Φ_V and simplifying the terms dr and $d\theta$, the equilibrium can be rewritten as:

$$\frac{d\sigma_r}{dr} + \frac{\sigma_r - \sigma_c}{r} + \rho \omega^2 r = 0 \quad (3.14)$$

Considering the stress-strain relationship (Inverse Hooke's Law, Equation 3.10) and substituting into it the strain-displacement relations (Equation 3.5 and Equation 3.6) we get:

$$\begin{cases} \sigma_r = \frac{E}{1-\nu^2} \left(\frac{du}{dr} + \nu \frac{u}{r} \right) \\ \sigma_c = \frac{E}{1-\nu^2} \left(\frac{u}{r} + \nu \frac{du}{dr} \right) \end{cases} \quad (3.15)$$

So, the Equation 3.14 becomes:

$$\frac{E}{1-\nu^2} \left[\frac{d^2u}{dr^2} + \frac{\nu}{r} \frac{du}{dr} - \frac{\nu u}{r^2} + \frac{1}{r} \left(\frac{du}{dr} + \nu \frac{u}{r} - \frac{u}{r} - \nu \frac{du}{dr} \right) \right] = -\rho \omega^2 r$$

$$\Downarrow$$

$$\frac{d^2u}{dr^2} + \frac{1}{r} \frac{du}{dr} - \frac{u}{r^2} = -\frac{(1-\nu^2)}{E} \rho \omega^2 r \quad (3.16)$$

It can be easily proven that the complete solution of this differential equation is:

$$u = -\frac{\rho \omega^2 r^3 (1-\nu^2)}{8E} + c_1 r + \frac{c_2}{r} \quad (3.17)$$

where c_1 and c_2 are the integration constants and depend on boundary conditions. The complete solution (Equation 3.17), upon substitution into the definition of stresses in Equation 3.15 provides the following expressions for radial and tangential stresses:

$$\begin{cases} \sigma_r = \frac{E}{1-\nu^2} \left[\frac{-(3+\nu)(1-\nu^2)\rho\omega^2 r^2}{8E} + (1+\nu)c_1 - (1-\nu)\frac{c_2}{r^2} \right] \\ \sigma_c = \frac{E}{1-\nu^2} \left[\frac{-(1+3\nu)(1-\nu^2)\rho\omega^2 r^2}{8E} + (1+\nu)c_1 - (1-\nu)\frac{c_2}{r^2} \right] \end{cases} \quad (3.18)$$

Annular disks

In case of an annular rotating disk with zero pressure on both the inner and outer boundaries
(19) the distribution of stresses is due only to the rotational effects.

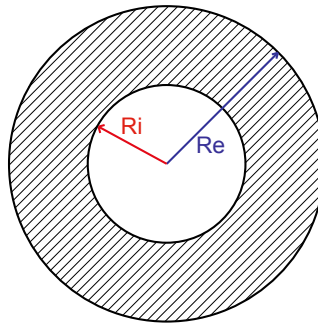


Figure 19: Annular disk

The boundary conditions for this particular case are:

$$(\sigma_r)_{r=R_i} = 0 \quad ; \quad (\sigma_r)_{r=R_e} = 0 \quad (3.19)$$

Combining the boundary conditions with Equation 3.18 it is possible to find the two constants c_1 and c_2 :

$$c_1 = \rho \omega^2 \frac{(R_i^2 + R_e^2)}{E} \frac{(1 - \nu)(3 + \nu)}{8} \quad (3.20)$$

$$c_2 = \rho \omega^2 \left(\frac{R_i^2 R_e^2}{E} \right) \frac{(1 + \nu)(3 + \nu)}{8} \quad (3.21)$$

Isolating, then, the reference circumferential stress $\sigma_0 = \rho \omega^2 R_e^2$ calculated on a very thin disk with zero radial extension, the final expression for the stresses into an annular disk is derived:

$$\begin{cases} \sigma_r = \sigma_0 \frac{3 + \nu}{8} \left[1 + \frac{D_i^2}{D_e^2} - \frac{D_i^2}{D^2} - \frac{D^2}{D_e^2} \right] \\ \sigma_c = \sigma_0 \frac{3 + \nu}{8} \left[1 + \frac{D_i^2}{D_e^2} + \frac{D_i^2}{D^2} - \frac{1 + 3\nu}{3 + \nu} \frac{D^2}{D_e^2} \right] \end{cases} \quad (3.22)$$

Finally, knowing that $u = r\varepsilon_c$ it is possible to write the expression of the radial displacement in an annular rotating disk:

$$u = \frac{D}{2E} (\sigma_c - \nu \sigma_r) = \sigma_0 D \frac{3 + \nu}{16E} \left[(1 - \nu) \left(1 + \frac{D_i^2}{D_e^2} \right) + (1 + \nu) \frac{D_i^2}{D^2} - \frac{1 - \nu^2}{3 + \nu} \frac{D^2}{D_e^2} \right] \quad (3.23)$$

3.5.2 Rotating disks of variable thickness

Turbomachinery disks seldom have constant thickness: they usually are thicker near the center and much thinner as the radius increases. This is made in order to reduce stress concentrations on the inner radius preserving the disk lightness.

For a variable thickness disk, the thickness term b in the equilibrium equation cannot be neglected because it varies with the radius ($b = b(r)$), hence the Equation 3.4 becomes:

$$\frac{d}{dr} (\sigma_r r d\theta b) - \sigma_c b = -\rho\omega^2 r^2 b \quad (3.24)$$

Note that also in this case the shear stresses are zero because of the symmetry of the problem.

Considering, now, the constitutive equations of the material expressed in Equation 3.13 the following compatibility equation can be obtained:

$$\frac{d}{dr} \left(\frac{\sigma_c}{E} \right) - \frac{d}{dr} \left(\frac{\nu \sigma_r}{E} \right) + \frac{d}{dr} (\alpha \Delta T) - \frac{(1 + \nu) (\sigma_r - \sigma_c)}{E r} = 0 \quad (3.25)$$

The solution for the stress distribution (σ_r and σ_c) in a variable thickness disk comes from the combination of the Equation 3.24 and the Equation 3.25 and can be computed manually using the well known step-wise profile approximation proposed by Grammel (Grammel's method, 1923)^[12] or a finite difference method, such as the Manson's method (1947)^[13].

3.6 Plastic field models

In the elastic field, or rather for low stresses, a metallic specimen follows the Hooke's law, so as the load increases the deformation also increases proportionally to the Young's Modulus E ($\sigma = E\varepsilon$). In this elastic condition, when the load is removed, the specimen returns to the original configuration, following the same path on the stress-strain diagram.

Metallic materials behave in a totally different way when the applied stress exceeds the yielding value. After this stress value (defined as *conventional limit of elasticity*¹), the material is permanently deformed and after removing the external load it does not return into the original configuration, but preserves some deformation. Yielding is, then, the transition phase that stands between the elastic and the plastic behaviour of the materials and is typically followed by an hardening phase.

Plasticity can be explained as the macro-scale result of the molecular modifications that occur in a material under certain loading conditions. In particular yielding and hardening are both due to irreversible modifications caused by the dislocation motion.^[14]

In Figure 20, three typical material behaviors are compared showing the stress-strain curves. Brittle materials present a restricted hardening phase: after the elastic area they reach the fracture very rapidly with low deformation. Hardening materials are characterized by a large increase of deformation in the plastic area and a corresponding increase of stress before reaching the fracture point, while the yielding zone is absent. Ductile materials (like the “INCONEL[®] 718”) exhibit a very wide yielding phase, in which deformation increases without a substantial increase of stress.

¹**Conventional limit of elasticity:** is the unit stress corresponding to an elongation which is not proportional to the stress on the test piece so that the excess of elongation beyond proportionality is equal to a fixed percentage of the initial gauge length (generally 0.2%)

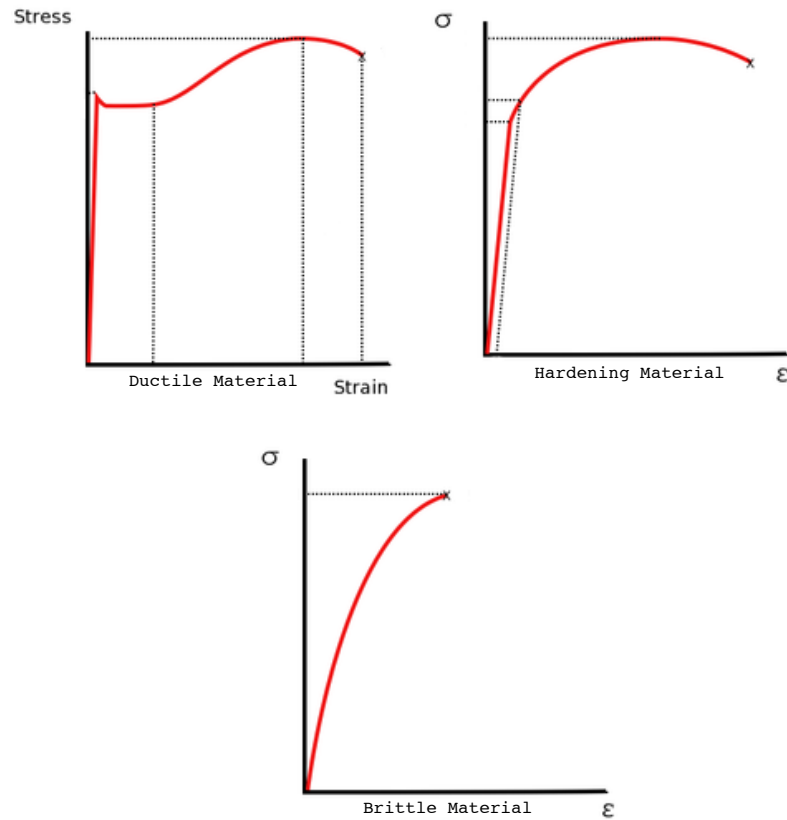


Figure 20: Typical material behaviours

Plasticity gains a relevant role in ductile materials, since they can experience very large deformation before the fracture. It is also influenced by the environmental conditions, and in particular by temperature. The presence of high temperatures, in fact, fosters the plasticity behaviour of materials, while low temperatures reduce it.

The equations derived in the previous sections are not verified if plasticity has to be taken into account, because the Hooke's law is not valid anymore after the yielding point.

The correct mathematical theory to use in case of plasticity, the *flow plasticity theory*, or *incremental theory of plasticity* (that will be further discussed later on in this thesis), was developed in 1960s and uses a set of non-linear, non-integrable equations to describe the correlation between stress and strains.^[15] This theory is based on an incremental approach, studying the relationship between the infinitesimal load increments \dot{P} , and the corresponding increments in term of stresses, strains and displacements ($\dot{\sigma}$, $\dot{\epsilon}$ and \dot{u}).

The flow theory is based on three main axioms:

1. Materials are characterized by a threshold resistance. This means that the possible stresses are a limited.
2. Deformations are irreversible, the material does not recover its original configuration after a loading cycle.
3. For low stresses, the behavior of the material can be considered as elastic.

Two material models are commonly used to describe the plasticity of a material: the *Elastic Perfectly Plastic* model, and the *Ramberg-Osgood* model.

3.6.1 Elastic perfectly plastic model

A very common model is the one of an *Elastic Perfectly Plastic* (EPP) material, in which a very extended yielding is considered with a flatten top stress-strain curve, that has large plastic

deformation at a constant stress level.

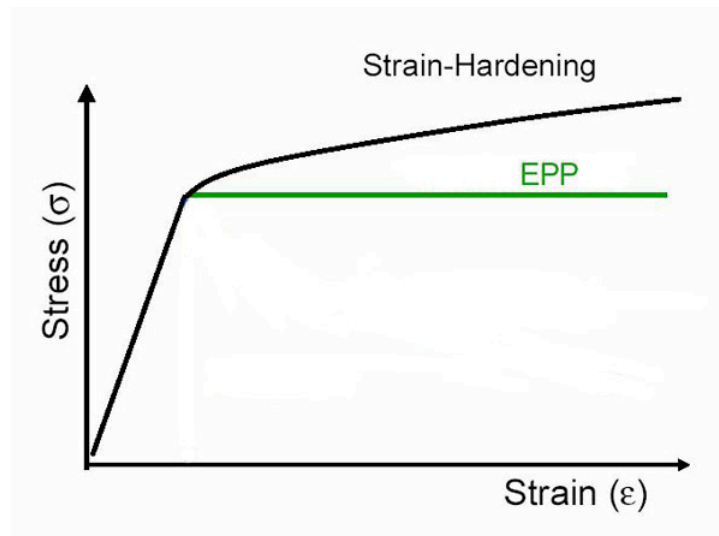


Figure 21: EPP material compared to hardening material

In this model all the admissible stresses are below the yielding point and the ultimate tensile strength is equal to the yielding:

$$\sigma \leq \sigma_{yield} \equiv \sigma_{UTS}$$

Plasticity occurs whenever the stress reaches the yielding, so the yielding function $f(\sigma) = 0$ is defined as:

$$\text{Yielding function : } f(\sigma) = \sigma - \sigma_y$$

In conclusion, this model describes the material as analogous to an ideally elastic one if the stress state is not exceeding the yield point. On the contrary, plasticization occurs and the material cannot suffer the increase of strain, so it brings to failure.

3.6.2 Ramberg-Osgood model

A second model of plasticity, developed by Ramberg and Osgood^[16] is used in order to consider the non linear relationship between stress and strain near the yield point in the case of an hardening material.

In its original form, the Ramberg-Osgood equation for strain is:

$$\varepsilon = \frac{\sigma}{E} + K \left(\frac{\sigma}{E} \right)^n \quad (3.26)$$

where:

- ε is the strain,
- σ is the stress,
- E is the Young's modulus,
- K and n are constants that depend on the material.

Looking at the right side of the equation, two terms can be identified: the first one, $\frac{\sigma}{E}$, is equal to the elastic strain; the second one, $K \left(\frac{\sigma}{E} \right)^n$, is the plastic strain and the two parameters K and n describe the hardening behavior of the material.

Introducing the yield strength, σ_y it is possible to rewrite the second term in a more convenient

way. A new parameter α related to K is defined as $\alpha = K \left(\frac{\sigma_y}{E}\right)^{n-1}$, so the second term becomes:

$$K \left(\frac{\sigma}{E}\right)^n = \alpha \left(\frac{\sigma_y}{E}\right) \left(\frac{\sigma}{\sigma_y}\right)^n$$

Hence the Ramberg-Osgood equation for the strain can be written as:

$$\varepsilon = \frac{\sigma}{E} + \alpha \left(\frac{\sigma_y}{E}\right) \left(\frac{\sigma}{\sigma_y}\right)^n \quad (3.27)$$

In this last form, the material behavior is linked to the value of the two constants, α and n . Moreover, looking at the formula, it comes out that plastic deformations theoretically exists also for very low stress levels, even if for low loading speed and average values of the constants, they are neglected if compared to the elastic ones. Only with the increase of the stress level over the yield point ($\sigma > \sigma_y$) plastic deformation increase its magnitude and become bigger than the elastic one.

The value of $\alpha \frac{\sigma_y}{E}$ can be seen as a yield offset, as shown in Figure 22. The value assumed by the constant n are usually greater than 5. Value for α , on the other side, are fixed by knowing the yield offset: it can be fixed a yield offset of 0.2% and from this find α by inverting the relationship:

$$\alpha \frac{\sigma_y}{E} = 0.002$$

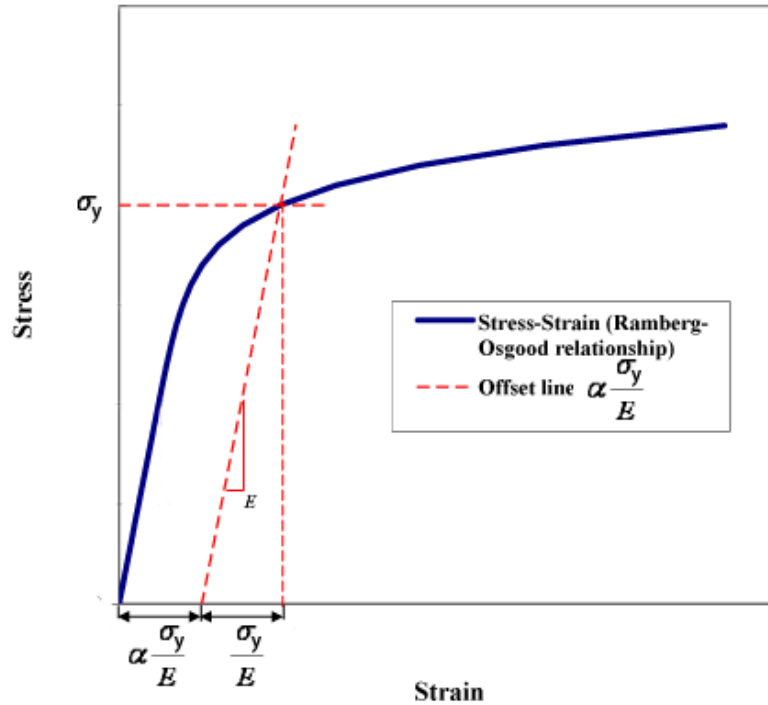


Figure 22: Stress-strain curve and offset line using Ramberg-Osgood model

3.7 Equations for annular disks in the plastic field (constant thickness)

It appears now clear that the constitutive equations developed in the previous sections are satisfied for the undeformed case rather than the deformed one, so they are not valid anymore in case plasticity has to be taken into account.

From the elastic stress analysis of an annular rotating disk it is known that, “as angular velocity is gradually increased, the yield limit is first reached in the interior surface”.^[17] As rotational speed increases, relevant plastic deformations with stable attributes may occur in the disk (starting from the inner radius moving toward the external rim), before the instability is verified

at the bursting speed.

The maximum elastic stress (at $r = a$):

$$\sigma_c = \frac{3 + \nu}{4} \rho \omega^2 \left(b^2 + \frac{1 - \nu}{3 + \nu} a^2 \right) \quad (3.28)$$

where a and b are respectively the inner and the outer radius, ρ is the density of the material, and ω is the angular velocity.

Under the hypothesis of assuming elastic strains negligible if compared to the plastic ones, and the use of *Tresca's yield criterion* and the associated *flow theory*, the **Initial Yielding**, the **Partial Yielding** and **Complete Yielding** can be studied.

Initial yielding

At the beginning of the chapter it was pointed out that for the considered axisymmetrical problem of a rotating disk, the principal stresses are the hoop stress σ_c , the radial stress σ_r and the axial stress σ_a . According to Tresca's yield criterion, none of the principal shearing stresses $\left(\frac{1}{2} |\sigma_c - \sigma_a|, \frac{1}{2} |\sigma_c - \sigma_r|, \frac{1}{2} |\sigma_r - \sigma_a| \right)$ can exceed a critical value that depends on the strain-hardening material.

Using a Poisson's ratio $\nu = \frac{1}{3}$, it is possible to find the critical speed ω_0 from the Equation 3.28:

$$\omega_0 = \left(\frac{6}{5b^2 + a^2} \frac{\sigma_y}{\rho} \right)^{1/2} \quad (3.29)$$

Partial yielding

For angular velocities that exceed the initial yielding one, ω_0 , but lower than speeds resulting in total plasticity of the disk, disks are characterized by both an elastic and a plastic region (Figure 23).

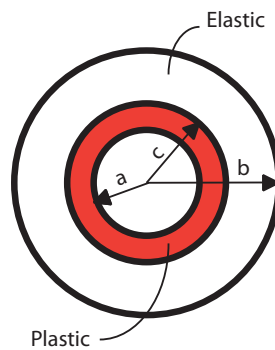


Figure 23: Partially plasticized disk

By replacing the maximum hoop stress σ_c with the yield stress σ_y , the equation of equilibrium for a uniform thickness hollow disk (Equation 3.14) becomes:

$$\frac{d}{dr} (r \sigma_r) - \sigma_y + \rho \omega^2 r^2 = 0 \quad (3.30)$$

The solution of this differential equation is given by:

$$r\sigma_r - \sigma_y r + \frac{\rho\omega^2 r^3}{3} + c_1 = 0 \quad (3.31)$$

Where the constant c_1 can be determined by imposing the boundary conditions. In case of an annular disk the boundary condition $\sigma_r = 0$ at $r = a$ provides the expression for c_1 and the Equation 3.30 becomes:

$$r\sigma_r - \sigma_y(r - a) + \frac{\rho\omega^2}{3}(r^3 - a^3) = 0 \quad (3.32)$$

while the stress in the plastic region is determined by considering the radius of the plastic region as $r = c$:

$$\sigma_r(r = c) = \frac{\rho\omega^2}{3} \frac{a^3 - c^3}{c} + \frac{c - a}{c} \sigma_y \quad (3.33)$$

In the elastic region, instead, the stresses can be found imposing the following two conditions into Equation 3.18:

- $\sigma_r = \sigma_r(r = c)$ at $r = c$;
- $\sigma_r = 0$ at $r = b$.

In this way the two integration constants c_1 and c_2 of Equation 3.18 can be found and, upon substitution, the stress field in the outer (elastic) region can be found:

$$\begin{cases} \sigma_r = \frac{c^2}{b^2 - c^2} \left(-1 + \frac{b^2}{r^2} \right) \sigma_c + \frac{\rho\omega^2}{8} (3 + \nu) \left(b^2 + c^2 - \frac{b^2 c^2}{r^2} - r^2 \right) \\ \sigma_c = -\frac{c^2}{b^2 - c^2} \left(1 + \frac{b^2}{r^2} \right) \sigma_c + \frac{\rho\omega^2}{8} (3 + \nu) \left(b^2 + c^2 - \frac{1 + 3\nu}{3 + \nu} r^2 + \frac{b^2 c^2}{r^2} \right) \end{cases} \quad (3.34)$$

Thus, by simply substituting in this last equation the value of yield strength σ_y instead of σ_c and this makes possible to describe the stress field of a rotating annular disk and the related rotational speed ω that cause yielding up to a specific radius c .

Complete yielding

It is, finally, possible to study the case in which the disk becomes fully plastic. The Equation 3.31 becomes:

$$\sigma_r - \sigma_y + \frac{\rho \omega^2 r^2}{3} + \frac{c_1}{r} = 0 \quad (3.35)$$

Applying the boundary conditions ($\sigma_r = 0$ for both $r = a$ and $r = b$) the constant c_1 is defined as:

$$c_1 = a \sigma_y - \frac{\rho^2 \omega^2 a^3}{3} \quad (3.36)$$

It is easy, then, to find the critical speed ω_1 at which all the disk is in the plastic region:

$$\omega_1 = \left(\frac{3 \sigma_y}{\rho} - \frac{b - a}{b^3 - a^3} \right)^{1/2} \quad (3.37)$$

Hence, knowing that in the plastic field the hoop stress has been considered constant and equal to the yielding stress, the equation for the radial stress in a fully plasticized disk can be written as follows:

$$\sigma_r = \left(1 - \frac{a}{r} - \frac{1 - a^2/b^2}{1 - a^3/b^3} - \frac{r^2}{b^2} \frac{1 - a/b}{1 - a^3/b^3} \right) \sigma_y \quad (3.38)$$

3.8 Failure criteria for rotating disks

The determination of the burst limit brought to the formulation of several theories and criteria that prescribe the procedure to determine the rotational speed that causes failure.

Among them, two are used in this thesis and, thus, are here presented: the Robinson's Criteria^[18], also called *average hoop stress criterion*; and the *critical strain criterion*.

3.8.1 Robinson Criterion

The Robinson Criterion is a semi-empiric method developed in order to easily find the burst speed in the *hoop mode* knowing the ultimate tensile strength, σ_{UTS} and the mean hoop stress, $\sigma_{c,mean}$. According to this criteria “burst occurs when the mean hoop stress on a disk section becomes equal to the nominal tensile strength of the material, determined from an uniaxial tensile stress”.^[19]

Then the mathematical formulation is:

$$\omega_{burst} = \omega \sqrt{\frac{\sigma_{UTS}}{\sigma_{c,mean}}} \quad (3.39)$$

It is important to point out, however, that the ultimate strength considered by the Robinson Criteria is the engineering stress, that differs from the true stress that, instead is used by Ansys. When passing from engineering stress to true stress, the following relations have to be applied:

$$\varepsilon_{true} = \ln(1 + \varepsilon_{eng})$$

$$\sigma_{true} = \sigma_{eng}(1 + \varepsilon_{eng})$$

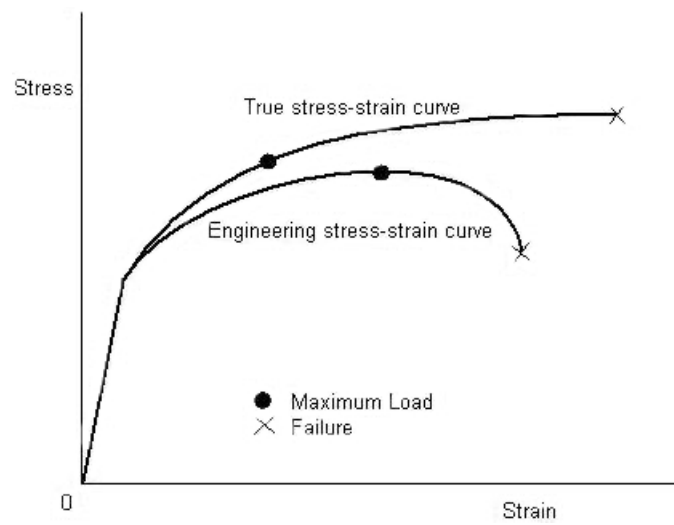


Figure 24: True stress versus engineering stress

Robinson formula has been modified in several ways. One of this is the Hallinan Formula, which extends the use of the Robinson criteria taking into account the maximum hoop stress, $\sigma_{c,max}$, introducing a factor S to weight the influence of the maximum stress over the mean stress.

$$\omega_{burst} = 0.95 \omega \left[S \left(\sqrt{\frac{\sigma_{UTS}}{\sigma_{c,mean}}} - \sqrt{\frac{\sigma_{UTS}}{\sigma_{c,max}}} \right) + \sqrt{\frac{\sigma_{UTS}}{\sigma_{c,max}}} \right] \quad (3.40)$$

This two criteria are actually degenerating into the same formula if the value of S is close to 1, such as for disks made of ductile materials.

So, in general, the concept of calculating the average stress is associated with the ductility of material, and no difference occurs between the two formulations; while if the disk is made of brittle material it is more appropriate to weight the influence of the maximum stress by applying the Hallinan Formula.

3.8.2 Critical strain criterion (inertial instability)

The critical strain criterion is usually associating burst with a critical deflection, hence the burst limit is fixed when a critical cumulated plastic strain is reached at any integration point. This criterion is then correlating directly burst with instability, that is going to be discussed in the following chapter. Instability, in fact, takes place whenever the spin softening is greater than the material hardening.

Considering a rotating disk that has to undertake the inertial load due to centrifugal force, an elevate deflection can cause the failure of the disk because of elastic instability. If strains are taken into account, for each increment of the angular velocity, or rather of the inertial load, the radial deflection u increases. Let r_0 denote the initial radius of a particle of the rotating disk,

and let r be the radius of the same particle when the angular velocity is ω . Then if the radial displacement is denoted by u , the following expression is valid:

$$r = r_0 + u$$

where both r and u can be considered as function of the independent variables r_0 and ω (note that the sign of ω is not affecting the result, hence it can be considered as a variable also its squared value, ω^2 , in order to get rid of the sign issue).

The centrifugal force, on its side, can be expressed, as done previously, by the formula:

$$\Phi_V = m\omega^2 r$$

So as the angular velocity ω increases, the effect produced is double: on one side the centrifugal load is increasing directly due to the increase of ω ; on the other side, the stresses induced by the rotation of the disk are causing a deflection that implies an additional increase of the centrifugal load.

Furthermore, it is important to point out that inertial instability is not related to the definition of a material curve in the plastic dominion: the increase of strain is not related to plasticity (even if in the plastic part strains are greater), but it can occur both in elastic and plastic dominion, since instability is actually regulated only by the stiffness of the materials. Hence, if it might be not so common to find metallic structures that become unstable in the elastic field (because of usually very high stiffness), when instead the yielding point is passed, instability

acquires great importance due to the gradual reduction of the stiffness in the hardening path of the stress-strain curve that fosters the instability because of the double effect of increasing inertial load and decreasing stiffness at each increment of angular velocity.

The drawback of this criterion is that is usually very complex to formulate a mathematical expression that takes into account the spin softening, the material hardening and condition of inertial instability. For this reason, in this thesis, the *Large Displacement* option in the Finite Element Method is applied to find the burst limit.

CHAPTER 4

FINITE ELEMENT MODEL USING ANSYS

This chapter goes on a general overview of the *Finite Element Method* describing the non linear calculation which is performed by the commercial code Ansys in order to solve static problems that are using the *Large Displacement* option.

The first part of the chapter is focusing on the general equation that are used in a finite element calculations, while the following sections are focused on the main settings used in order to run the simulations both in the 2D case and the 3D one.

4.1 The finite element method general formulation

A Finite Element analysis is based, as said in Section 2.5, on the division of the entire domain into smaller elements that can be easily solved.

The unknowns of the finite element calculation are the nodal coordinates $\{q\}$: those depend on the type of element used and assume a finite value different from zero if any kind of external load is applied on the discretized structure. The global stiffness matrix, $[K]$ is generated by assembling all the local (elemental) stiffness matrices that characterize the elements. The stiffness matrix, $[K]$, can be determined by applying the principle of virtual work to the deformation energy.^[20]

Calling the *Cauchy stress tensor* $[\boldsymbol{\sigma}]$ and the *Strain tensor* $[\boldsymbol{\varepsilon}]$, with $\varepsilon_{ij} = \frac{1}{2} \left(\frac{\partial u_i}{\partial x_j} + \frac{\partial u_j}{\partial x_i} \right)$,

it is possible to write the potential deformation energy as:

$$W = \frac{1}{2} \int \sigma_{ij} \varepsilon_{ij} dV \quad (4.1)$$

Deformation, and thus also strain, can be written as a linear combination of the nodal coordinates, by simply considering the *Shape functions matrix* $[N]$: $\{\delta(x)\} = [N] \{q\}$. So, $[B] = \nabla [N]$ is the matrix that expresses the relationship between strains and nodal coordinates, such that $[\boldsymbol{\varepsilon}] = [B] \{q\}$.

On the other side, it is possible to write a matrix $[D]$ that contains all the information about the material behavior and allows to define the stress-strain relationship in the matrix form: $[\boldsymbol{\sigma}] = [D] [\boldsymbol{\varepsilon}] = [D] [B] \{q\}$. In this way the equation of the elastic work (Equation 4.1) can be rewritten as:

$$W = \frac{1}{2} \int [\boldsymbol{\varepsilon}]^T [\boldsymbol{\sigma}] dV = \int \{q\}^T [B]^T [D] [B] \{q\} \quad (4.2)$$

Since the vector of nodal coordinates does not depend on the coordinates x, y, z it is possible to put it outside from the integration, hence:

$$W = \frac{1}{2} \{q\}^T \left(\int [B]^T [D] [B] \right) \{q\} = \{q\}^T [K] \{q\} \quad (4.3)$$

Where $[K] = \int [B]^T [D] [B]$ is the *Stiffness matrix*.

The formulation shown above is defining the *Stiffness matrix* that is used for elastic analysis or elasto-plastic calculation whenever only *Small Displacement* is taken into account. The deformation energy considered, in fact, is not taking into account the effect of non-linearity. As soon as the *Large Displacement* option is activated in Ansys, the calculation of the *Stiffness matrix* $[K]$ has to be carried out considering the non-linear effects: in an elasto-plastic analysis, given a material curve to the software, the matrix is then updated every substep considering several parameters, such as *yield criterion*, *hardening rule* and *relative flow rule*. The deformation energy, thus, has an additional term that influence the formulation of $[K]$ as shown in Section 3.6 of the Help of Ansys^[21]:

$$W_{LD} = \frac{1}{2} \int \sigma_{ij} \varepsilon_{ij} dV + \int \sigma_{ij} \left(\frac{\partial u_k}{\partial x_i} \frac{\partial u_k}{\partial x_j} - 2\varepsilon_{ik}\varepsilon_{jk} \right) dV \quad (4.4)$$

The Equation 4.4 shows that the Ansys consider an additional term when the LD option is activated, complicating the formula used in the SD analysis (Equation 4.1), so that it is possible to consider the contribution of the elastic deformations. This redefines the definition of the *Stiffness matrix*, hence the problem becomes not linear.

The second part of the integral represents the *Stress stiffening matrix*, $[S]$, that allows to update the definition of the stiffness matrix taking into account both the loading condition and the deformation status. The solving equation for the two cases is:

$$\begin{aligned} \text{Small Displacement:} \quad & [K] \{q\} = \{P\} \\ \text{Large Displacement:} \quad & ([K] + [S]) \{q\} = \{P(q)\} \end{aligned} \quad (4.5)$$

In the study of rotating structures, then, the formulation included in the *Large Displacement*, much more sophisticated than the one of *Small Displacement*, since it includes also the effects of deformations, is preferable upon the *Small Displacement*. It is more conservative, then, to use this kind of solution option, letting the software consider all the non linear terms that influence the results in terms of burst speed and stress distribution, obtaining also a better correlation of those results with the material curve, as it will be shown later on in this thesis.

4.2 Setup of a finite element analysis using Ansys

4.2.1 Preprocessing: model generation and mesh properties

The first step to go through in order to perform a FE analysis is to set up a geometrical model that represents the structure to study. In this thesis two different models were created: one in two-dimensions, that was using the axisymmetric option allowed by Ansys on certain elements; the other in three-dimensions, instead, was modeled using the cyclic symmetry feature.

Ansys operations are divided into modules and the one dedicated to the model creation and meshing are contained into the *Preprocessor* module. In this section, then, the main commands required to model a component in Ansys are listed:

- **Modeling:** In the modeling menu are available a set of instructions useful to create a geometry directly in Ansys. After the creation of keypoints, lines, areas and volumes can be built on them or directly giving their parameters. Other modeling operations can be carried out in the *Operate* section. Here the extrusion command is used when dealing with

3D models and is used for example to extrude areas about an axis. *Booleans* operations are very used to finalize the geometry: they allow to make operations like adding or subtracting areas and volumes, or dividing them into parts.

- **Element Type:** is the section used to add, modify or delete the elements used to mesh the component and perform on them the finite element calculation. The elements are classified by number of nodes and their configuration. Basically three kind of elements were used in the analysis that were carried out during this thesis.

For the bi-dimensional study, the element *Plane42*, which uses four nodes with two degrees of freedom each, was adopted using the option for axisymmetry.

For the three-dimensional model, instead, two elements have to be set up: *Mesh200* in its 8-noded quadrilateral configuration and *Solid95*, which is using a brick with 20 nodes.

- **Material Props:** here the material model is defined. For structural analysis it is possible to set the density (in ton/mm^3 if the metric system is used), the elastic properties (Young's modulus and Poisson's ratio) choosing Linear Isotropic behavior, and the non linear path indicating a maximum of 100 discrete point of the $\sigma - \varepsilon$ curve.
- **Meshing:** In this section is possible to set up all the options to use in order to obtain the desired meshing grid to discretize the body. The *MeshTool* is enclosing most of this options in a GUI that easily allows to set up the number of divisions of a line (the equivalent of the command *LESIZE*), or the desired dimensions of the areal elements.

4.2.2 Processing: load increasing simulations

After having correctly defined the geometry and the mesh on which the analysis is going to be performed, the set up of the FEM software requires to select the correct solution options and to define the boundary conditions. All those parameters are defined in the ***Solution*** module. Boundary conditions are indicated in the *Define Loads* menu, in which it is possible to fix the displacement on one side and apply loads on the part.

The *Analysis Type* menu, instead, is containing all the information regarding the solution options to adopt for the calculation, which are:

- *Small displacement*: tells the software to ignore the deflections of the structure when calculating the stress state at different load steps. Ansys, in fact, tends to reach the equilibrium under external loads using a time-dependent technique, in which the final condition is reached after an initial transient in which an increasing load is applied by dividing the total one in substeps. The solution, then is evolving in time, but if this option is selected, no information about deformation is taken into account in the iterative process.
- *Large displacement*: by selecting this solution option, instead, all the deformations that are occurring in the structure at each substep of the loading in the time-dependent solution process are considered. Considering the effect of deformations implies that large strains are affecting the calculation of the stress state of the structure.

When dealing with rotating structures, as done in this thesis, the centrifugal load increases at each substep, which correspond to increasing fraction of the imposed angular velocity.

This cause an increase of radial deformation of the disk, the so called “*spin softening*”, and this deformation is considered as an input in following substeps. Another effect, the “*stress stiffening*”, is also considered when using the *Large displacement*: the stiffening of the structure is a consequence of having set a plastic material curve, so a higher load is implying higher stiffness.

Both these effects are then considered by Ansys when the stiffness matrix is updated passing from a substep to the following one.

- *Automatic Time Stepping*: this options allows to control the division in substeps that the software operate before performing the equilibrium calculation. If the entry “OFF” is chosen, the user is in charge to decide the total number of substeps that have to be considered in the analysis and the software is equally spacing the load increments upon them. Otherwise, if the entry “ON” is selected, three parameters have to be set up: “*Number of substeps*” is the value used for the first division; “*Max no. of substeps*” stand for the maximum number of substeps that Ansys can use for the analysis, or also the smallest increment that it will be used during the iterative process (usually a much higher number than the other two); “*Min no. of substeps*” is, instead, the minumum number of substeps to consider for the analysis. This kind of solution option is more refined of the first one, since there is an increasing number of divisions around the instability point. A third option, “*Program Chosen*”, lets the software to decide by it self which of the two methods use after having imposed the three parameters listed above.

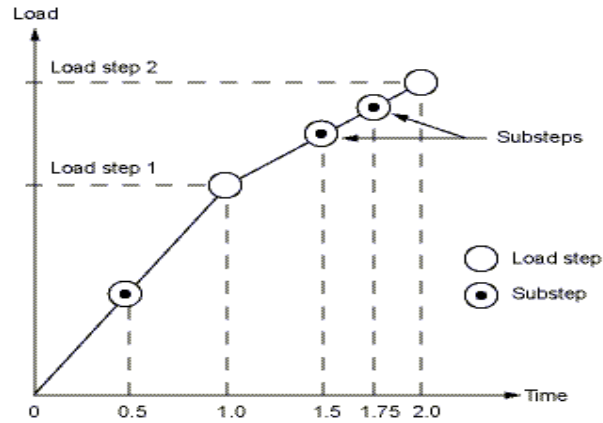


Figure 25: Loading sequence and division in substeps

- *Nonlinear Options:* here Ansys gives the user the possibility to choose between two methods to solve non-linear problems: the *Newton-Raphson* method and the *Arc Length*. Both these methods can be applied in a static analysis, and are based on bisection if convergence is not reached in the first iteration. The *Newton-Raphson* method is basically finding the zero upon linear approximations with the tangent at the curve and the value found converges if the error is below a threshold value. The *Arc Length*, instead, is looking for a converging solution to be inside a reference radius initially calculated as $r = (Total\ load) / (Max\ no.\ of\ substeps)$ and then applying bisection if convergence is not reached.

For each substep the maximum number of iterations is fixed within 15 and 26 iterations by the software, so the analysis is stopped if convergence is reached after all the loading increments, or the convergence is not found after the selected number of iterations for the

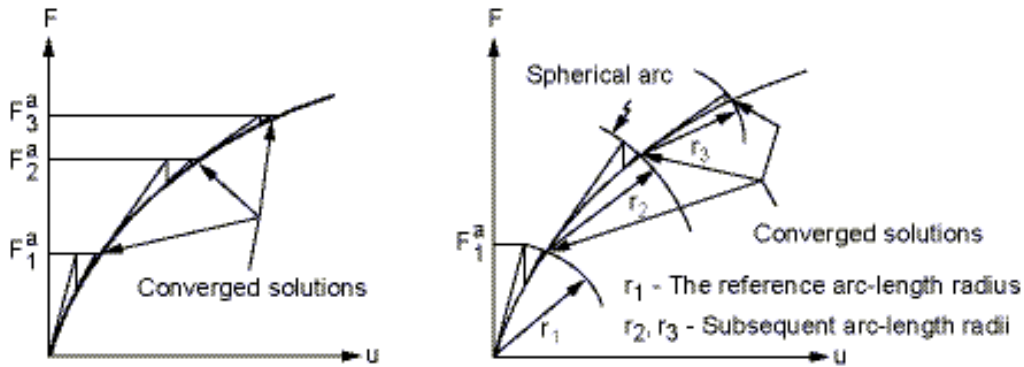


Figure 26: Newton-Raphson method vs arc length method

lowest loading increment (minimum multiplier).

A good setup of the options listed above allows to optimizing the time required for obtaining a sufficiently refined solution. It is recommended to use the *Arc Length* especially when the force-displacement function is not anymore injective or surjective, or if dealing with a stability problem. In those cases, in fact, the *Newton-Raphson* method is usually failing in finding the convergence value.

4.3 Elasto-plastic calculations in Ansys

How is convergence reached when external loads cause an equivalent stress greater than yielding?

The main issue in an elasto-plastic analysis is to update the stiffness matrix $[K]$ when a material

curve is considered, so in the non linear path after yielding. The stiffness matrix in a non linear analysis is not constant anymore, but is function of the nodal coordinates $\{q\}$, hence $[K] = f(\{q\})$.

So, the non linear problem can be written as:

$$[K(q)] \{q\} = \{p\} \quad (4.6)$$

The convergence of the final solution is obtained by iterations, recalculating each time the value of $\{q\}_i$ and, consequently, updating the value of $[K]$ until it has:

$$[K(q)] \{q\} - \{p\} = \{p_n\} - \{p\} = 0 \quad (4.7)$$

where $\{p_n\} - \{p\}$ is the deficit between the nodal load vector at each iteration, $\{p_n\}$, and the external load, $\{p\}$.

In reality, Ansys does not set at zero the convergence value, instead a series of parameters are defined to set the convergence condition as follows:

$$\| \{p_n\} - \{p\} \| = \delta_{tol} p_{rif} \quad (4.8)$$

where p_{rif} is the norm of the nodal loads vector which increases at each substep.

The plot in Figure 27, where u stands for the nodal deflections q_i , shows how the stiffness matrix $[K]$, represented by the tangent, is updated at each iteration. The Newton-Raphson

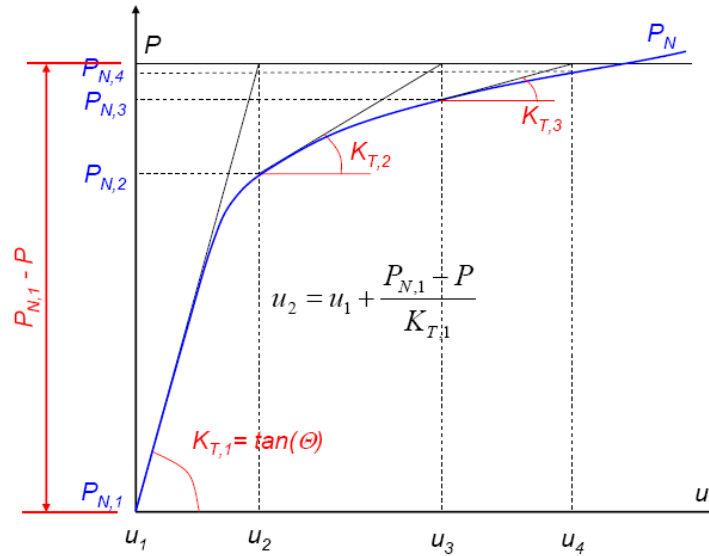


Figure 27: Update of the matrix $[K]$ at each iteration

method is here applied choosing in Ansys the option for: “full” method, which updates $[K]$ at each iteration in the plastic field (it is also possible to store the initial stiffness value requiring more, but less demanding, iterations at each substep); or “auto”, that lets the software to decide whether to recalculate the value of $[K]$ or not in a mixed way.

It is now necessary to define some elements on which an elastoplastic analysis is based and explain briefly how Ansys commands elaborate this analyses using such components: *yield criterion*, *hardening rule*, *flow rule*.

First of all, it is important to say that Ansys places automatically the yielding point where the proportionality between σ and ε in the material curve (implemented using the *MELA*, *MISO* or

MKIN commands) is interrupted. Before starting the solution process, however, the software checks that the Young's modulus, or in other words the slope of the first part of the curve, is actually corresponding to the calculated value from the yield point calculation.

The *yield criterion* allows to state if a certain stress state is corresponding to an elastic or to a plastic working condition. It consists in calculating the equivalent stress using Tresca or von Mises, and comparing the obtained value with the one of σ_y . Called σ_1 , σ_2 and σ_3 the three principal stresses, the equivalent stress is:

$$\begin{aligned} \text{Tresca: } \sigma_{eq} &= \max(|\sigma_1 - \sigma_2|, |\sigma_1 - \sigma_3|, |\sigma_2 - \sigma_3|) \\ \text{von Mises: } \sigma_{eq} &= \frac{1}{\sqrt{2}} \sqrt{(\sigma_1 - \sigma_2)^2 + (\sigma_1 - \sigma_3)^2 + (\sigma_2 - \sigma_3)^2} \end{aligned} \quad (4.9)$$

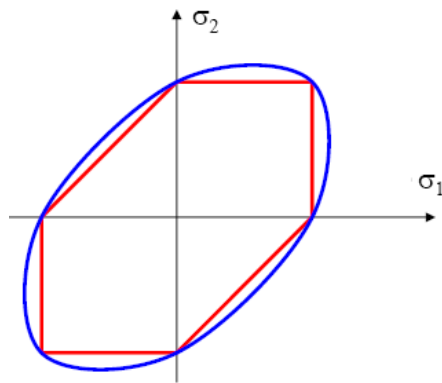


Figure 28: Yield criteria

In Figure 28 the two criteria are compared: the red line shows the equivalent stress calculated using Tresca, while the blue line is referring to the von Mises criterion.

The yielding function can, then, be formulated as follows:

$$F(\sigma_{eq}) = \sigma_{eq} - \sigma_0 \quad (4.10)$$

The value of σ_0 in plastic field is updated every iteration and it becomes as much bigger than σ_y as the hardening becomes greater, it increases, then, with the plastic deformation. If we are in the plastic field, the value of the yielding function F can be zero or less than zero, but the second condition is not physically possible, so it is corrected by other iterations.

The *hardening rule* defines how the value of σ_0 has to be updated with increasing plastic deformation ε_p : σ_0 is a threshold value that increases when σ_{eq} falls in the plastic field.

At this point the differences between the options used in order to define the material curve in Ansys arise.

If the von Mises criterion is applied, σ_0 is represented by the blue ellipse in Figure 28: if the commands *MISO* (*multilinear isotropic hardening*) or *MELA* (equivalent to *MISO* in loading), as plasticization increases, the ellipse is increasing in dimension of the same quantity in each direction (Figure 29(a)) and the yielding function is the one defined in Equation 4.10; while if the option *MKIN* (*multilinear kinematic hardening*) is used, the yielding surface is translated

along a principal direction (Figure 29(b)).

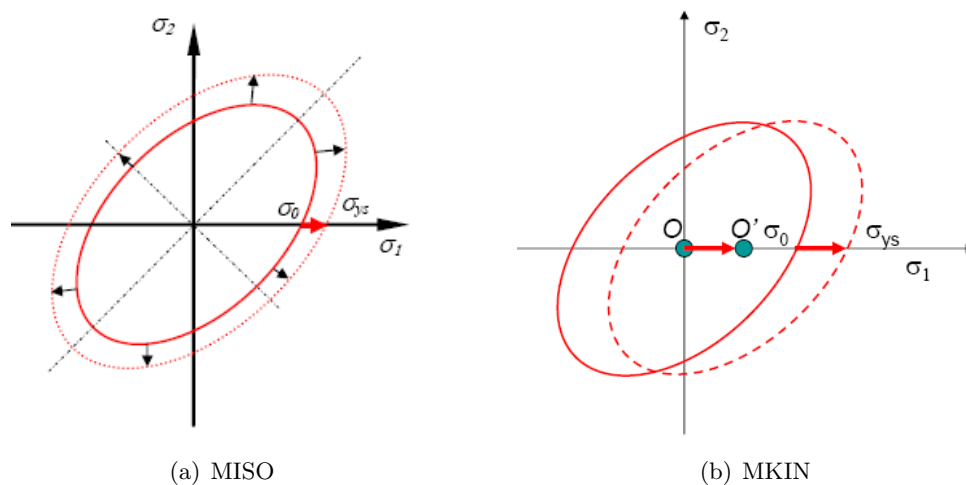


Figure 29: Models for updating σ_0

Finally, the *flow rule* is in charge of evaluating the increment of plastic deformation ε_p correlated to a stress increment.

In elasto-plastic field, this increment is usually expressed in an incremental form by the Prandtl-Reuss relationship:

$$\{d\varepsilon_p\} = d\lambda \left\{ \frac{\partial F(\sigma_{ij})}{\partial \sigma_{ij}} \right\} \quad (4.11)$$

Where $d\lambda$ is called plastic multiplier and is the factor that allows to amplify the yielding surface after an increment of stress. Hence the plastic multiplier is the one in charge of updating σ_0 .

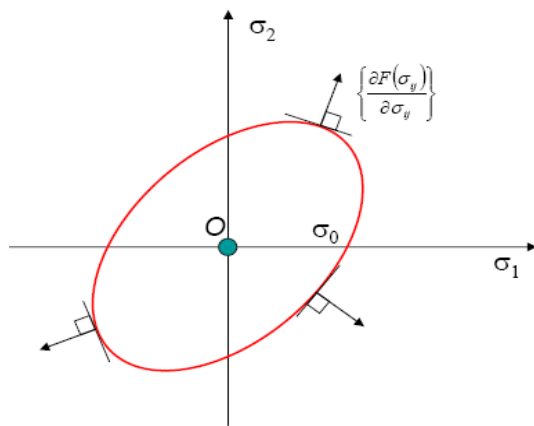


Figure 30: Amplification of the allowable ellipse due to cumulated plastic deformation

For almost all metallic materials, it has $F = Q$, where Q is the plastic potential, hence:

$$F(\sigma_{eq}, \varepsilon_p) = \{\sigma_{eq}\}^t \{d\varepsilon_p\} \quad (4.12)$$

Knowing that:

$$\{d\sigma\} = [D] \{d\varepsilon_p\} = [D] (\{d\varepsilon\} - \{d\varepsilon_p\}) \quad (4.13)$$

And that, in order to be on the plastic boundary it has to be verified the following compatibility expression:

$$dF = \left\{ \frac{\partial F}{\partial \sigma} \right\}^t d\sigma + \left\{ \frac{\partial F}{\partial \varepsilon_p} \right\} d\varepsilon_p = 0 \quad (4.14)$$

It is possible to combine those equations in order to calculate the plastic multiplied $d\lambda$:

$$\left\{ \frac{\partial F}{\partial \sigma} \right\}^t [D] \{d\varepsilon\} - \left\{ \frac{\partial F}{\partial \sigma} \right\}^t [D] d\lambda \left\{ \frac{\partial F}{\partial \sigma} \right\} + \left\{ \frac{\partial F}{\partial \varepsilon_p} \right\}^t d\lambda \left\{ \frac{\partial F}{\partial \sigma} \right\} = 0 \quad (4.15)$$

By inverting this last equation it is easy to get the expression of $d\lambda$:

$$d\lambda = \frac{\left\{ \frac{\partial F}{\partial \sigma} \right\}^t [D]}{\left\{ \frac{\partial F}{\partial \sigma} \right\}^t [D] \left\{ \frac{\partial F}{\partial \sigma} \right\} - \left\{ \frac{\partial F}{\partial \varepsilon_p} \right\}^t \left\{ \frac{\partial F}{\partial \sigma} \right\}} \cdot \{d\varepsilon\} \quad (4.16)$$

The value of this plastic multiplier, guarantees that after an infinitesimal increment of deflection, the point expressing the final stress state is still laying on the yielding surface, which has been updated. This updating process is carried out by substituting the value of $d\lambda$ calculated numerically using finite differences into the Equation 4.13, obtaining:

$$\{d\sigma\} = [D] d\varepsilon = \left([D] - \frac{[D] \left\{ \frac{\partial F}{\partial \sigma} \right\}^t \left\{ \frac{\partial F}{\partial \sigma} \right\} [D]}{\left\{ \frac{\partial F}{\partial \sigma} \right\}^t [D] \left\{ \frac{\partial F}{\partial \sigma} \right\} - \left\{ \frac{\partial F}{\partial \varepsilon_p} \right\}^t \left\{ \frac{\partial F}{\partial \sigma} \right\}} \right) d\varepsilon = [D]_i d\varepsilon \quad (4.17)$$

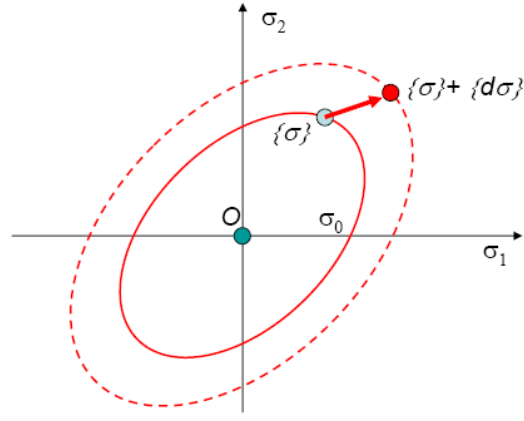


Figure 31: Update of the yielding surface

From Equation 4.17 it is clear that the updated stiffness $[D]_i$ is reduced by the subtractive term that depends on plastic deformation ε_p .

Hence, the next step is to recalculate the stiffness matrix by simply applying its definition:

$$[K]_i = \int [B]^T [D]_i [B] \quad (4.18)$$

This showed shortly the procedure applied by Ansys to update the stiffness matrix in order to adapt the material properties to the loading conditions and, consequently, when the material is working in the plastic field, the stiffness is progressively reduced as prescribed by applied material curve. The procedure showed above is based on an iterative method, so the calculation is repeated many times, until the convergence condition, which implies that the $F(\sigma_0, \varepsilon_p) = 0$, is fulfilled.

When the *Large Displacement* option is enabled, finally, the contributes of spin softening and stress stiffening have to be added to the global stiffness matrix as said before.

CHAPTER 5

COMPUTATION OF INERTIAL INSTABILITY OF ROTATING DISKS

The overspeed burst of rotating disk has been discussed in several different ways during the years, and, as mentioned in Chapter 2, the modes of fracture can be various and depend on the loading conditions and on the presence of notches that cause fatigue failure.

If only the inertial loads are taken into account, it can be demonstrated that the reason that brings to burst of the disk is the inertial instability of the material. This is a strain dominated phenomenon and it is directly related to the material properties and the stiffness both in the elastic and plastic fields.

It was verified experimentally (Percy et al., 1974) that the failure of a disk can be due to instability of the material, such that failure can occur for values of the equivalent stress, σ_{eq} , lower than the ultimate strength, σ_{UTS} . The exponential increase of the inertial forces, or rather centrifugal loads, in fact, causes a fast increase of deformation until a condition of instability is reached and, finally, it culminates with burst.^[22]

In Figure 32(a) and 32(b) it is possible to look at those experiments, and notice how a disk that rotates at speeds slightly below the calculated instability burst speed shows evident plastic deformation near the bore. The necking near the bore is the macroscopic effect of the deformations that rapidly increase at high rotational speed and explains why it should be important to consider this kind of behavior when developing a formula for safety factor against burst.

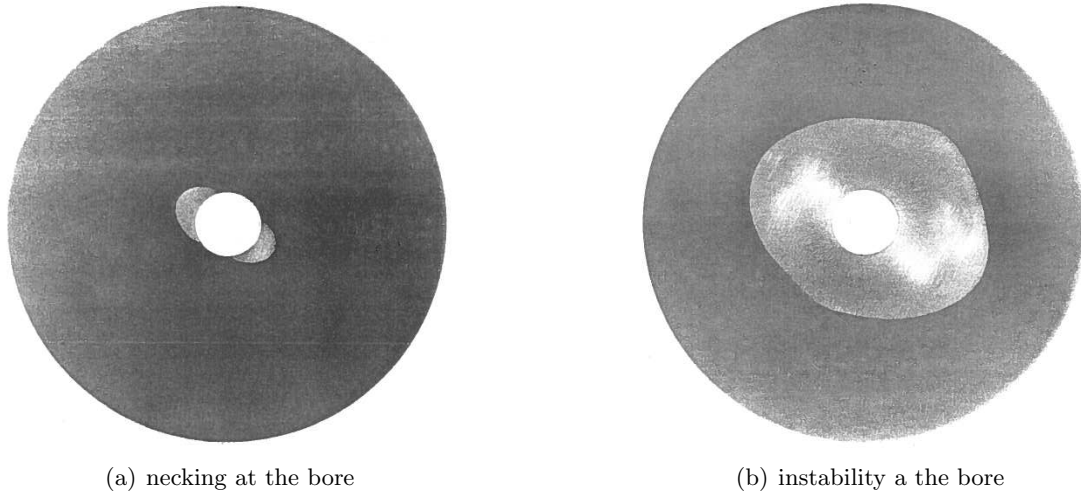


Figure 32: Plastic deformations prior to fracture

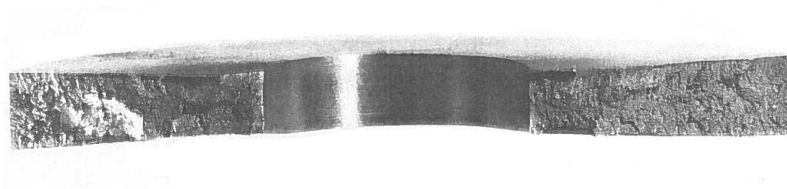


Figure 33: View of the fracture surface of a disk showing evident necking

The instability approach totally redefines the burst limit analysis, since all the other analytic criteria are considering only the tensile strength of the material as the governing parameter to explain the phenomenon. Instead, the study on inertial instability revealed that fracture is preceded by a condition of tensile instability: this condition is strain dominated and, there-

fore burst strictly depends on the material behavior in plastic field as pointed out in Section 3.8.

The effects of inertial instability have been considered for different types of materials: the work done by Brunelle et al. (1971) is taking into account beams and disks made of isotropic materials^[23], while Tutuncu (2000) focused onto orthotropic materials.^[24]

Following the mathematical approach used by Brunelle, the analytic results obtained for the instability rotating beams and disks and the numerical results obtained by using the FEM code Ansys, were compared.^[2] Thus, the following sections the two examples of the rotating beam with a tip mass and the rotating disk are reported, so that it can be possible to show the quality of a bi-dimensional model created using Ansys.

Eventually, it is important to remind that instability, as confirmed by the following comparisons, can occur both in elastic and plastic dominion, since it is regulated only by the stiffness of the materials. In particular the material set for the comparison is only considering a linear elastic trend in order to investigate inertial instability.

5.1 Rotating beam with tip mass

The easiest model to study for inertial instability is a beam with a mass on its tip, which rotates around a axis perpendicular to the beam it self.

Brunelle considers the beam as a one-dimensional problem characterized by mass per unit length m , length l , and mass on tip called M , while the rotational speed is ω and the radial displacement u .

The radial equilibrium, then, is rather easy to write as a function of the non-dimensional parameter $\xi = u/l$:

$$E A u_{xx} = m l \omega^2 (\xi l + u) \quad (5.1)$$

where the term $m l \omega^2 u$ is the one that is taking into account the spin softening, or rather the additional centrifugal load given by the deformation u in the radial direction.

Considering the following boundary conditions:

$$\begin{cases} u(0) = 0 \\ u_x(1) = \frac{M l}{A E [l + u(1)] \omega^2} \end{cases} \quad (5.2)$$

the equation Equation 5.1 yields to the solutions for displacement u and stress σ reported below, where k is defined as $k = \frac{m l \omega^2}{E A}$:

$$u(\xi) = l \left\{ \left[\frac{\sin k\xi}{k \cos k (1 - (m l/M) k \tan k)} \right] - \xi \right\} \quad (5.3)$$

$$\sigma(\xi) = E \left\{ \left[\frac{\cos k\xi}{\cos k (1 - (m l/M) k \tan k)} \right] - 1 \right\} \quad (5.4)$$

On the other side, the classical values for $u(\xi)$ and $\sigma(\xi)$, where no spin softening effect is considered, are used as reference and are here distinguished by the subscript *cl*.

$$u(\xi)_{cl} = k^2 l \left[\frac{M}{m l (6 - k^2)} + 3 - \xi^2 \right] \xi/6 \quad (5.5)$$

$$\sigma(\xi)_{cl} = k^2 E \left[\frac{M}{ml(6 - k^2)} + 3 - 3\xi^2 \right] / 6 \quad (5.6)$$

It is noticed from Equation 5.3 and Equation 5.4 that $u(\xi)$ and $\sigma(\xi)$ tend to infinite if $k \tan k = ml/M$, while no instability points are prescribed by Equation 5.5 and Equation 5.6. The evolution of σ at the root ($\xi = 0$) has been calculated for different values of ml/M , making it possible to draw the graph of σ/σ_{cl} over the variable k .

From the Figure 34 it is possible to see that the ratio σ/σ_{cl} tends to diverge as a critical value

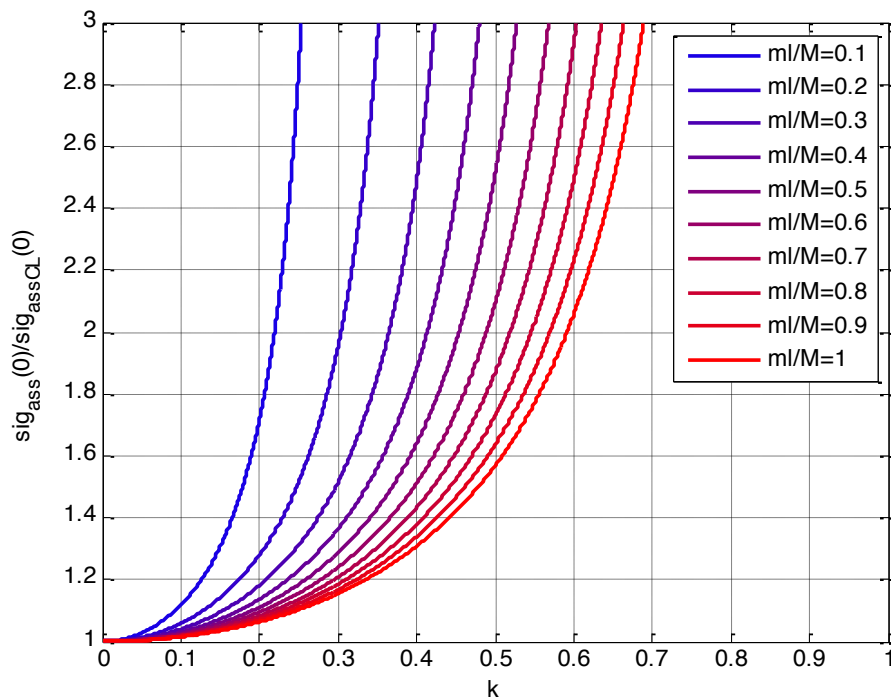


Figure 34: Divergence of stresses for varying k and mass rates

of k is reached (asymptotic behavior). So the values of k_{crit} have been found for each mass rate.

TABLE II: CRITICAL VALUES OF K VS MASS RATE

ml/M	k_{crit}
0.05	0.2218
0.1	0.3109
0.2	0.4328
0.3	0.5216
0.4	0.5932
0.5	0.6531
0.6	0.7049
0.7	0.7505
0.8	0.7909
0.9	0.8273
1	0.858

The results obtained by simply applying this mathematical formulation can be compared with the finite element analysis implemented with Ansys using for this purpose the Large Displacement model (LD model) and 400 substeps. The model was set up using the element *LINK8* for the beam, and the *MASS21* for the mass, assigning the following dimensional parameters $E = 207600MPa$, $A = 25mm^2$, $M = 10^{-3}tonn$, $L = 1000mm$, letting the density ($\rho = m/A$) to vary as it governing parameter for the mass rate defined above (ml/M).



Figure 35: Ansys model for the rotating beam with mass on tip

Looking at the values reported in the Table III and the plot in Figure 36, it is possible to deduce that the numeric model developed using Ansys in the *Large Displacement* configuration is producing the same results of the analytic formulation in the case of the rotating beam.

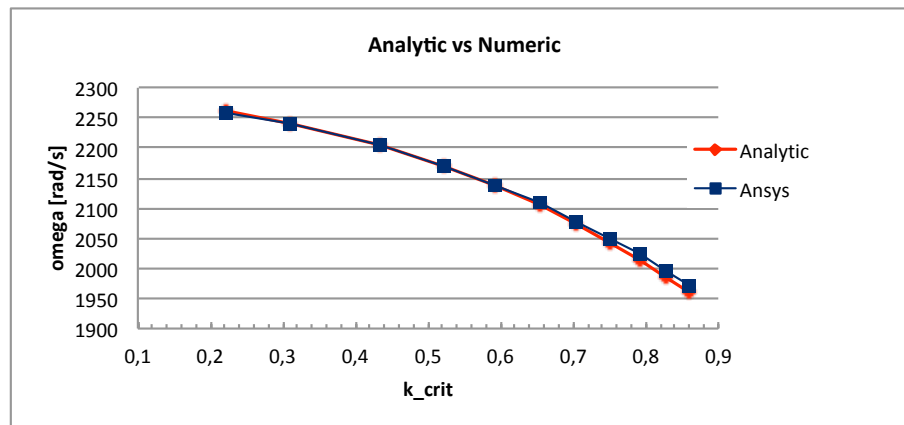


Figure 36: Comparison between analytic and numeric results

TABLE III: INSTABILITY BURST SPEED OF A ROTATING BEAM: COMPARISON BETWEEN ANALYTIC AND NUMERIC RESULTS

ml/M	k_{critic}	$\omega_{burst_analytic} [rad/s]$	$\omega_{burst_Ansys} [rad/s]$
0.05	0.2218	2261.80	2258
0.1	0.3109	2227.19	2240
0.2	0.4328	2196.65	2204
0.3	0.5216	2168.08	2171
0.4	0.5932	2129.89	2138.8
0.5	0.6531	2098.43	2108
0.6	0.7049	2068.61	2078
0.7	0.7505	2040.48	2050
0.8	0.7909	2010.62	2023
0.9	0.8273	1982.13	1997
1	0.858	1957.91	1972

5.2 Rotating disk of uniform thickness

The same procedure has been followed for a rotating disk, considering the spin softening effect in the analytic formulation and properly setting the problem with the FE code. This allow to finally test the fidelity of the numerical model if it is compared with the formula that describe burst for instability.^[2]

The stress-strain relations for a generic orthotropic material in the matrix formulation are expressed as:

$$\begin{Bmatrix} \sigma_r \\ \sigma_c \\ \tau_{rC} \end{Bmatrix} = \begin{bmatrix} A_{11} & A_{12} & 0 \\ A_{21} & A_{22} & 0 \\ 0 & 0 & A_{66} \end{bmatrix} \begin{Bmatrix} \varepsilon_r \\ \varepsilon_c \\ \gamma_{rC} \end{Bmatrix} \quad (5.7)$$

If the material is assumed to be isotropic, then $A_{11} = A_{22} = E/(1 - \nu)$ and $A_{12} = A_{21} = E\nu/(1 - \nu)$.

The effect of spin softening can be added to equation of radial equilibrium:

$$\rho\omega^2(r+u) + \frac{d\sigma_r}{dr} + \frac{\sigma_r - \sigma_c}{r} = 0 \quad (5.8)$$

This equation can be rewritten as function of the displacement u as:

$$\frac{r^2 d^2 r}{du^2} + \frac{r du}{dr} + \left[\Omega^2 \left(\frac{r}{b} \right)^2 - 1 \right] u = \frac{-\Omega^2 r^3}{b^2} \quad (5.9)$$

where

- $\Omega^2 = (1 - \nu^2) \rho\omega b^2/E$;
- a is the radius at the bore;
- b is the radius at the rim.

Since the bore is considered to be fixed, while the rim can deform, the following boundary conditions can be used: $u(a) = \sigma(b) = 0$. Then, the solution of the Equation 5.9, which is a non-homogeneous Bessel equation is:

$$u/b = A J_1(\Omega r/b) + B Y_1(\Omega r/b) - r/b \quad (5.10)$$

Where J_1 and Y_1 are respectively the first and second order Bessel's functions, while A and B are the two integration constants and, with the boundary condition expressed above, they are equal to:

$$A = [(1 + \nu) Y_1 (\Omega a/b) - (a/b) \Omega Y_0 (\Omega) + (a/b) (1 - \nu) Y_1 (\Omega)] / C \quad (5.11a)$$

$$B = [(a/b) \Omega J_0 (\Omega) - (a/b) (1 - \nu) J_1 (\Omega) - (1 + \nu) J_1 (\Omega a/b)] / C \quad (5.11b)$$

$$C = Y_1 (\Omega a/b) [\Omega J_0 (\Omega) - (1 - \nu) J_1 (\Omega)] + J_1 (\Omega a/b) [(1 - \nu) Y_1 (\Omega) - \Omega Y_0 (\Omega)] \quad (5.11c)$$

Once that the values for a and b have been fixed, the constants reported above are only function of the parameter Ω which depends from the angular velocity ω .

Also the stresses can be expressed in the non dimensional form as function of the the same parameters:

$$\begin{aligned} (1 - \nu^2) \sigma_r / E = A [\Omega J_0 (\Omega r/b) - (b/r) (1 - \nu) J_1 (\Omega r/b)] \\ + B [\Omega Y_0 (\Omega r/b) - (b/r) (1 - \nu) Y_1 (\Omega r/b)] - (1 + \nu) \end{aligned} \quad (5.12a)$$

$$\begin{aligned} (1 - \nu^2) \sigma_c / E = A [(b/r) (1 - \nu) J_1 (\Omega r/b) + \nu \Omega J_0 (\Omega r/b)] \\ + B [(b/r) (1 - \nu) Y_1 (\Omega r/b) + \nu \Omega Y_0 (\Omega r/b) \Omega] - (1 + \nu) \end{aligned} \quad (5.12b)$$

As done in the previous section for the rotating beam, the the hoop stress at the bore, $\sigma_c(a)$ can be calculated for different form factors $\gamma = a/b$. The plot in Figure 37 shows the tendency of the ratio between the hoop stress calculated as shown before and the classical one (without spin softening effect) as the dimensionless parameter Ω is varying. This results can be compared

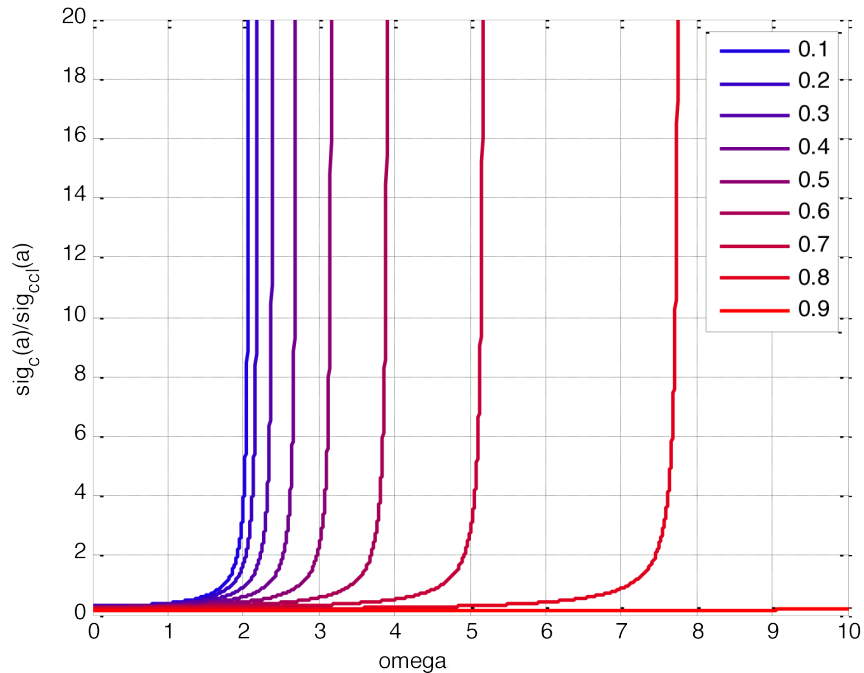


Figure 37: Divergence of stresses for different Ω and geometry rates

with the one calculated using Ansys. As done before for the beam, some real geometry values have to be set to allow the calculation, hence $E = 207600 \text{ MPa}$, $\rho = 8219 \cdot 10^{-12} \text{ tonn/mm}^3$, $\nu = 0.3$, $b = 1000 \text{ mm}$.

In this case the the large displacement solution option was not fitting the results properly, since the analysis stopped before the instability point was reached, as shown in Figure 38. For this reason the option KSPIN has been used to consider the reduction of stiffness due to the spin softening but keeping the small displacement activated. A closer analysis at the KSPIN option^[21] shows, in truth, that this is following exactly the same approach Brunelle

used in the analytic formulation, while the LD option, which is indeed more accurate, reaches instability earlier. Moreover, it can be proven that in case of the one-dimensional beam, the Large Displacement is actually degenerating in the KSPIN, giving the same results obtained by Brunelle.^[2]

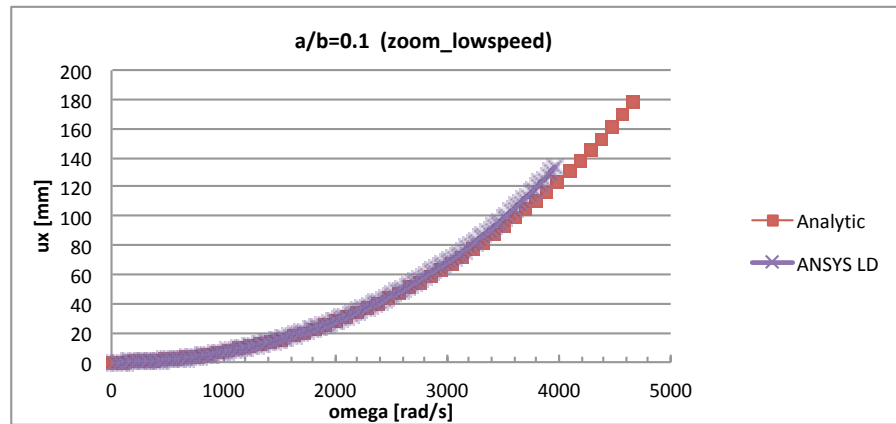


Figure 38: Comparison between Ansys results and analytic model: LD option

Using the KSPIN setting the matching between analytic formulation and numerical model results to be very neat and to obtain comparable values of burst speed (Figure 39).

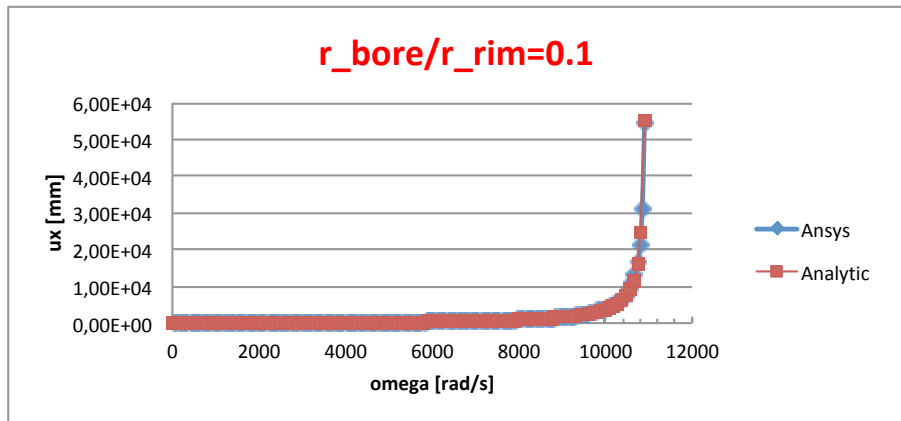


Figure 39: Comparison between Ansys results and analytic model: KSPIN option

Eventually, the table gathers some numerical values calculated for different geometry ratios, a/b , which, if all the other parameters are constant, govern the burst speed no matter of the absolute dimensions.

TABLE IV: INSTABILITY BURST SPEED OF A ROTATING DISK: COMPARISON BETWEEN ANALYTIC AND NUMERIC RESULTS

a/b	Ω_{crit}	$\omega_{burst_analytic}$	ω_{burst_Ansys}
0.1	2.088	10997	10980
0.3	2.404	12666	12630
0.5	3.183	16763	16750
0.7	5.193	27366	27300
0.9	15.604	82207	82025

CHAPTER 6

COMPARISON BETWEEN TWO-DIMENSIONAL AND THREE-DIMENSIONAL MODELS

The study shown in the previous chapter, which was explaining the instability condition of a rotating disk modeled as a bi-dimensional axisymmetric structure, compared the results obtained by using the finite element simulations with the analytic formulation and is fundamental in order to validate the effectiveness of a bi-dimensional numerical model implemented using the software Ansys.

The two-dimensional model works perfectly in case of axisymmetric disks, since Ansys allows to set up a plane problem using the option of axisymmetry, but if some asymmetries, like for instance a certain number of holes in the web area, are present, the finite element analysis requires several complications, so the study of a tri-dimensional model becomes necessary.

Thus, the aim of this chapter is to show that a simple three-dimensional model of an axisymmetric disk with no holes, built using the *Cyclic Symmetry* command, is consistent with the two-dimensional one, that is instead using the axisymmetry option of the *Plane42* element in Ansys.

The analysis has been carried out studying the problem firstly using the *Small Displacement* option, then by setting the *Large Displacement* and testing the behavior of the structure using some idealized bi-linear material curves.

Those fictional bi-linear material curves allows easily to vary the plastic part of the material curve, keeping constant all the other parameters: in particular, the elastic line and the ultimate stress considered are conserved, while the strain at the UTS is the only varying parameter.

It is important, however, to point out that the all the bi-linear curves used in this particular analysis are not real, but have been arbitrary sketched with the only purpose of stressing out the reaction of the numerical model when larger strains are allowed.

6.1 Two-dimensional model

The two-dimensional model is considering a planar case using the element *Plane42* (Figure 40) that is defined by four nodes having two degrees of freedom each (translations in the nodal x and y directions), setting the option for the axisymmetry of the problem. The mesh has been created by manually defining the size of the areas of each element and using the free mesh option.

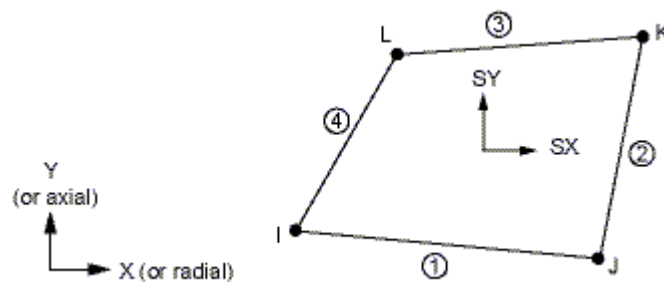


Figure 40: *Plane42* element

In Figure 41 it is possible to see the meshed 2D model with the boundary condition: the displacement of a node at the inner radius have been set to zero, so that the displacement in the axial direction (y-axis) is constantly equal to zero.

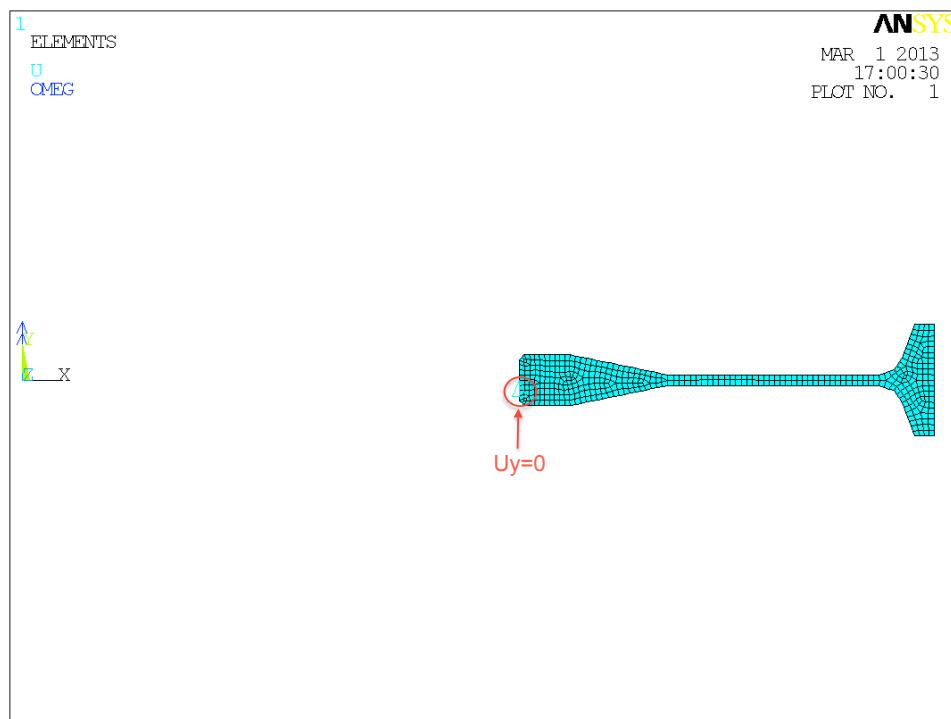


Figure 41: Bidimensional model

6.2 Three-dimensional model

For what concerns the three-dimensional model, the geometry model has been created using the *cyclic symmetry* on a sector of 10° in order to reduce the total number of nodes involved

in the calculation. The definition a high level and a low level surface, which are linked using particular constraint relations, allows the cyclic option to consider the repetition of the basic sector and to build the solution on the expanded geometry.

In Figure 42 it is possible to see the basic sector that is going to be considered for the analysis, obtained by extruding the cross-sectional area that is used for the 2D model about the y-axis.

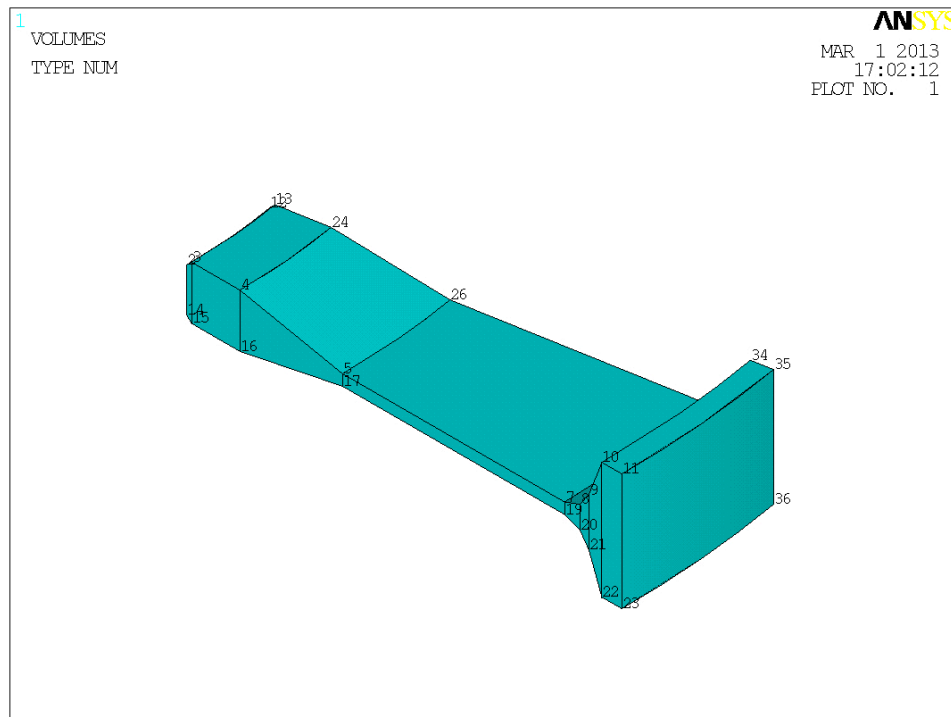


Figure 42: Basic Sector

The three-dimensional mesh of the basic sector has been performed defining two elements: a quadrilateral plane element, *Mesh200*, with 8 nodes; and a 20-noded brick element, *Solid95*. The quadrilateral *Mesh200* is used on the high level boundary surface of the cyclic sector, setting the divisions to use for each segment and defining a mapped mesh of the areas. The *Solid95* element is used, instead, by sweeping the volumes. Ansys is automatically recognizing the second surface as linked to the high level edge and doubling the areal mesh.

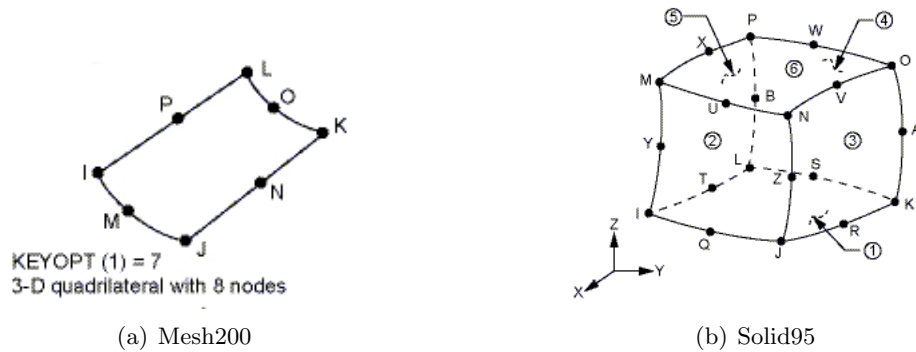


Figure 43: Elements used in the three-dimensional case

The mesh of the high edge component is shown in Figure 44(a), while the full sweep is shown in Figure 44(c).

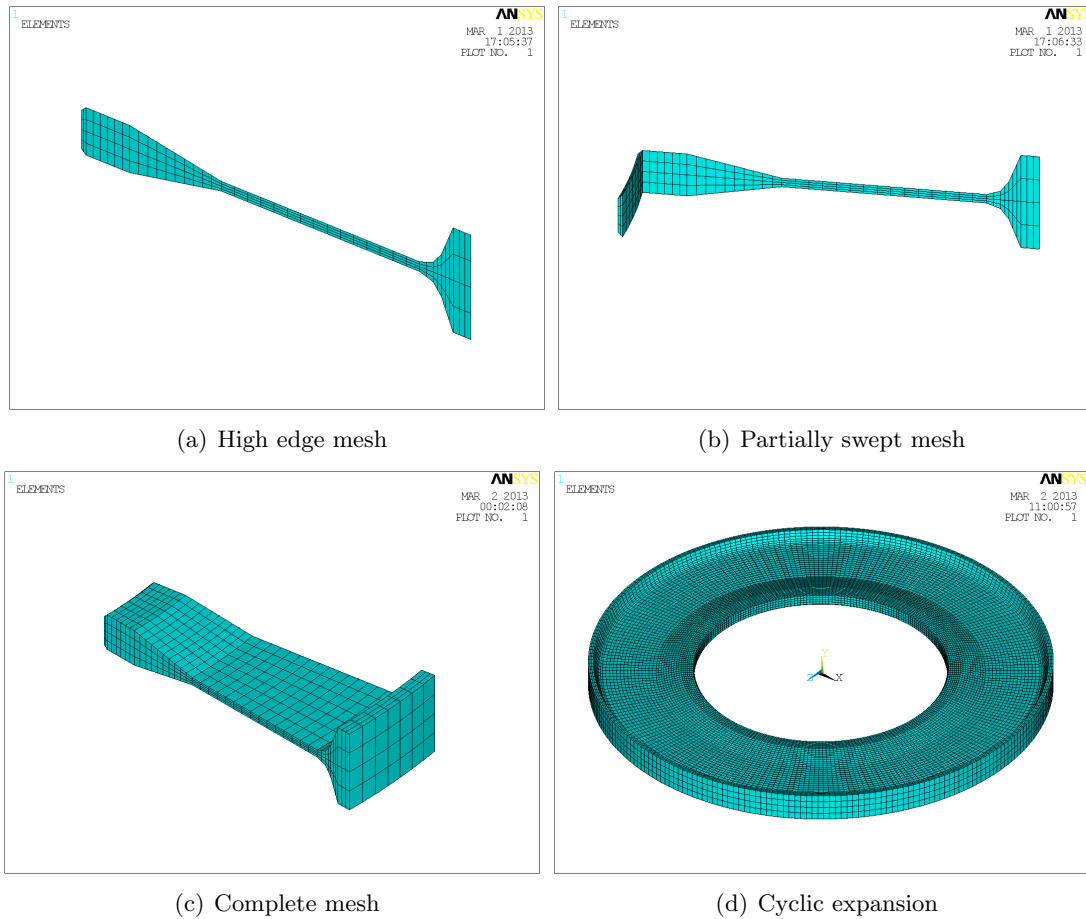


Figure 44: Three-dimensional model mesh

As for the two-dimensional model, it is fundamental to set a boundary condition that prevents the rigid body motion of the disk in the axial direction. For this reason, the displacement on one line belonging to the bore surface has been fixed to zero in the y direction ($U_Y = 0$).

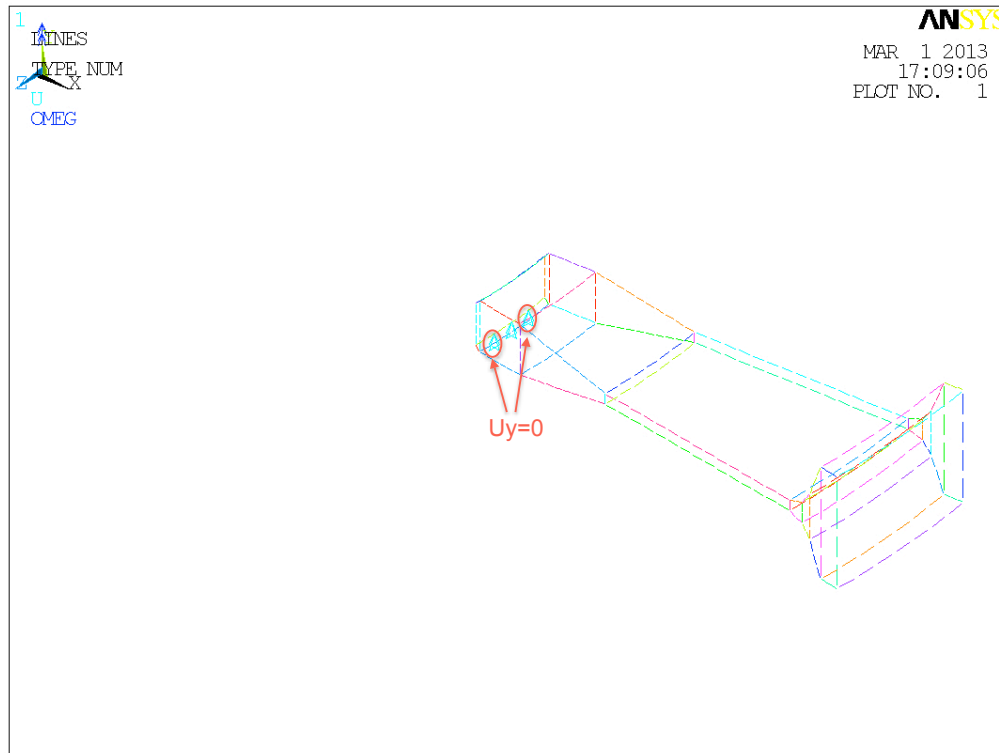


Figure 45: Three-dimensional: lines and boundary condition

6.3 Finite element analysis of the burst limit

The Finite Element analysis is run for both the two-dimensional and three-dimensional model in order to verify that they provide the same burst speed with comparable results.

The material properties implemented are varied using some fictional curves that on purpose let the strain at the fracture point to change in an exaggerated and arbitrary way, while the Young's modulus (elastic behavior of material) and the yield point are kept constant. In this way it is possible to investigate the variation of the burst speed as the plastic behavior is more

or less extended.

The two options for *Small Displacement* and *Large Displacement* are used to compare the results obtained whether the software is considering the non linear effect of plasticity or not. From the discussion made in Chapter 4 it is expected, then, that the burst speed is not varying if the SD option is enabled, while if the LD option is used it should be verified a decrease of burst limit as the plastic strain at the UTS is increasing.

6.3.1 Small displacement simulations

For the small displacement analysis the following material properties have been used:

- Young's modulus: $E = 206700 \text{ MPa}$;
- Poisson's ratio: $\nu = 0.3$;
- Density: $\rho = 8.219 \cdot 10^{-9} \text{ ton/mm}^3$;
- Two fictional bi-linear curves in the $\sigma - \varepsilon$ plane, with constant yield point at $\varepsilon = 0.004299$ and $\sigma = 888.6033 \text{ MPa}$ and variable ε_{UTS} at $\sigma = 1275 \text{ MPa}$ (Figure 46).

Only two curves are used in this analysis to show that the results obtained with the *Small Displacement* option are not varying if the material curve is changing its shape only in the post-yield area. So, the two curves shown in Figure 46 are considering the increase of the strain at the *Ultimate Tensile Strength* that goes from $\varepsilon_{UTS} = 0.1$ to $\varepsilon_{UTS} = 0.3$.

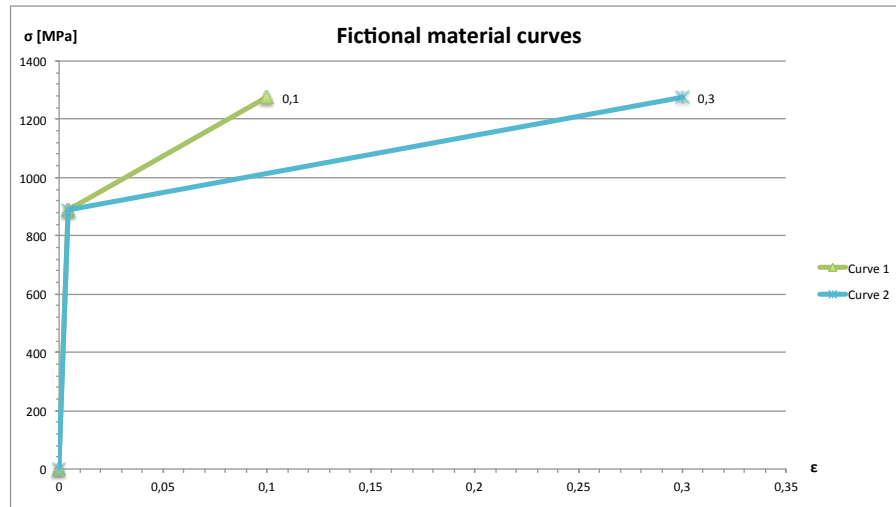


Figure 46: Bi-linear material curves used in the SD analysis

The angular velocity has been set as $\omega = 1500 \text{ rad/s}$, and the analysis is considering 100 equally spaced substeps using the *line search* option (Newton-Raphson criteria). The condition of inertial instability is verified whenever the software fails to find the convergence value for the solution, so that specific substep is directly referring to the burst speed.

As expected the burst speed using the *Small Displacement* is not varying if the material curve is arbitrary changing its tendency in the plastic field, as in this case the increase of the strain value at the fracture point. In Table V it is possible to read the results obtained using both the 2D model and the 3D model for the two material curves discussed before.

From the results shown in the table it is also evident that the two-dimensional and the three-dimensional model give back the same results, at least in terms of bursting speed. In

TABLE V: SMALL DISPLACEMENT ANALYSIS: BURST SPEED

ε_{UTS}	ω_{burst_2D} [rad/s]	ω_{burst_3D} [rad/s]
$\varepsilon_{UTS} = 0.1$	1290	1290
$\varepsilon_{UTS} = 0.3$	1290	1290

addition it is also possible to show the equivalency of the two models by looking at the plots of principal and equivalent stresses. Principal stresses of the 2D and the 3D models, σ_c and σ_r (respectively the first and the second principal), are perfectly matching with a relative error less than 2% (Figure 47).

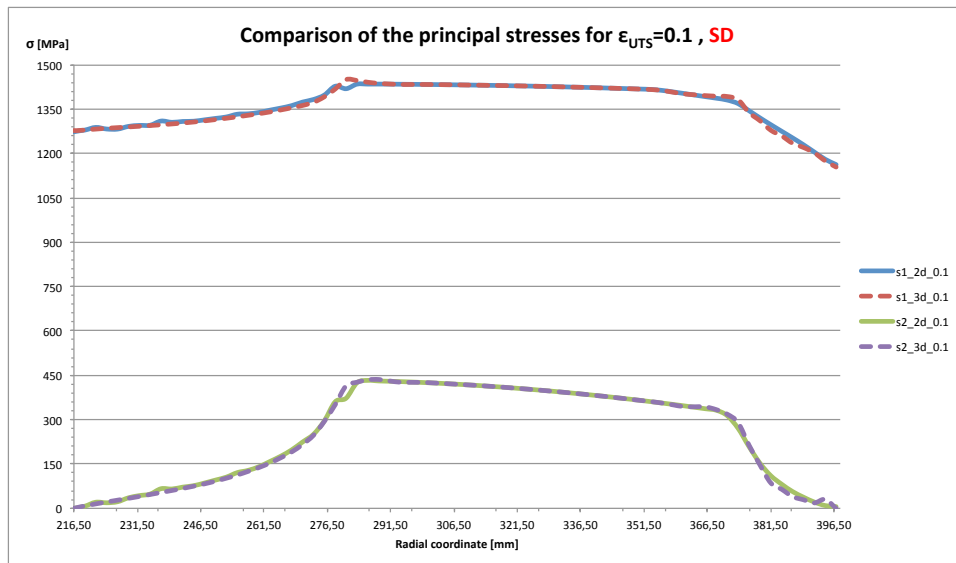


Figure 47: Comparison of principal stresses tendencies before burst (SD)

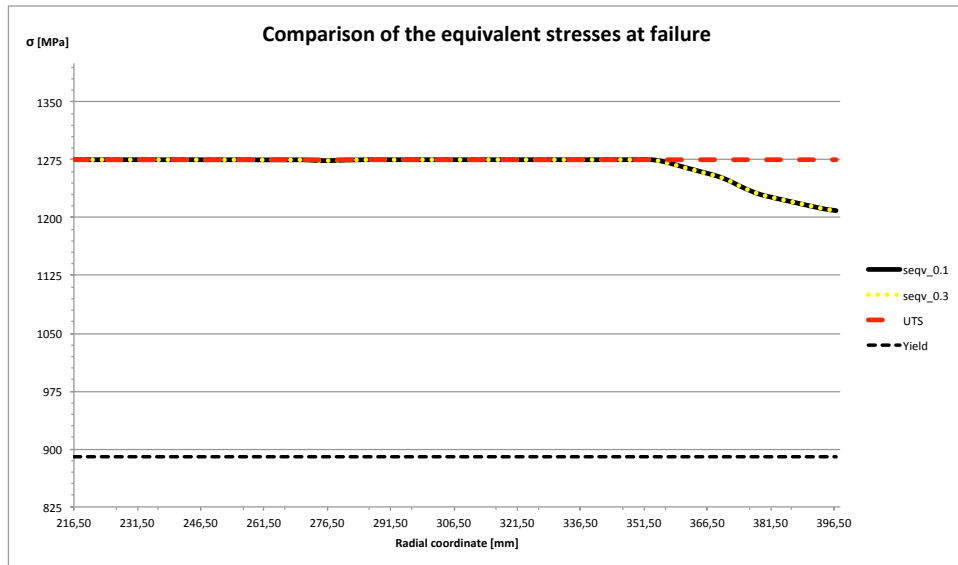


Figure 48: Comparison of equivalent stresses tendencies before burst (SD)

Figure 48 shows clearly that change in the plastic part of the material bi-linear curve is not effecting at all the *Small Displacement* results, since for both curves (Curve 1 and Curve 2 in Figure 46) the burst speed is $\omega_{burst_SD} = 1290 \text{ rad/s}$ and the tendency of the equivalent stress along the radius is not changing.

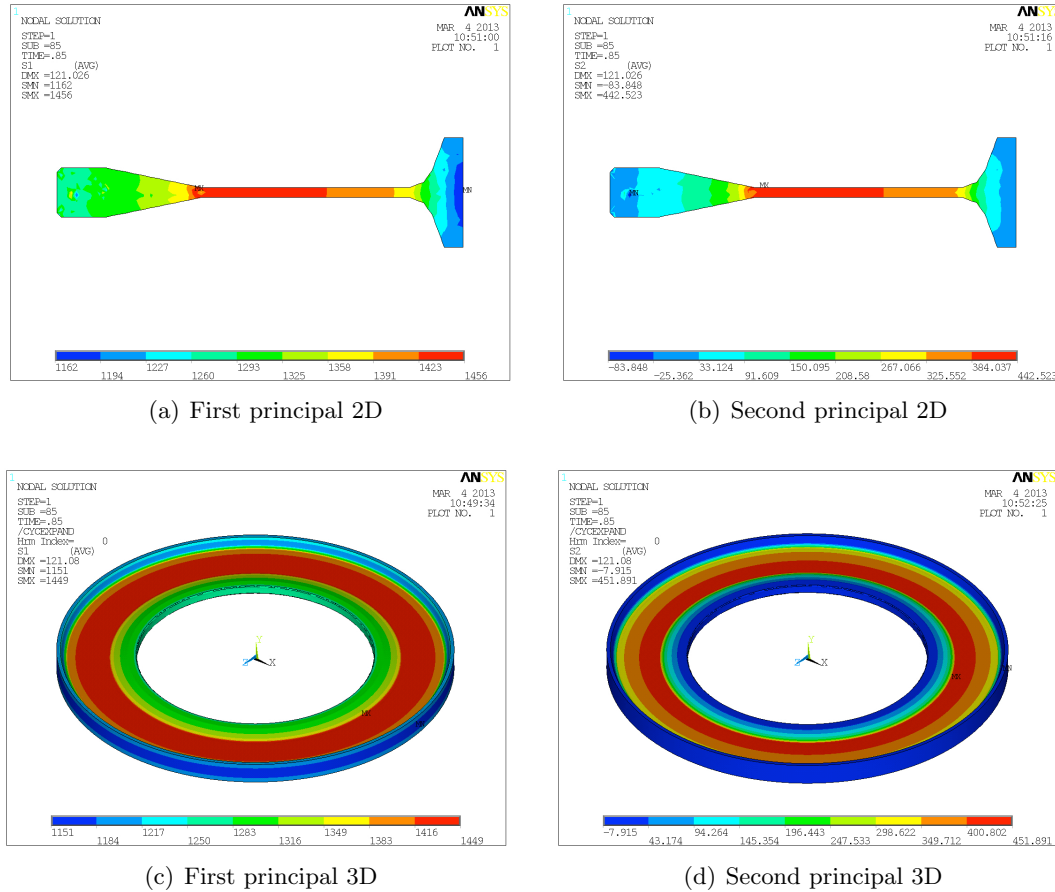


Figure 49: Contour plots of the principal stresses, SD analysis

It might be useful, finally, to look at the evolution of the equivalent stress during the loading phase, as shown in Figure 50. It is interesting to notice that near the yielding load, approximately 890 MPa , the σ_{eq} curve flattens since the region closer to the bore (the most stressed one) is plasticizing and has lower stiffness, while the external part of the disk (that is less stressed) is still working in the elastic field, thus the higher stiffness of this part contains

the deformations of the disk preventing the total plasticization of the disk and keeping constant the stress until load (speed) increases.

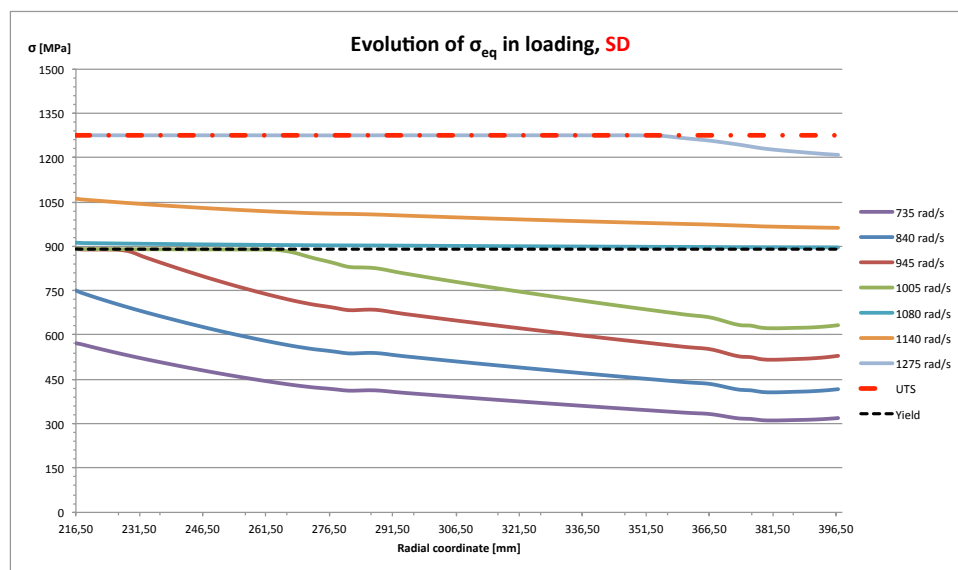


Figure 50: Loading evolution of the σ_{eq}

In conclusion, when using the *Small Displacement* option, burst is a condition dominated only by the elastic part of the material curve, while no differences are noticed if variations are introduced in the plastic region.

6.3.2 Large displacement analysis

By enabling the *Large Displacement* option it is possible to study the correlation between the burst speed and the material curve as the plastic behavior is changed. For this analysis the material models used are the same used for the *Small Displacement* analysis, but this time more curves are going to be considered:

- Young's modulus: $E = 206700 \text{ MPa}$;
- Poisson's ratio: $\nu = 0.3$;
- Density: $\rho = 8.219 \cdot 10^{-9} \text{ ton/mm}^3$;
- Five fictional bi-linear curves in the $\sigma - \varepsilon$ plane, with constant yield point at $\varepsilon = 0.004299$ and $\sigma = 888.6033 \text{ MPa}$ and variable ε_{UTS} at $\sigma = 1275 \text{ MPa}$ (Figure 51).

Again, the angular velocity set in the loading option is $\omega = 1500 \text{ rad/s}$, and the simulation uses 100 equally spaced substeps (*Automatic time stepping off*), solving the non-linearity through the line search option.

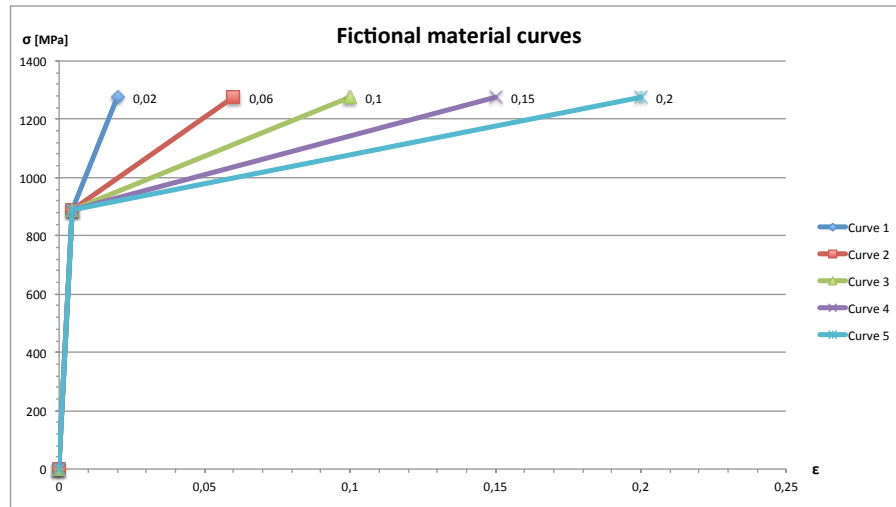


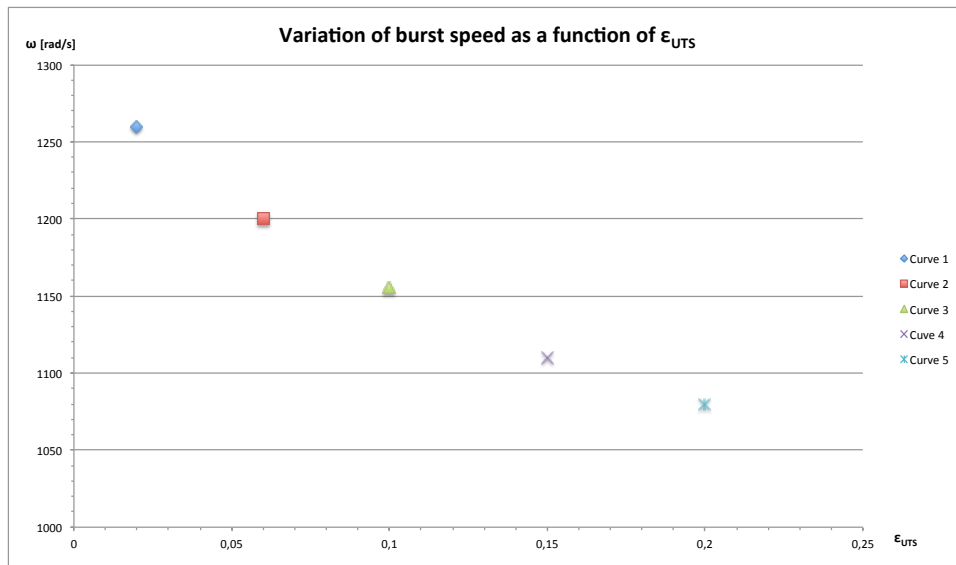
Figure 51: Bi-linear material curves used in the LD analysis

While for the SD analysis the burst speed was always the same and equal to $\omega_{burst_SD} = 1290 \text{ rad/s}$, using the LD option the burst speed is influenced by the material curve used and it is as much lower as the plastic strain at fracture (ϵ_{UTS}) is higher.

In Table VI the burst speed for each case considered is shown, while in Figure 52 it is possible to look at the trend of in the $\omega - \epsilon$ plane.

TABLE VI: VARIATION OF BURST SPEED

Curve	ε_{UTS}	ω_{burst} [rad/s]
1	0.02	1250
2	0.06	1200
3	0.10	1155
4	0.15	1110
5	0.20	1080

Figure 52: Burst speed trend as function of ε_{UTS}

In order to evaluate the equivalence of the 3D and 2D models, the plots of principal and equivalent stresses for one of the material curves are compared, as done in Figure 53 and Figure 54 for the Curve 3. The equivalence is easy to read from graphs, since the relative error of the principal stresses plot is always below 1.5 %, while the equivalent stresses in both the 2D and the 3D models follow exactly the same path along the radial coordinate.

Generalizing this result it is possible to state that a three-dimensional model like the one showed in this chapter is perfectly equivalent to the two-dimensional model that was used in the analysis of Chapter 4 to prove the consistency of the results obtained by Ansys for inertial instability.

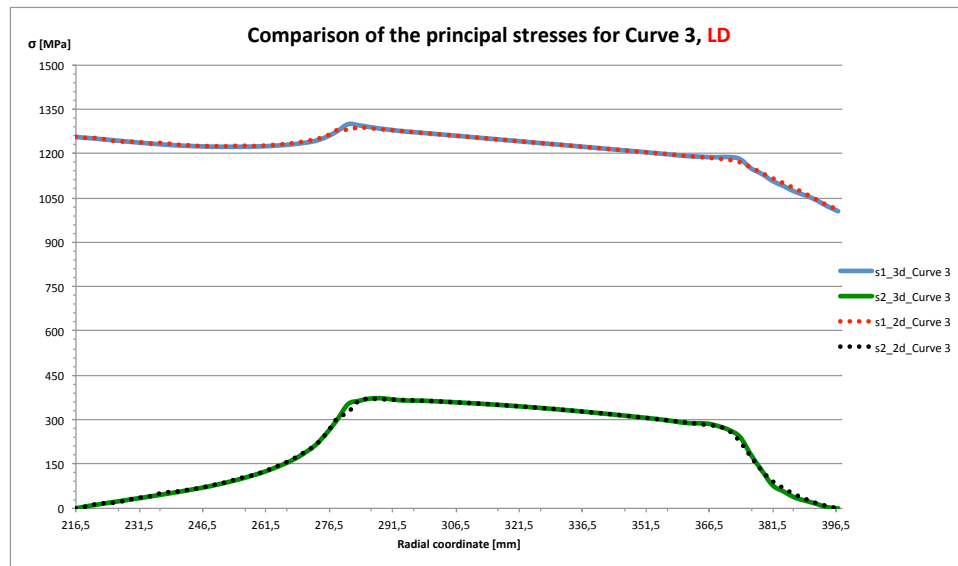


Figure 53: Comparison of principal stresses tendencies before burst (LD)

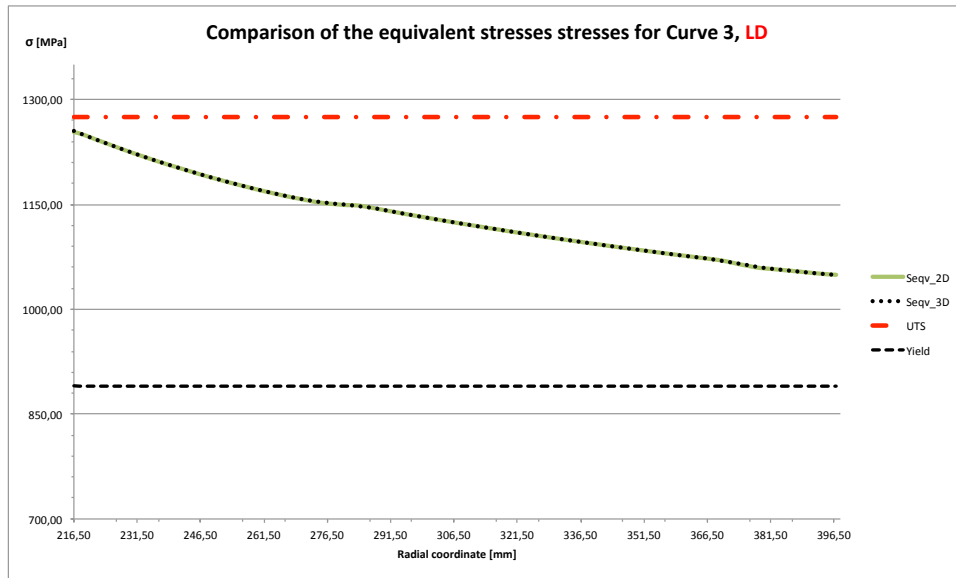
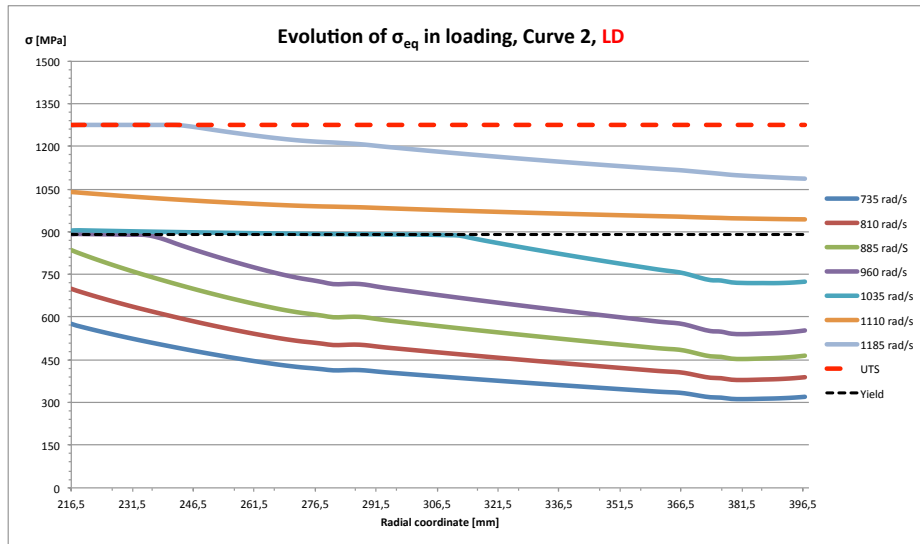


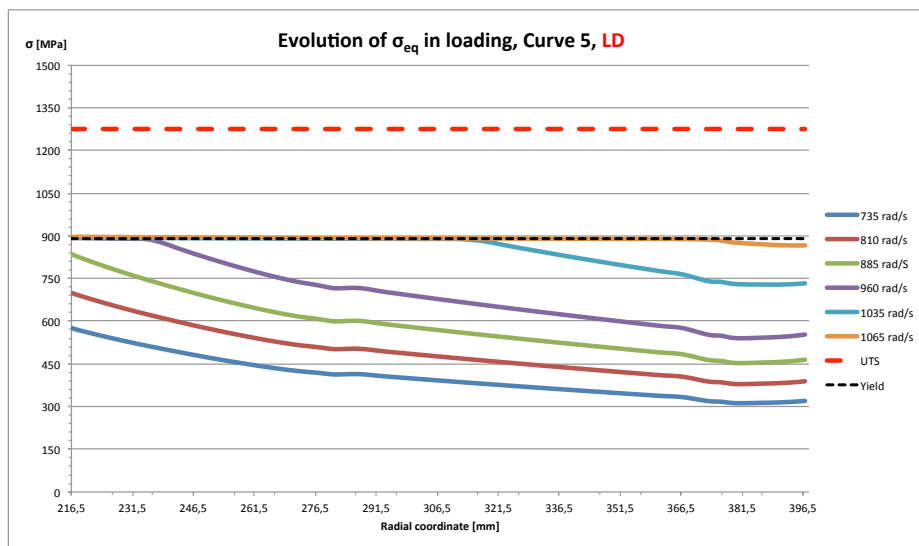
Figure 54: Comparison of equivalent stresses tendencies before burst (LD)

It might be also interesting to compare the loading history when different curves are considered, in order to look at the different values of σ_{eq} corresponding to each loading condition in terms of angular velocity.

Curve 2 ($\varepsilon_{UTS} = 0.06$) and curve 5 ($\varepsilon_{UTS} = 0.15$) have been considered in order to show the great influence that the variation of the plastic segment of the fictional bi-linear curves has in terms of stresses induced into the disk.



(a) Curve 2



(b) Curve 5

Figure 55: Comparison of the equivalent stresses in loading for curve 2 and curve 5 (LD)

Looking at Figure 55, the first difference that is possible to notice is that the equivalent stress is never exceeding the yielding point when the curve 5 for the material is set, while if curve 2 is considered, the disk plasticize for high loads (near burst speed), thus the equivalent stress reaches higher values and, eventually, for the last substep before failure the internal part of the disk is actually suffering the σ_{UTS} .

This shows perfectly the relationship that exists between burst and the plastic part of the material curve, highlighting the biggest drawback of the Robinson formula showed in Chapter 3 that is not considering at all the influence of plastic behavior for the determination of burst speed.

Inertial instability, instead, perfectly matches with the burst limit modification due to large deformations: as it is possible to see in Figure 56, in fact, the displacements at the rim of the disk show a asymptotic behavior at the burst speed, with a sharp increase of displacement that brings to failure.

Moreover, a first intuition can derive from the implementation of this “fake curves”: the most the curve is flattened (highest strain at fracture) the lowest are the stresses that the rotating disk can suffer and consequently the burst speed.

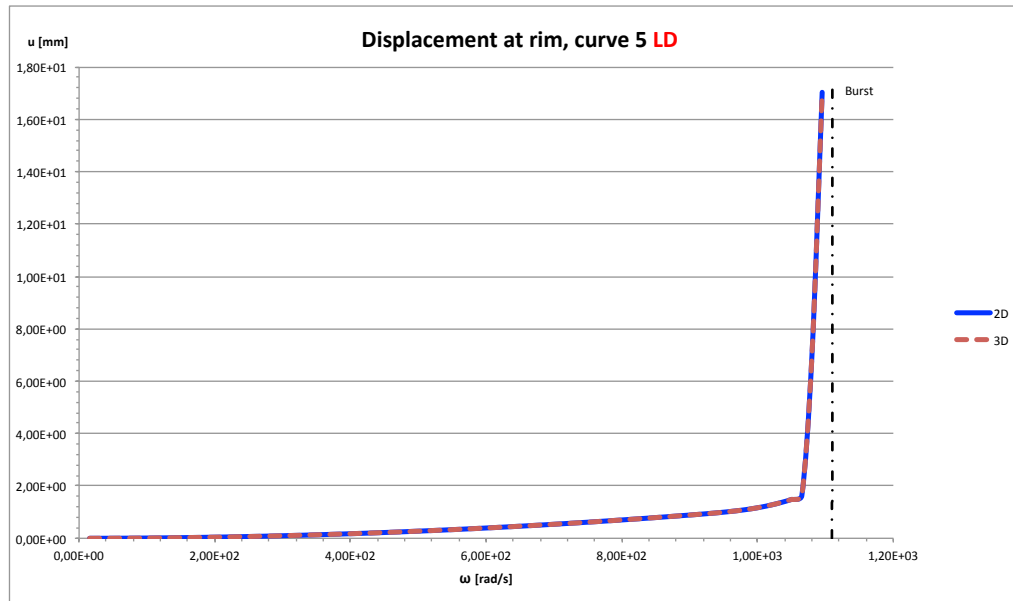


Figure 56: Displacements at rim for curve 5

After proving that the two models, both the two-dimensional and the three-dimensional one, give the same results and that the *Large Displacement* analysis is largely influenced by the variation of the material curve in the plastic region, it might be useful to look up for some more realistic results using experimental material curves obtained by testing the “INCONEL[®] 718”. Since the experimental tests have, of course, a normal distribution of occurrences, each material characterization is represented by a set of curves that are contained between a minimum curve and a maximum curve.

In Figure 57 is reported the dimensionless $\sigma - \varepsilon$ plot of one of this curve with the minimum, the maximum and the mean tendencies and it is also sketched a box of allowable statistical variations of σ_{UTS} and ε_{UTS} .

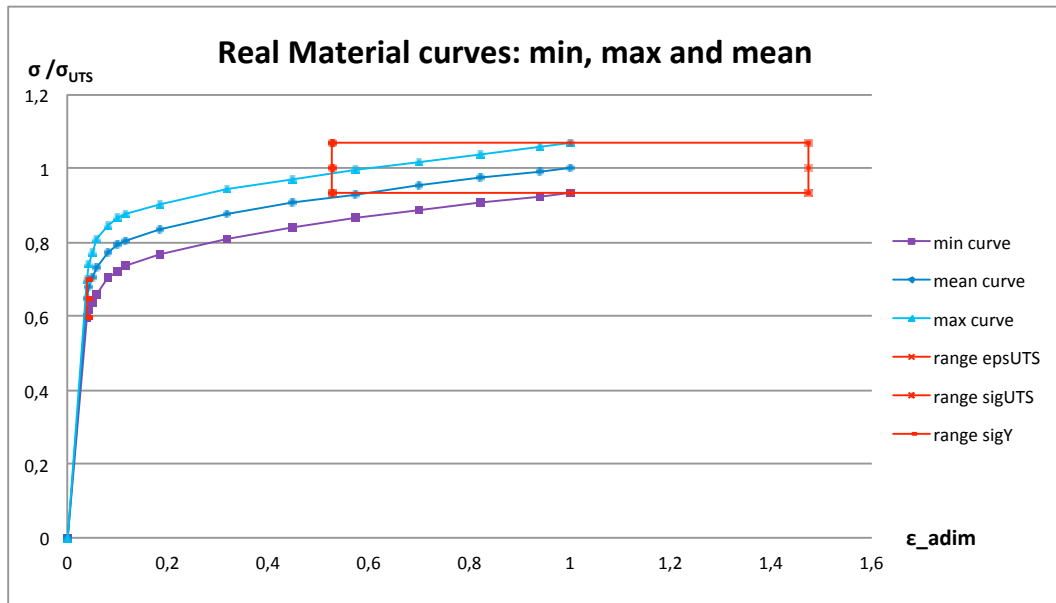


Figure 57: Experimental material curve with variation ranges

In second analysis is possible, starting from the mean curve of Figure 57, to consider the worst combination of stress and strain at the UTS, sketching the curve that presents the greatest reduction in stiffness in the plastic region preserving the same value at yield: lowest σ_{UTS} and largest ϵ_{UTS} (Curve 1A in Figure 58).

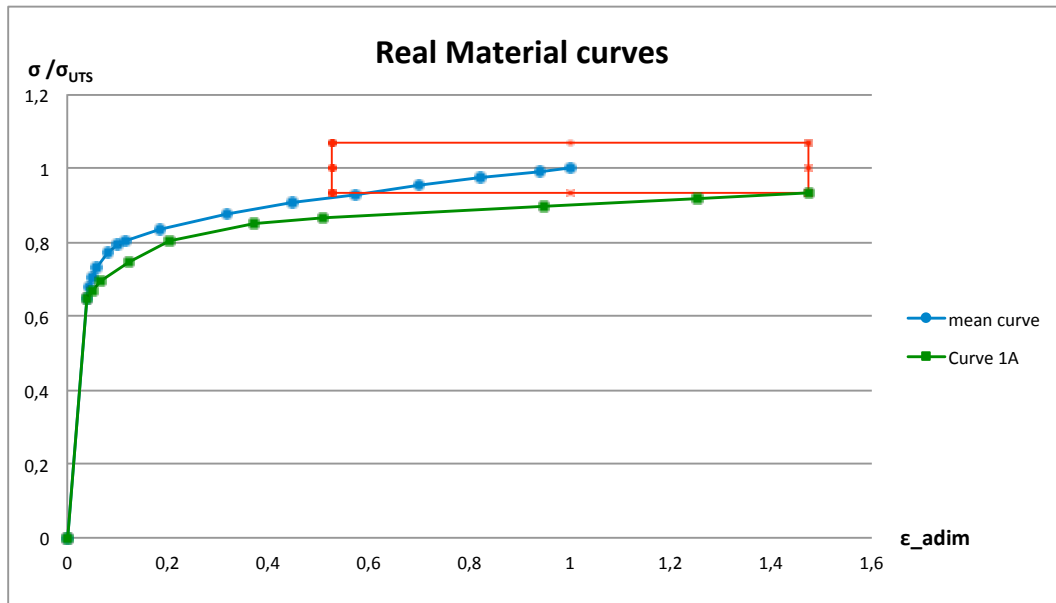


Figure 58: Mean curve and modified curve

The results obtained by using the Finite Element analysis with the option for *Large Displacement* allows to complete the following table that shows the results obtained by using the numerical code for both the cases of the mean real curve and the modified one.

TABLE VII: COMPARISON BETWEEN MEAN REAL CURVE AND WORST OCCURRENCE

Curve	ω_{burst_Ansys} [rad/s]
Mean Curve	1320
Curve 1A	1290

The plot in Figure 59 shows the the displacement at the rim as function of the angular velocity: this plot is very meaningful since it allows to loot at the relationship between burst speed and displacement, explaining in this way the instability condition due to the sharp increase of deformation.

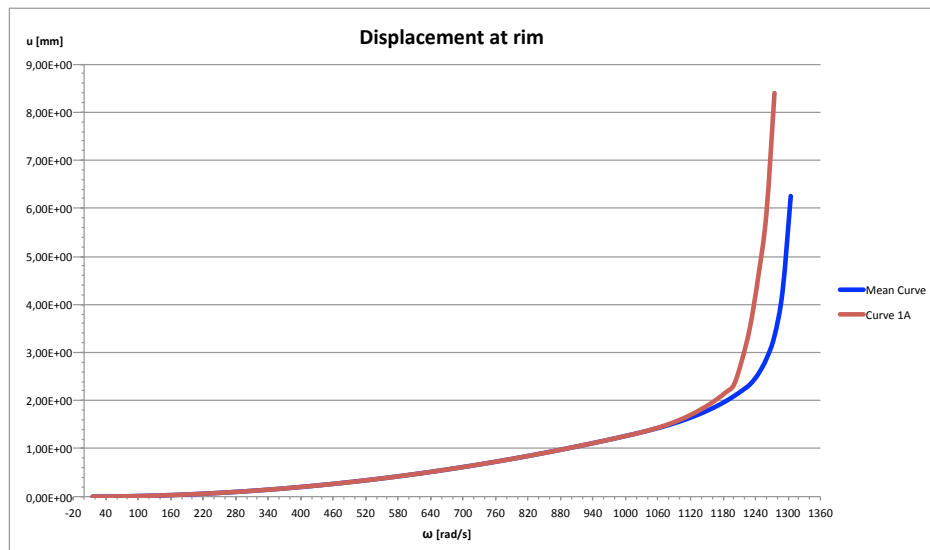


Figure 59: Displacement at the rim for real material curves

6.4 Comparison with Robinson's criterion

Finally, it is possible to compare the burst speed estimated by the numerical code Ansys over the three-dimensional model with the results obtained by simply applying the Robinson criterion cited in Section 3.8.

In order to apply the simple proportion formulated by Robinson in 1944^[18], it is fundamental to know two governing parameters: the engineering tensile strength, σ_{UTS_eng} , and the mean hoop stress, σ_{c_m} .

The engineering tensile strength is obtained from the known true values, by simply applying the following two formulas:

$$\varepsilon_{true} = \ln(1 + \varepsilon_{eng})$$

$$\sigma_{true} = \sigma_{eng}(1 + \varepsilon_{eng})$$

For what concerns the average hoop stress, two equivalent methods can be used in our case.

The first way to obtain the average hoop stress is to use the numerical code and ask the software for the centroid hoop stress for each element at a certain angular velocity and, subsequently, average this value, obtaining the average hoop stress over the two-dimensional model. Important is to pick a sufficiently low rotational speed so that the *Large Displacement* analysis

in Ansys gives the same results that it would be obtained in a *Small Displacement* simulation. Robinson, in fact, is not considering at all the plastic behavior of materials and the effects of deformations (variations of r_G and A influence the final result), so the angular velocity to use for the proportion has to be such that the resultant stress is in the elastic field.

A second possible solution to find the mean hoop stress is to solve a simple equilibrium problem on a half-disk, since in this particular situation only centrifugal loads are acting on the disk. So, the forces acting on the disk are $2 \cdot A \cdot \sigma_{c,m}$ and $F_c = M \cdot \omega^2 \cdot r_G$ acting on the center of gravity G (Figure 60).

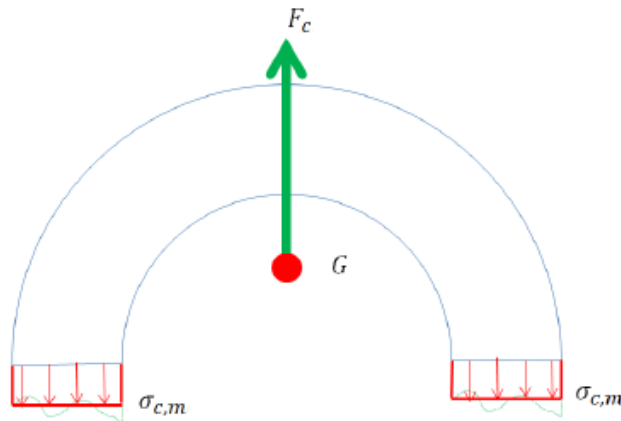


Figure 60: Equilibrium on a half-disk

By simply substituting the formula for the center of gravity of an annular disk and the value of the area it is possible to obtain the following expression for the mean hoop stress as a function of the angular velocity ω :

$$\sigma_{c.m} = \frac{2/3 \omega^2 \rho (R_{rim}^3 - R_{bore}^3)}{2 (R_{rim} - R_{bore})} \quad (6.1)$$

The proportion in Equation 3.39, $\omega_{burst} = \omega \sqrt{\frac{\sigma_{UTS}}{\sigma_{c,mean}}}$, then, gives back the burst speed value.

For the *bi-linear material curves*, all having the same value of σ_{UTS} the Robinson criterion gives the same result: once that the engineering ultimate strength is fixed, the burst speed is not influenced at all by the plastic part of the material curve, since the only conditioning material parameter is σ_{UTS} .

Hence, for all this cases we have :

$$\omega_{burst_Robinson} = 1258 \text{ rad/s}$$

In Figure 61 the displacements at the rim for all the different curves are reported together with the value of burst speed calculated using the Robinson criterion. It appears from the picture that the Robinson's value of burst speed is more conservative than the values obtained implementing an elsto-plastic analysis in ansys using the *Large Displacement* option. Moreover, this value is much more conservative as the stiffness of the second segment is reducing compared

to the stiffness of the elastic part. This perfectly shows one of the limit of the semi empiric analytic formula developed by Robinson: it doesn't consider at all the plastic deformation of materials and it only depends on the value of UTS. However, Robinson can still be applied as a rule of thumb: its easiness, in fact, compensate the overestimation of burst speed, and even though the failure for inertial instability is totally different from the one in the Robinson's hypothesis, the results obtained with the elasto-plastic analysis using Ansys are close enough to consider Robinson's result as a starting point for design optimization.

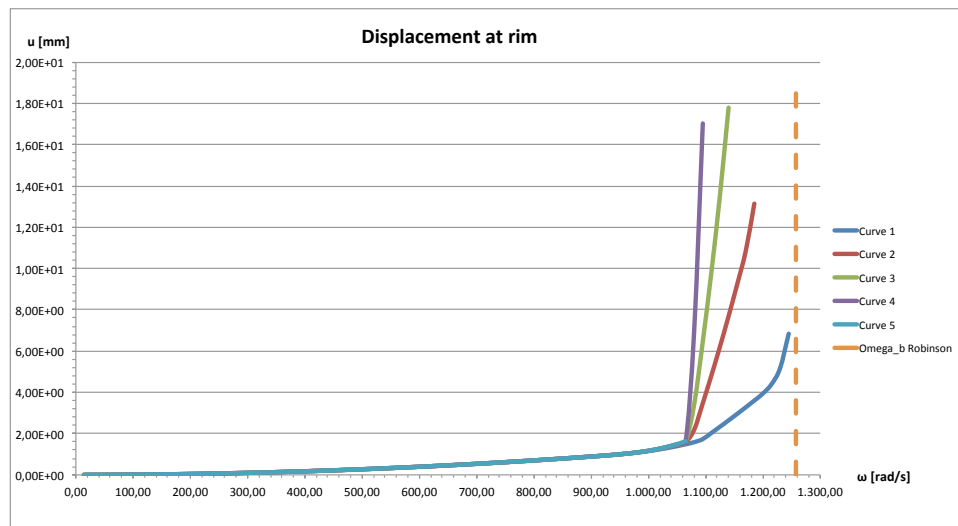


Figure 61: Displacements at rim for the different curves compared with Robinson

The same thing has been done also for the real material curves used in the previous section to perform a *Large Displacement* analysis in Ansys. In this case the curves were entered in the

FEM software as true stress-strain discrete points, so it is important in this case to remember that the analytic formula needs the engineering stress.

The estimated burst speeds for the two cases: mean real curve and modified real curve (Curve 1A) are reported in the table below:

TABLE VIII: BURST SPEED CALCULATED USING ROBINSON FOR REAL CURVES

	<i>Robinson's criteria</i> [rad/s]	<i>Ansys LD</i> [rad/s]
Mean Curve	1338	1320
Curve 1A	1242	1290

From the results in Table VIII, it is very important to notice that changing the material curve from the mean real curve to one created considering the worst statistical occurrences in terms of stress and strain, so with the lowest σ_{UTS} and the largest ε_{UTS} , there is an incoherence when Robinson's criterion is applied.

If the mean curve is taken into account, the value calculated using the analytic criteria is still slightly conservative if compared with the value obtained using Ansys.

On the other side, with the modified curve, the value obtained applying Robinson is smaller than the numerical one, and this makes the Robinson criterion to lose its conservative approach.

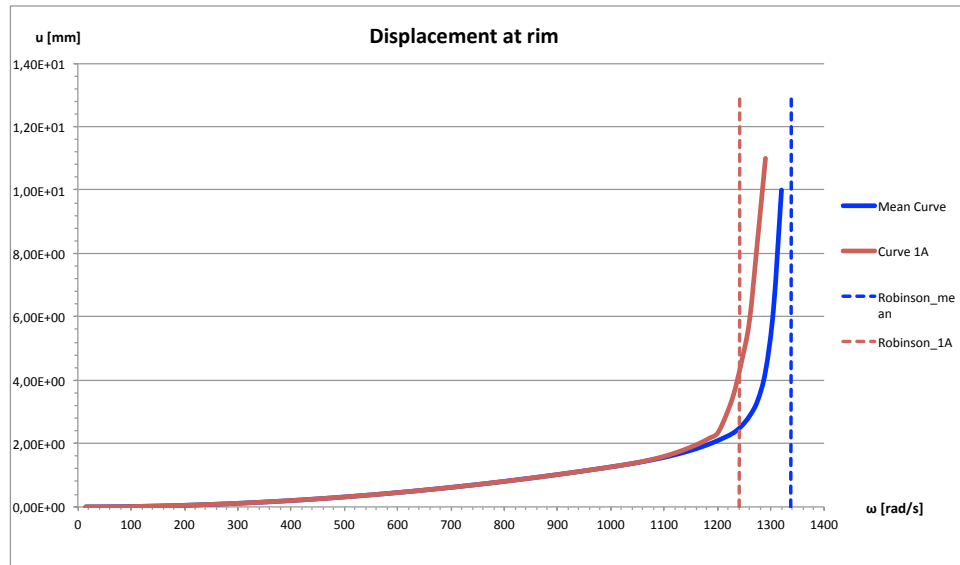


Figure 62: Displacements at rim for real curves compared with Robinson

In conclusion, it is possible to state that in the case of axisymmetric disks the Robinson's criterion provides relatively reliable results with very little efforts that can be used as a rule of thumb for the design of a rotating disk.

However, some limits are pointed out from the comparison of the results obtained applying the formula with the divergence values of the elasto-plastic analyses conducted in Ansys: using the real material curve and considering the worst occurrence of the combination stress-strains allowed in the statistical distribution, Robinson loses its conservative approach and is underestimating the value of burst speed. The indication provided by the this method in case of axisymmetric disks, then, is not to be taken as a true value, but only as an indication of the maximum angular velocity that the structure can withstand.

CHAPTER 7

THREE-DIMENSIONAL MODEL WITH HOLES

Starting from the results obtained by the comparison carried out in the previous chapter, it is possible to state that a three-dimensional model of the disk with cyclic symmetry over a basic sector can be used in a *Large Displacement* finite element simulation in order to predict numerically the burst due to inertial instability. It was verified, in fact, that the results obtained by using this kind of model are perfectly matching the ones obtained using an axisymmetric model, which was proven to satisfy the hypothesis of inertial instability.

Besides, the use of the three-dimensional model allows to study the case of a non-axisymmetric rotating disk, such as, for example, a rotating disk with a variable number of holes in the web area. Holes located in the web area are usually added in order to allow the connection between two or more turbine disks using connecting rods fastened with bolts.

In this chapter, then, the three-dimensional model used previously in the comparison with a two-dimensional one, is modified with the purpose of studying the influence of the number and the dimension of holes onto burst speed.

7.1 Model description

In order to consider the effects due to the presence of a hole on the disk web, it is fundamental to redefine the basic sector by extruding the cross-sectional area by an angle that depends on

the number of holes to consider: $\theta_{basic_sector} = \frac{360^\circ}{no. of holes}$.

The disk used for this analysis is the same simple disk showed in the previous chapters, where the web has constant thickness of $4.5mm$. Since the aim of this chapter is only to show the influence of the number of holes and their dimension onto the burst phenomenon, the position of the holes has been chosen arbitrary in the middle of the web area, not taking into account all the other geometrical constraints that are considered during the design process in order to correctly place the holes.

The extrusion of the basic sector is done by letting Ansys to create 3 equal volume extrusions around the rotation axis, so that it is possible to modify only the central sector that is containing the hole. The hole is created by extruding a solid cylinder in the middle of the web and then subtracting it from the central volume of the previously extruded disk (Figure 63).

As it is possible to see in Figure 63, the volume that contains the hole has been divided into four “slices” that allow to control the mesh around the hole.

The idea is, in fact, to rebuild the mesh of that particular sector using the *LESIZE* command that allows to set the number of elements on a line and the spacing ratio between elements on the same line. In this way, the mesh can be created using mapped 8-noded quadrilateral (*Mesh200*) for the boundary area of the cyclic sector and sweeping the volume with brick elements that have 20 nodes each (*Solid95*).

The mesh obtained is pretty regular and easy to replicate, in Figure 64 the mesh for the entire basic sector is shown, and it is also possible to notice the refinement done in the hole area.

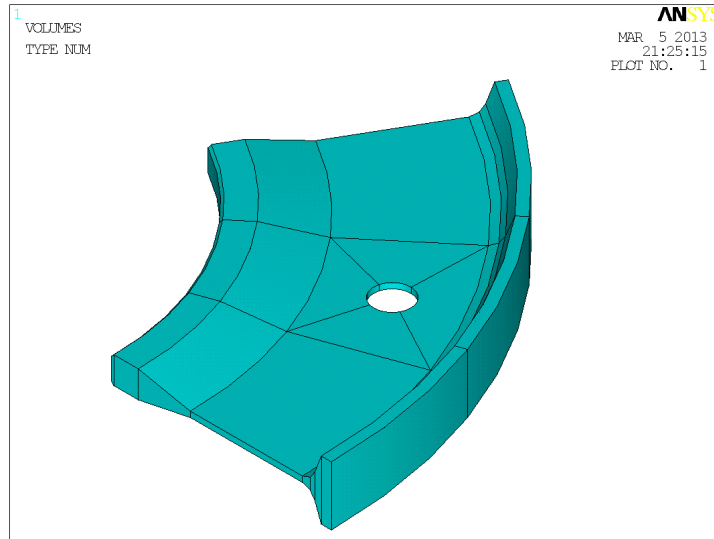
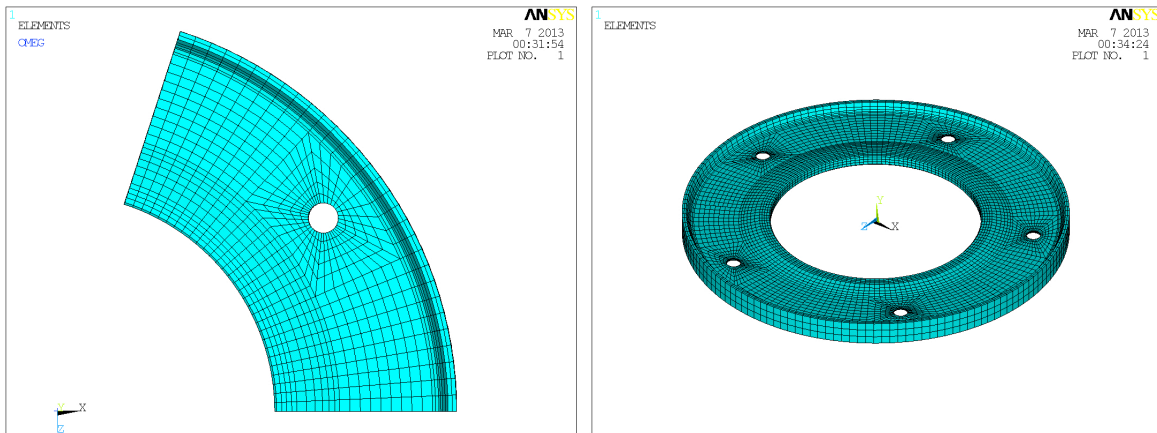


Figure 63: Basic sector with the hole: volume division



(a) Basic sector

(b) Cyclic expansion

Figure 64: Mesh of the holed disk

7.2 Burst speed analyses

The analysis is carried out for an increasing number and increasing dimension of the holes.

As a first analysis, the models considered aim to look at the differences occurring when the number of holes is increased: 5, 8 and 12 holes, keeping constant the dimension of holes at $d = 30mm$, but considering different plastic behavior of material.

Later on in this section, the study is focused on the effects of the size of the hole is conducted on the disks with 5 and 12 holes considering the diameters of 10mm, 20mm, 30mm, 50mm and 60mm, considering this time a real material curve.

7.2.1 Variation of the number of holes

In order to conduce a first study on the variation of burst speed with the number of holes in the web of the turbine disks, two fictional bi-linear material curves from those defined in Chapter 6 have been chosen calling them: **curve 1**, with $\varepsilon_{UTS} = 0.06$; **curve 2**, with $\varepsilon_{UTS} = 0.1$ ¹. In this way it is possible to look at the influence of the presence of holes if the plastic region of the material curve is more or less extended, or in other words for larger or smaller allowed deformations at the ultimate strength.

¹For all the other material properties please refer to the Chapter 6

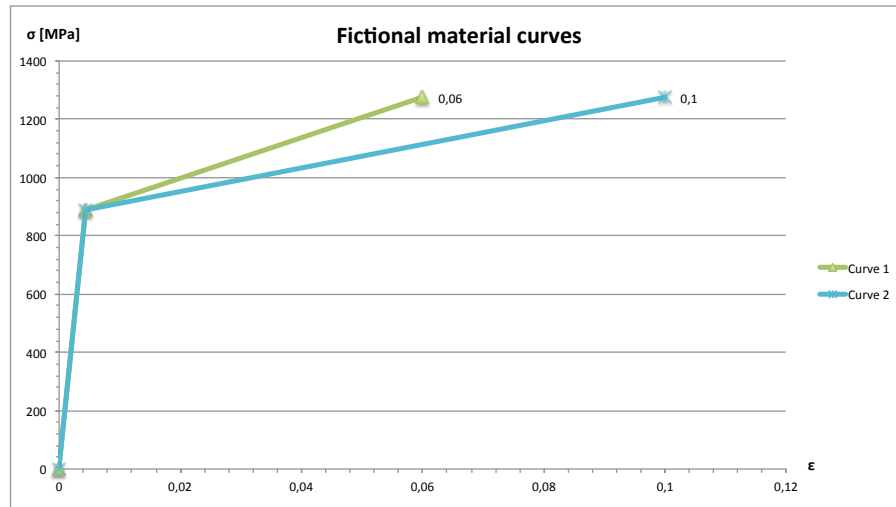


Figure 65: Bi-linear material curves

As for the analysis of the solid disk, the failure of the disk is identified in Ansys by the divergence of the solution at a specific substeps at which the rotational speed corresponds to the burst speed.

Since the values are close to each other, to have more accurate definition of the burst speed the solution option *Automatic time stepping* has been activated, allowing the software to choose the automatically the time step. The parameters used to control the time stepping for this first set of analysis are the following:

- Number of substeps: 3;
- Maximum number of substeps: 300;
- Minimum number of substeps: 1.

This means that the first step increment is $1/3^{rd}$ of the total angular velocity, while the analysis runs until the convergence is reached using the smallest substep increment equal to $1/300^{th}$ of the total angular velocity set in as inertial load to 1500 rad/s .

Considering the **Curve 1** ($\varepsilon_{UTS} = 0.06$) for a disk with 5, 8 or 12 holes, it is possible to observe that a burst speed decreases with the increase of the number of holes (Table IX).

The trend of burst angular velocities is also shown in Figure 66, where the results listed in the table are plotted on the $\omega_{burst} - \text{No. of holes}$ plane. It is possible to see that the simulation gave the same results, within the range of 5 rad/s ($1/300^{th}$ of the total angular velocity set as load), for the burst speeds of the disk with 8 holes and the one with 12 holes, showing an asymptotic trend for higher number of holes.

TABLE IX: VARIATION OF BURST SPEED WITH THE NUMBER OF HOLES - CURVE

1

No. of holes	$\omega_{burst} [\text{rad/s}]$
0	1200
5	1161
8	1152
12	1152

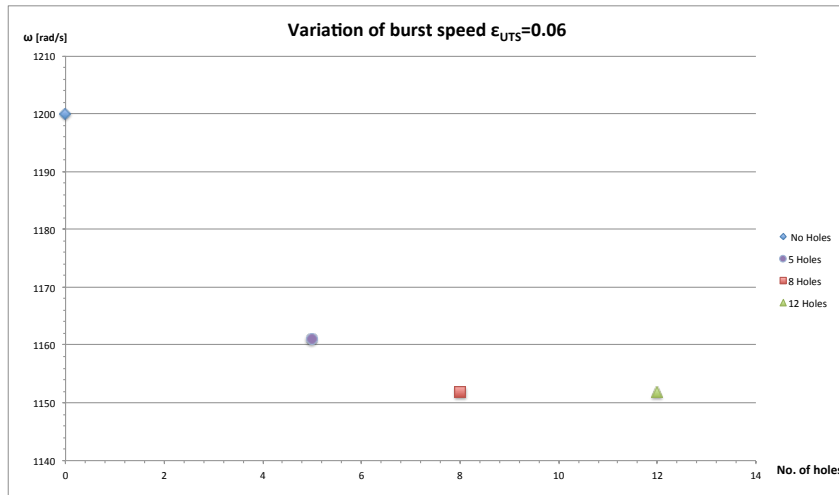


Figure 66: Variation of burst speed with the number of holes (curve 1)

Together with the considerations made about the variation of burst speed with the number of holes, plots of the equivalent stresses at the last substep before failure are here reported so that it is possible to highlight the dynamics of burst. Those plots have been defined along two different paths, both in the radial direction: the first path (*path 1*) is picking the equivalent stress in a section far away from the hole (Figure 67), while the second one (*path 2*) passes through the hole (Figure 70).

From the first path (Figure 67) it is interesting to notice that in a section located far from the holes, the equivalent stress presents a reduction in magnitude in the web area as the number of holes increases and, eventually, there is a minimum for the case with 12 holes, when the pitch between holes is smaller.

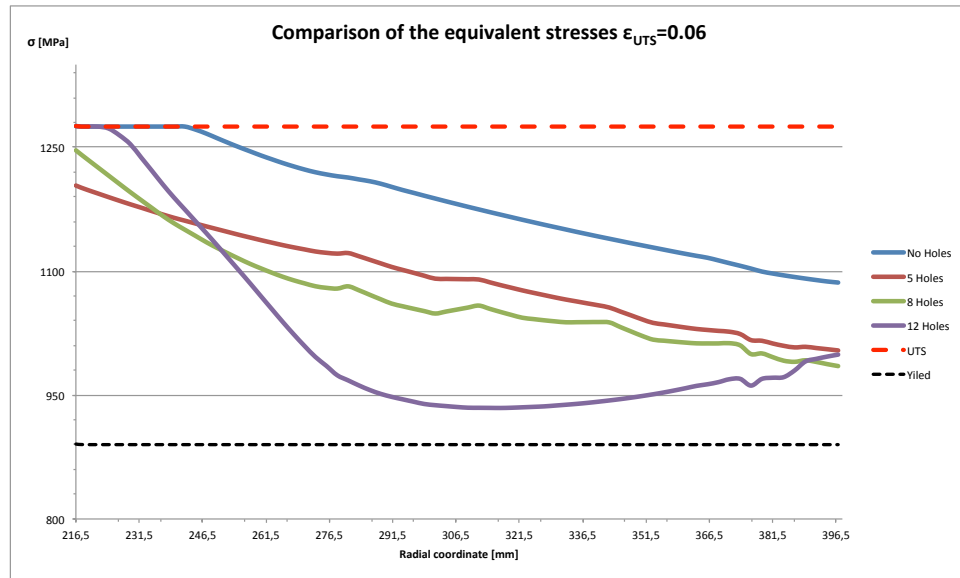


Figure 67: Comparison of equivalent stresses before burst (curve 1, path 1)

Totally different is the equivalent stress tendency along the path that passes through the holes (Figure 68).

The presence of the hole creates a peak of stress along the radial coordinate: plasticization begins at the holes boundaries and, at the last substep before burst, it is possible to see that part of the disk near the hole is at the UTS ($\sigma_{eq} = \sigma_{UTS}$).

This allows to use of the three-dimensional model also to predict the weaker section in case of holed disks: for all the studied configurations, in fact, failure is more likely occurring in the radial direction that passes through the holes, since from the plots the equivalent stress is reaching the ultimate strength.

Failure again occurs for inertial instability, which now can be considered as the predominant

cause of failure when disks are only loaded by the centrifugal load, since some residual stresses could have been undertaken by the portion of the disk not working at UTS.

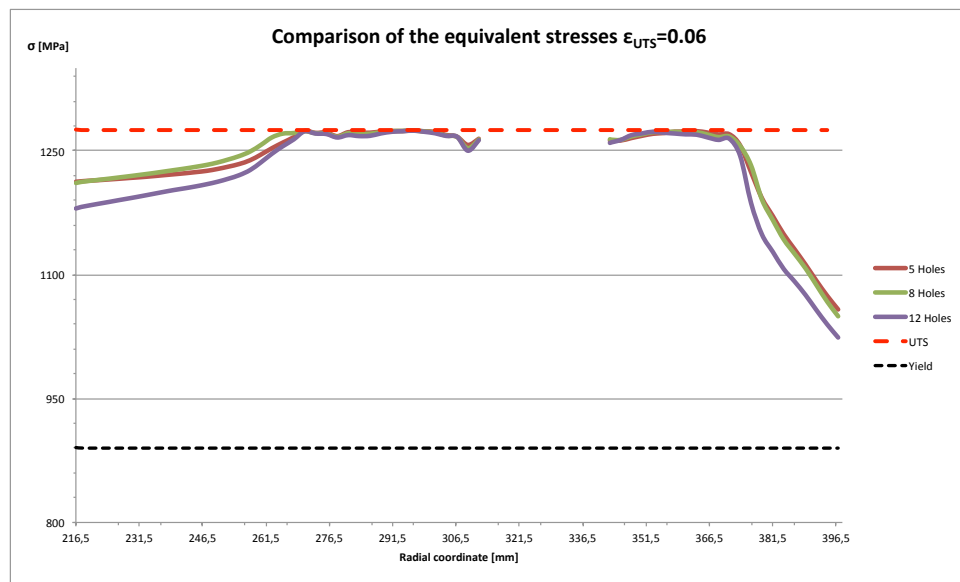


Figure 68: Comparison of equivalent stresses before burst (curve 1, path 2)

The same analysis has been performed for the **Curve 2** ($\epsilon_{UTS} = 0.1$). It shows that the reduction of burst speed for the same number of holes in the web area (Table X) is comparable with the one obtained with the other material curve, but, as expected, burst speeds are lower this time, since the new curve allows larger deformation, hence the inertial instability is induced earlier. Besides, since the plastic part of the material curve is more extended, the differences

between the various cases are more clearly outlined as well as the decrease of burst speed is not reaching any asymptotic behavior (Figure 69).

TABLE X: VARIATION OF BURST SPEED WITH THE NUMBER OF HOLES - CURVE 2

No. of holes	ω_{burst} [rad/s]
0	1155
5	1128
8	1118
12	1109

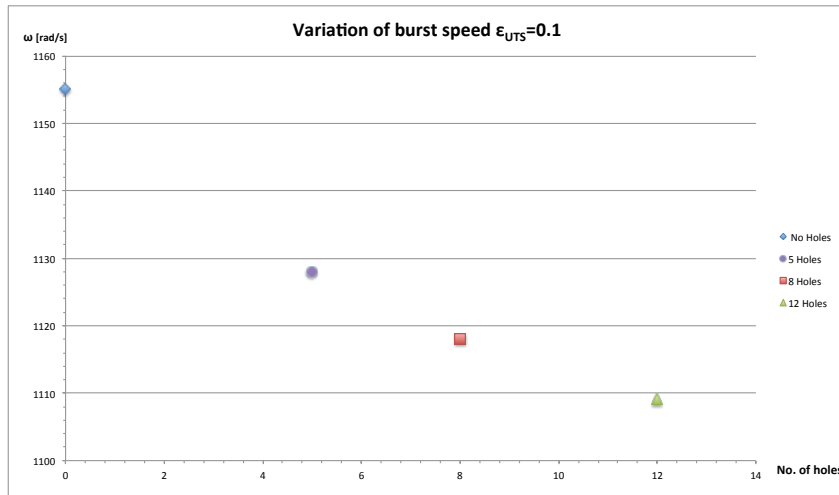


Figure 69: Variation of burst speed with the number of holes (curve 2)

Again, the principal stresses tendencies are plotted for two paths: in Figure 70 at a section far from the hole (*path 1*), and in Figure 71 at a section which passes through the hole (*path 2*).

In this simulation it is possible to highlight from the plot in Figure 71 the differences that occur when the number of holes increases: it is more evident, in fact, the fact that the disk with 5 holes has an higher burst speed, since the part working at the UTS is more extended, meaning that the disk survived some load increments more than the other two cases.

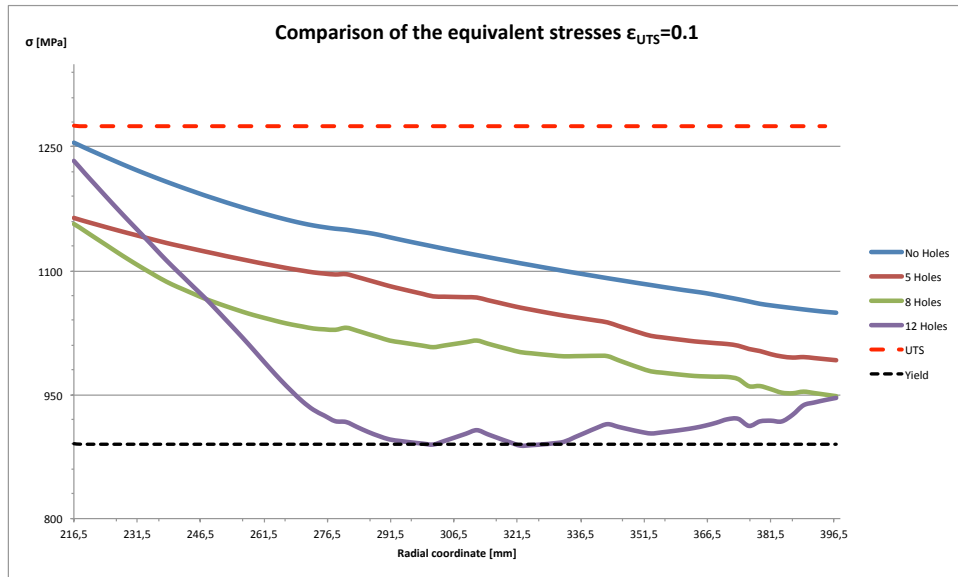


Figure 70: Comparison of equivalent stresses before burst (curve 2, path 1)

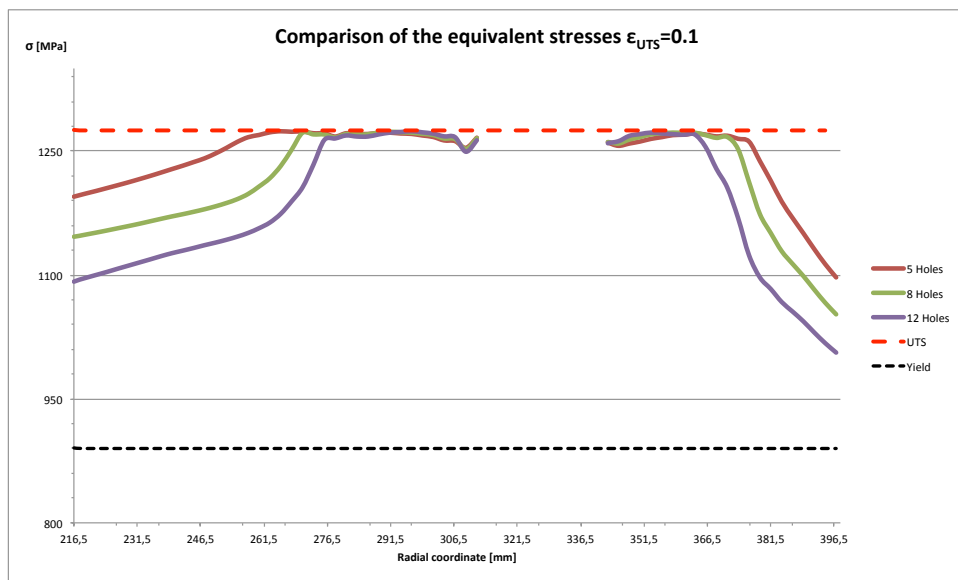


Figure 71: Comparison of equivalent stresses before burst (curve 2, path 2)

A further study has been conducted considering a real material curve (the mean curve showed in the previous chapter, Figure 72) and performing an elasto-plastic analysis with *Large Displacements*.

The material curve used is the same presented in the previous chapter, where the one considered is the mean curve of the experimental set.

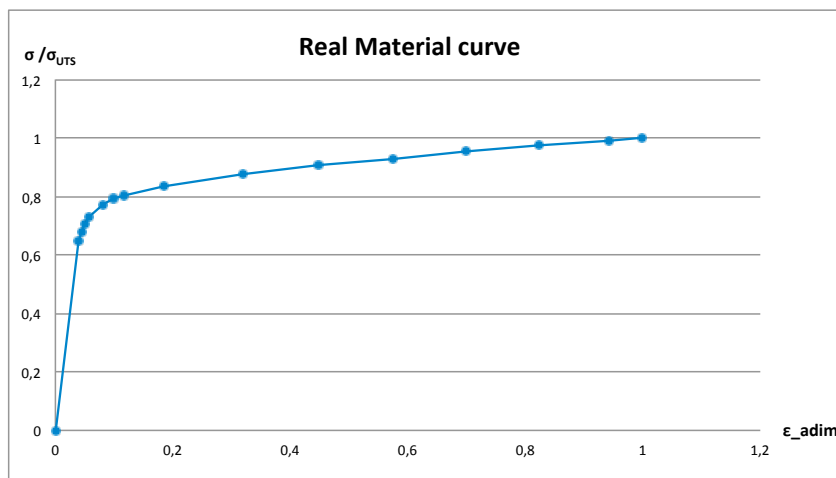


Figure 72: Mean real material curve

In order to show qualitatively the tendency of both burst speed and stresses along the radial direction, the same analyses conducted before for the idealized curves have been repeated, varying the number of holes each of 30 mm diameter, comparing also the results with the one

obtained using the *Small Displacement* option.

The trend of burst speed variation as the number of holes increases is shown both in Table XI and in Figure 73. Again, according to the *Large Displacement* analysis on the 3D model set with a cyclic symmetry, there is a reduction of burst speed, though moderate, when the number of holes increases.

TABLE XI: VARIATION OF BURST SPEED WITH THE NUMBER OF HOLES - REAL CURVE

No. of holes	ω_{burst} [rad/s]
0	1320
5	1295
8	1290
12	1285

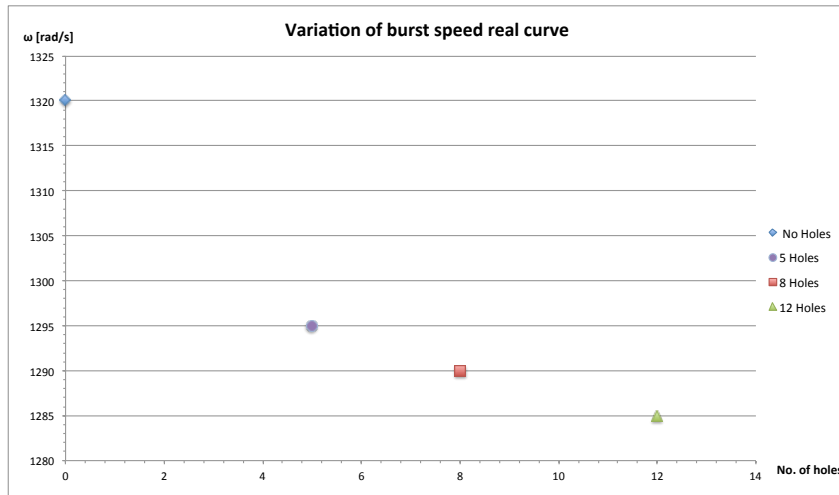


Figure 73: Variation of burst speed with the number of holes (real curve)

The same plots of stresses produced for the previous two simulation can be generated also for the real curve, reported here in dimensionless form, like the material curve itself.

So in Figure 74 and in Figure 75 it is possible to look at the equivalent stresses at the last substep before burst, traced respectively in a section between the holes and in a section passing through one of them.

Notice that on the same plot it has been reported also the trend of equivalent stress calculated using the *Small Displacement* option, which gives exactly the same results for all the three different cases: 5, 8 and 12 holes. Using the SD option the software provides, as expected, an higher rotational speed at which the analysis is interrupted, since burst occurs when in all the disk the equivalent stress is reached ($\omega_{burst_SD} = 1430rad/s$).

This confirms the hypothesis of failure due to inertial instability and that it occurs in the radial

direction (*hoop mode*) along those direction that passes through the hole, since near the holes the disk has an equivalent stress equal to the ultimate strength.

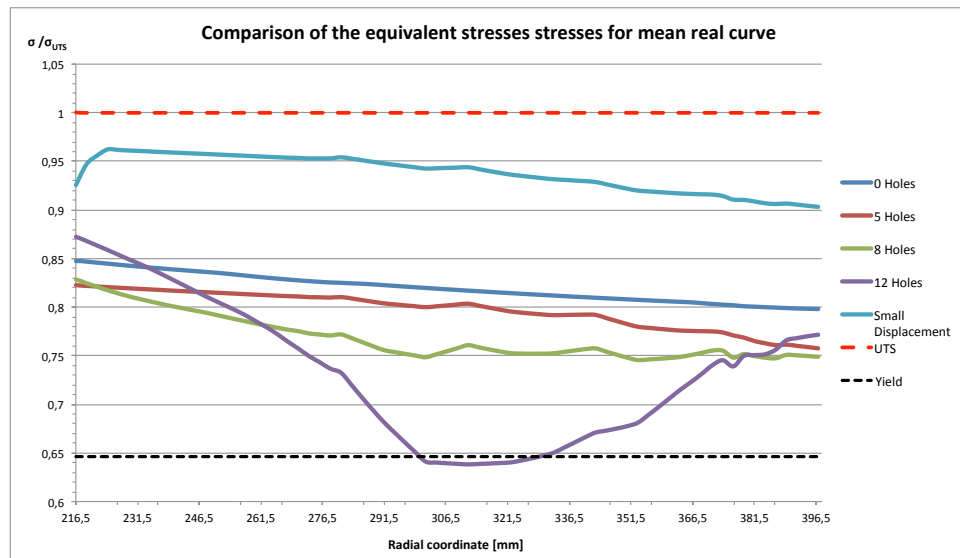


Figure 74: Comparison of equivalent stresses before burst (real curve, path 1)

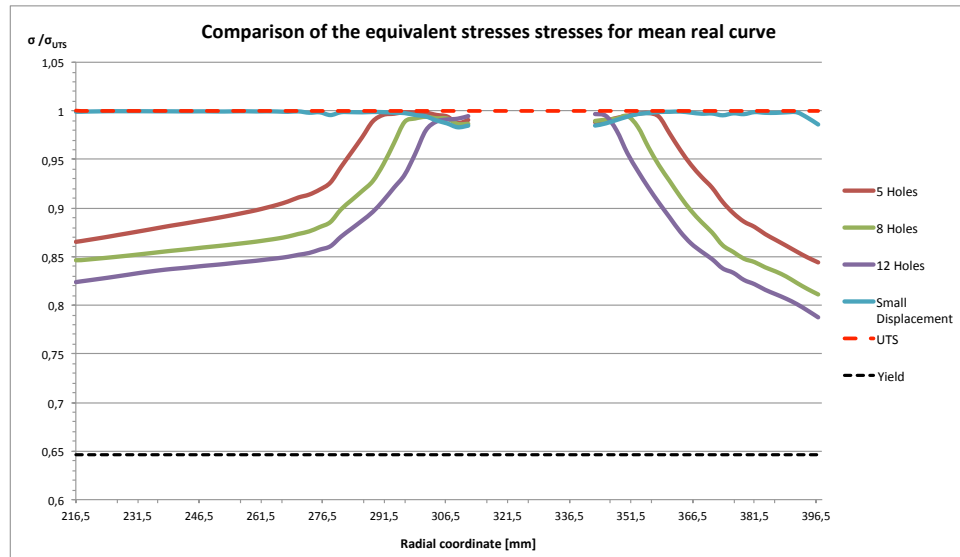


Figure 75: Comparison of equivalent stresses before burst (real curve, path 2)

Figure 76, finally, shows evolution of the equivalent stress along the second path for the case of a disk with 5 holes.

The rotational speed at which part of the disk starts to plasticize (passes the yielding stress) is between 750 rad/s and 900 rad/s , while the total plasticization of the cutting section ($\sigma_{eq} > \sigma_y$ at each radii) is verified around 1125 rad/s .

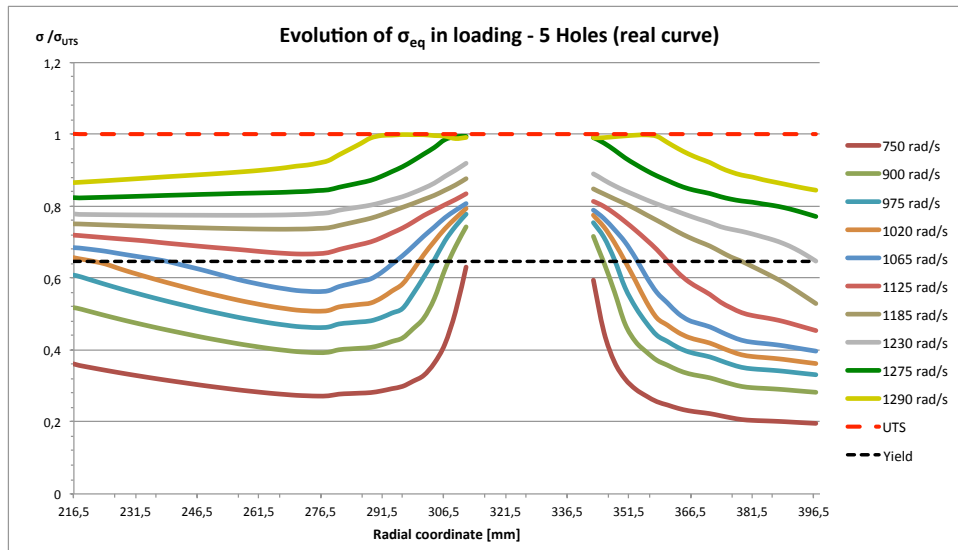


Figure 76: Evolution of equivalent stress in loading (5 holes, real curve)

7.2.2 Variation of the holes dimension

A second study, instead, is focusing on the effect of the dimension of the holes onto burst. Considering the mean real material curve defined previously and fixing the number of holes, their dimension has been varied from a minimum diameter of 10 *mm* to a maximum of 50 *mm*.

So, in the following table are reported the value of burst speed given by the numerical code for two cases of disks with 5 and 12 holes and holes having the following diameters: 10 *mm*, 20 *mm*, 30 *mm*, 40 *mm* and 50 *mm*.

TABLE XII: VARIATION OF BURST SPEED WITH HOLES DIMENSION - REAL CURVE

	5 Holes	12 Holes
Holes diameter [<i>mm</i>]	ω_{burst} [<i>rad/s</i>]	ω_{burst} [<i>rad/s</i>]
10	1310	1309
20	1300	1297
30	1295	1285
40	1285	1277
50	1275	1270

As shown in Table XII, Ansys points out a decreasing value of burst speed as the dimension of holes increases, with a monotonic tendency. Moreover, for small dimensions very little differences (below the threshold value of 5 rad/s , which is the lowest increment of angular velocity set in the software) occur between the case with 5 holes and the one with 12 holes.

For the configuration with 12 holes, plots of the equivalent stress against the radial coordinate are reported in Figure 77 and Figure 78. Those plots allow to confirm that the presence of the holes moves the direction of preferential failure in the section that passes through the holes, since the equivalent stress reaches the highest value, equal to the ultimate strength, in proximity of the hole.

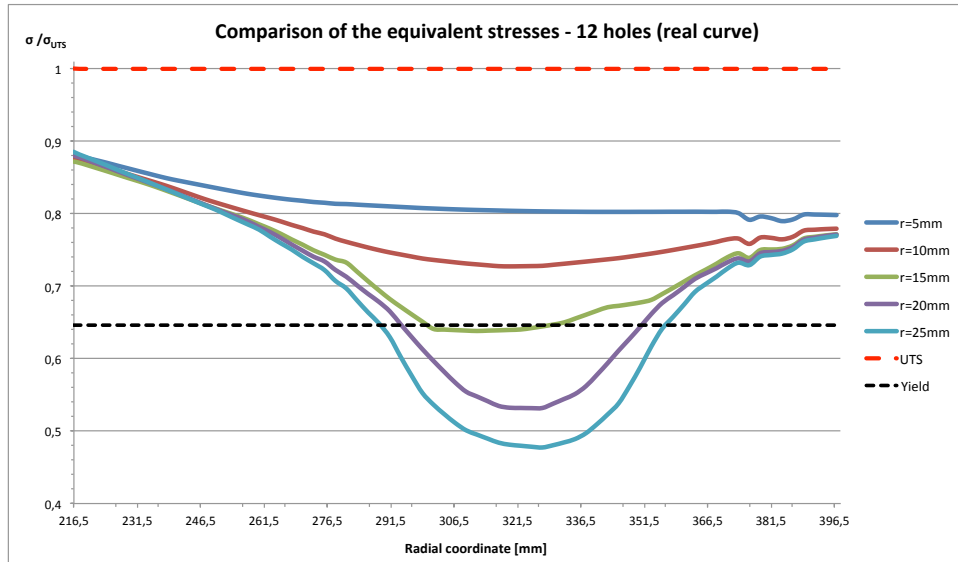


Figure 77: Comparison of equivalent stress before burst as dimension of holes varies (12 holes, path 1)

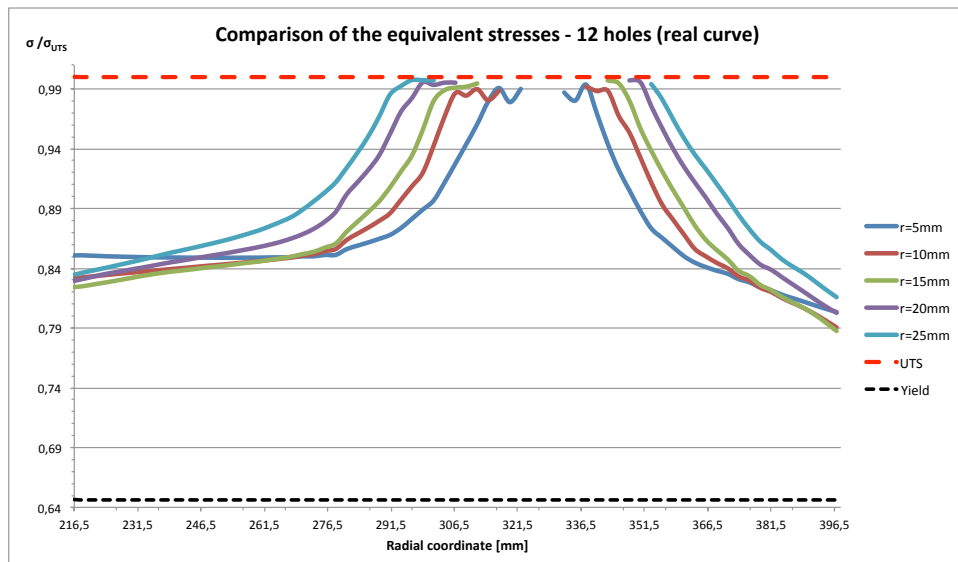


Figure 78: Comparison of equivalent stress before burst as dimension of holes varies (12 holes, path 2)

Curious is to notice from Figure 77, in which the equivalent stresses are considered in a section far from the holes, that as the holes dimension increases the stress in the web area (where holes are located) suffers a great reduction as it is evident looking at the two cases with diameters of 40 mm and 50 mm where it is widely below the yield value.

This means that the considering larger holes increases the perturbation in the stress composition in the area interested by the presence of the holes.

Having a look at the principal stresses along the same path is then really interesting, as reported in Figure 79. From this plot, in fact, it is clear that at radial position that correspond to the location of the holes, the first principal (hoop stress) tend to decrease, while the second principal (radial stress) increases.

Finally, for the case with the largest holes ($d = 50\text{ mm}$), the two principal stresses are locally equal each other. This condition might represents a limiting case, since a further increase of the radial stress would cause a different burst behavior and, most likely, a mode of fracture more similar to the *rim peel*.

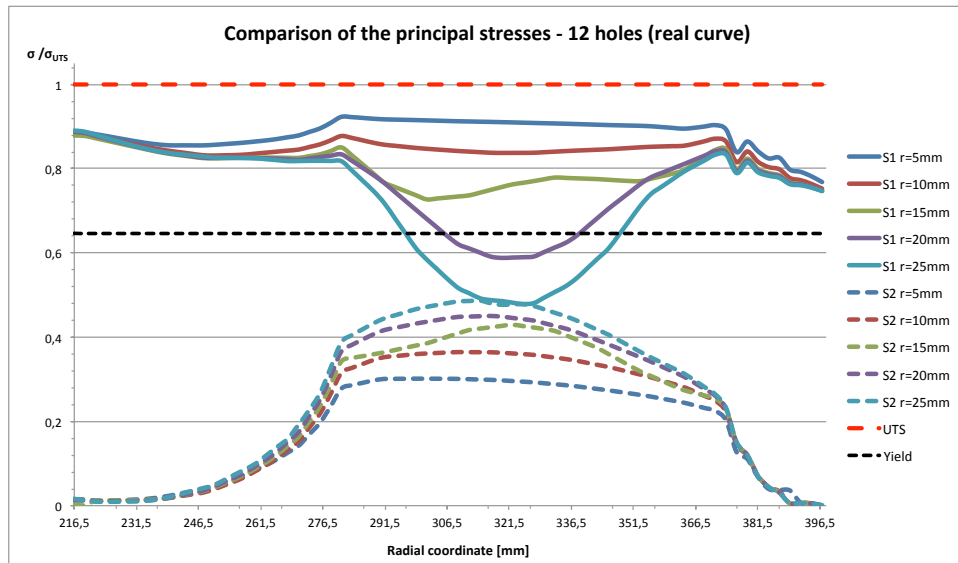


Figure 79: Principal stresses along path 1 for varying holes dimensions (12 holes)

In order to understand if *rim peel* is actually prevailing over the *hoop mode*, the study of the radial paths has to be compared with the plot of the stresses along the arc of circumference that passes through the hole (Figure 80).

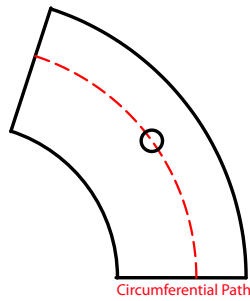


Figure 80: Circumferential path

For this reason, in the following pages a set of compared plots of principal stresses ($S1=hoop$ stress ; $S2=radial$ stress) and principal stresses for some of the above configurations are reported in order to show the differences between them and look also into the circumferential path traced upon the basic sector.

- 5 holes - $d = 10 \text{ mm}$:

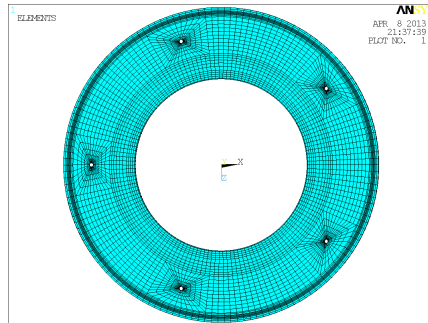


Figure 81: Disk with 5 holes of 10mm diameter

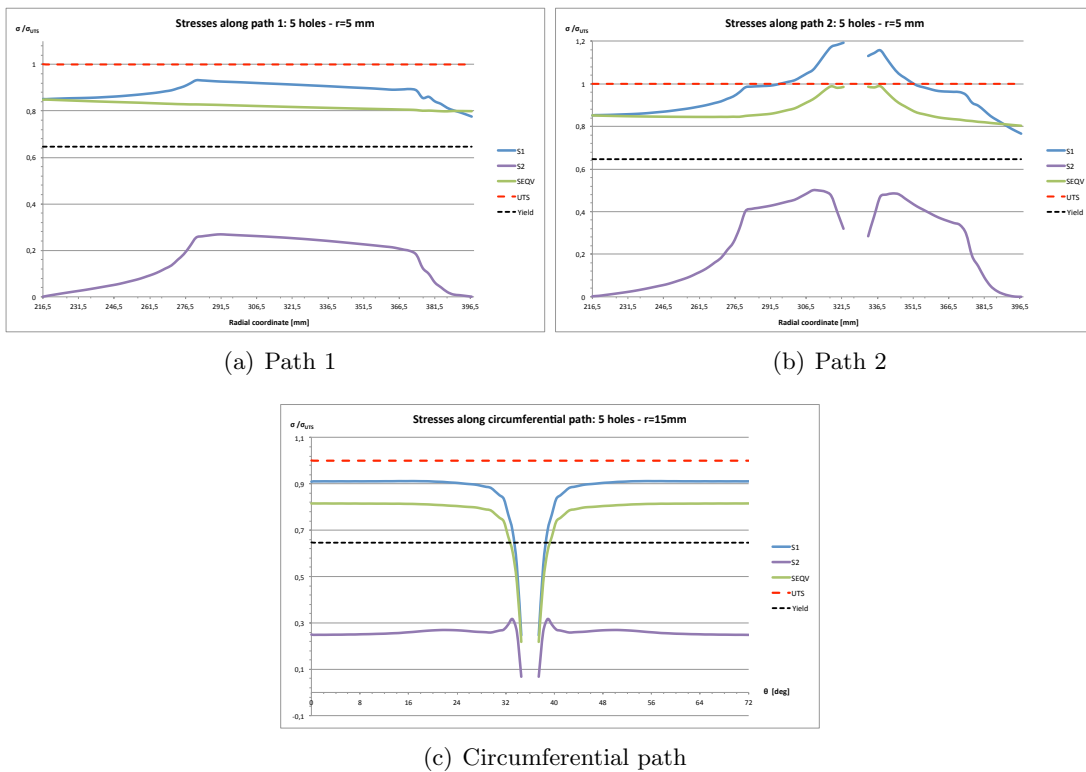


Figure 82: Comparison of stresses along different paths (5 holes, $d = 10 \text{ mm}$)

- 5 holes - $d = 30$ mm:

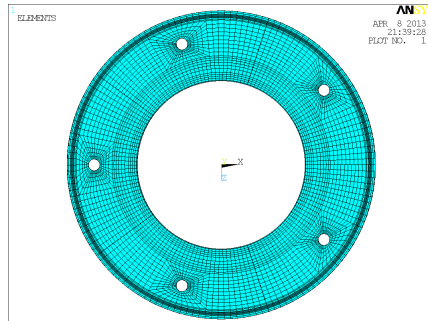


Figure 83: Disk with 5 holes of 30mm diameter

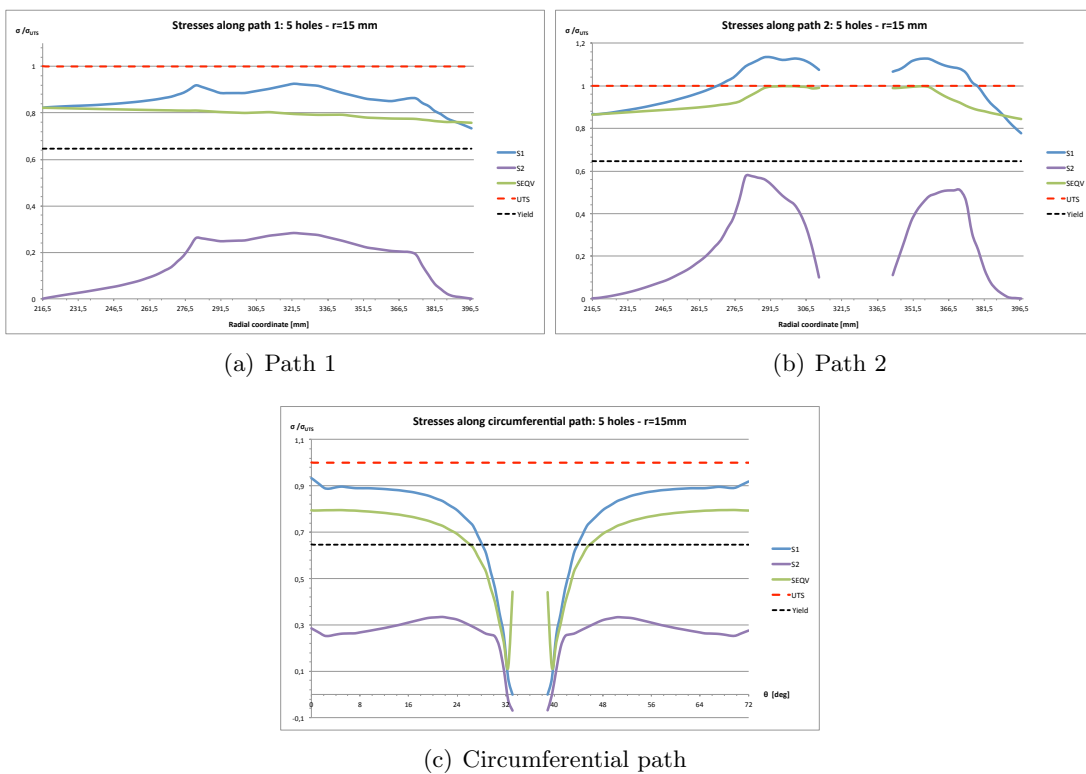


Figure 84: Comparison of stresses along different paths (5 holes, $d = 30$ mm)

- 5 holes - $d = 50 \text{ mm}$:

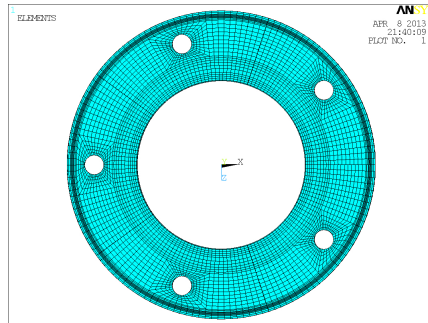


Figure 85: Disk with 5 holes of 50mm diameter

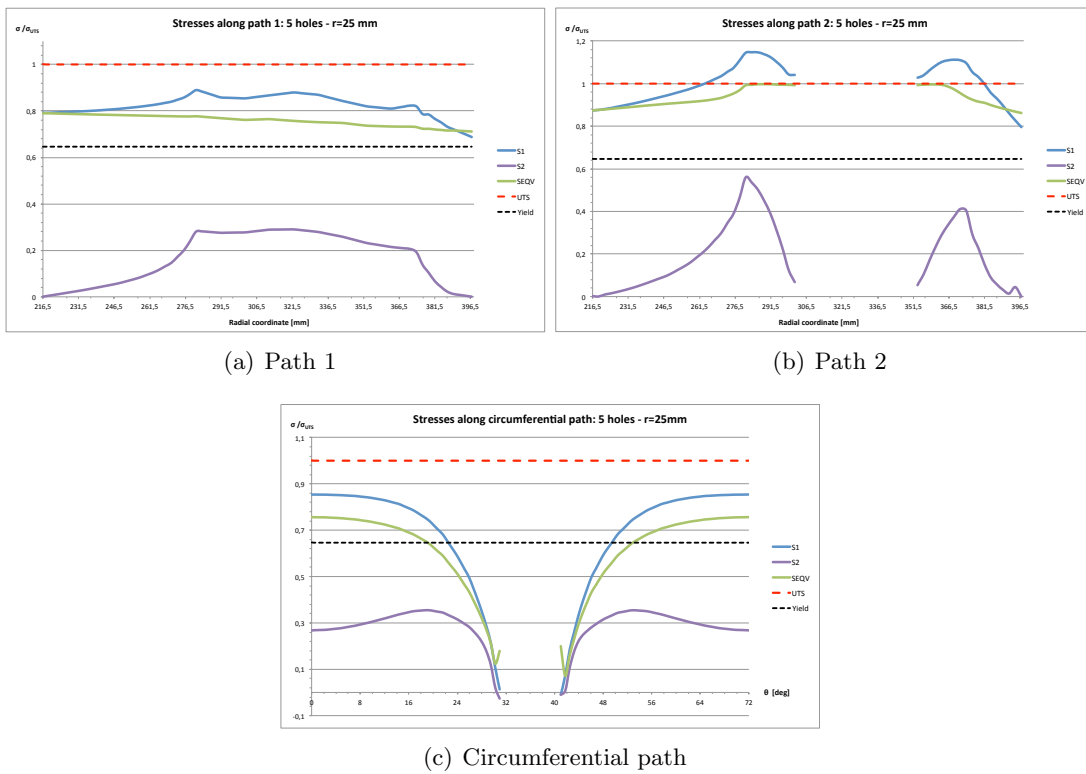


Figure 86: Comparison of stresses along different paths (5 holes, $d = 50 \text{ mm}$)

- 12 holes - $d = 10\text{ mm}$:

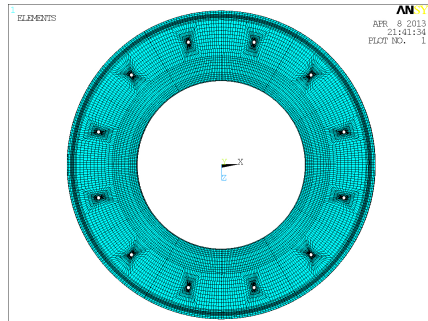


Figure 87: Disk with 12 holes of 10mm diameter

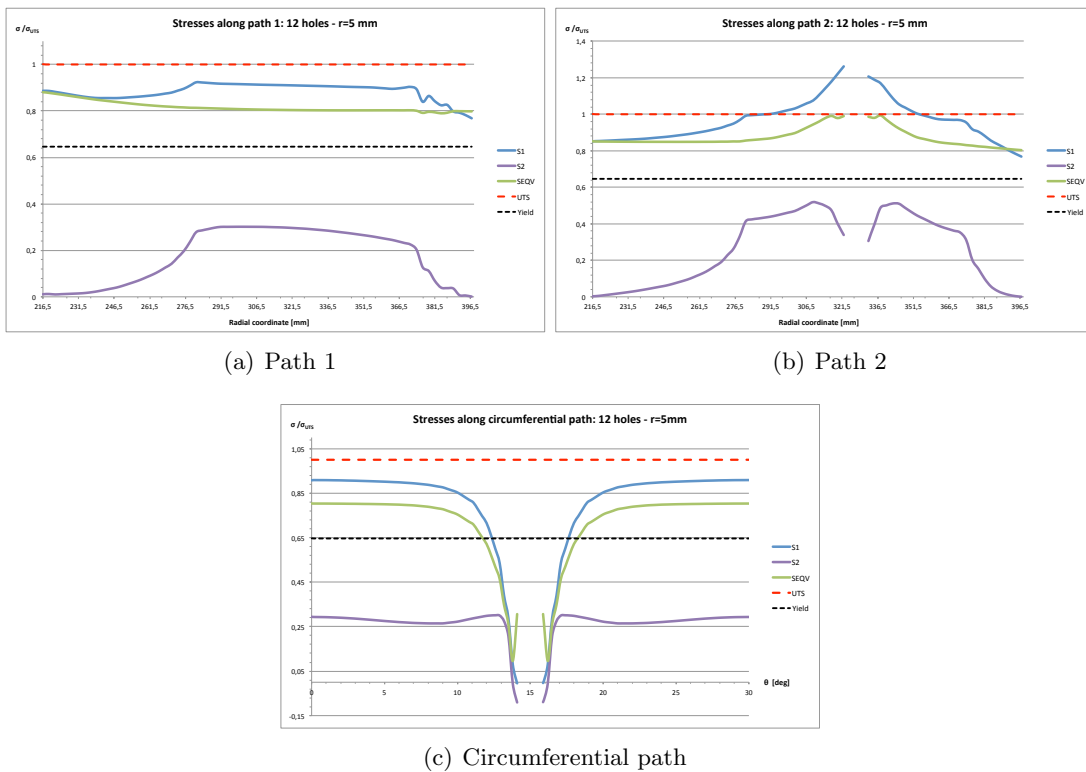


Figure 88: Comparison of stresses along different paths (12 holes, $d = 10\text{ mm}$)

- 12 holes - $d = 30\text{ mm}$:

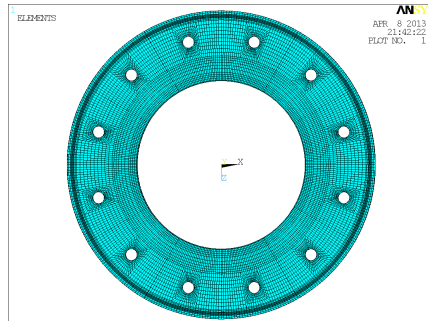


Figure 89: Disk with 12 holes of 30mm diameter

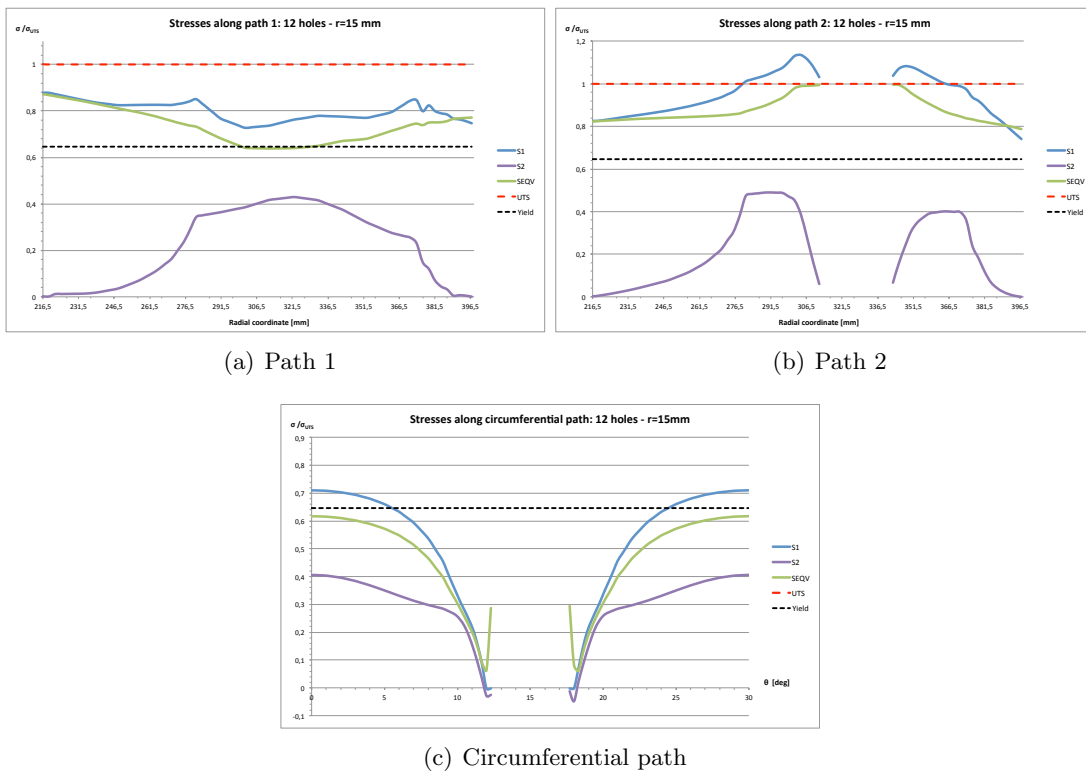


Figure 90: Comparison of stresses along different paths (12 holes, $d = 30\text{ mm}$)

- 12 holes - $d = 50 \text{ mm}$:

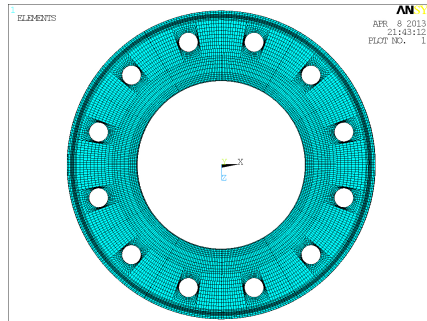


Figure 91: Disk with 12 holes of 50mm diameter

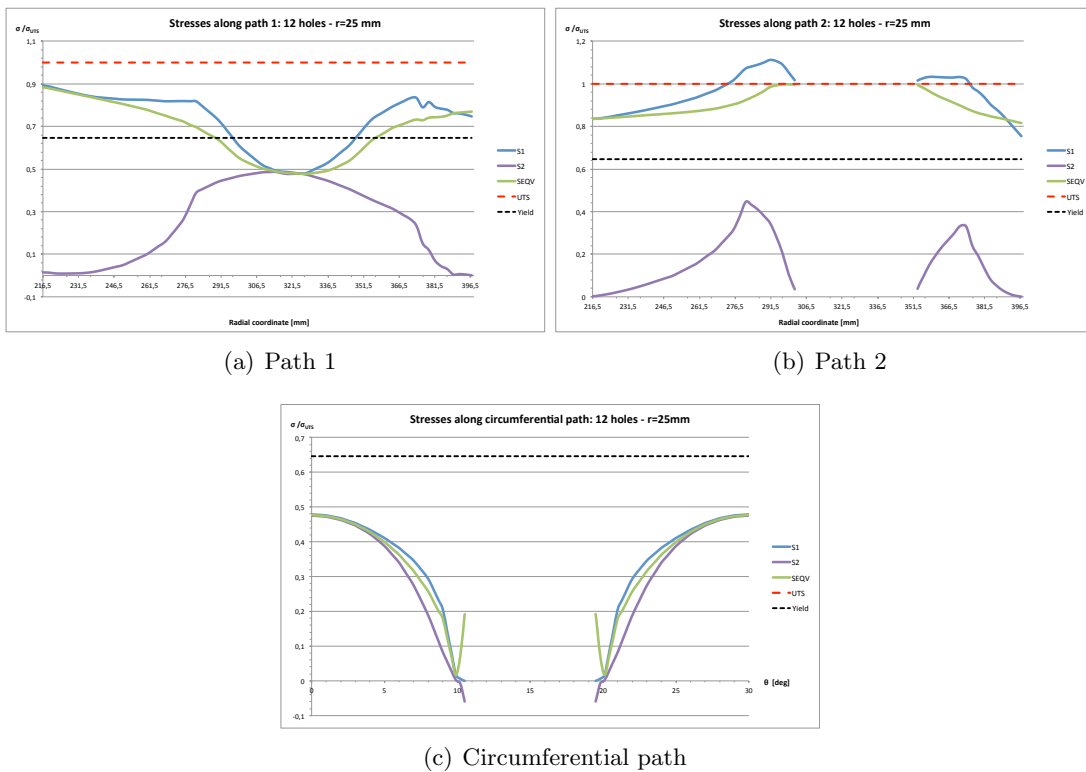


Figure 92: Comparison of stresses along different paths (12 holes, $d = 50 \text{ mm}$)

By comparing the results showed above it is possible to deduce that the *rim peel burst* is not verified in any of those configurations. Looking at the equivalent stress along the circumferential path, in fact, it appears clear that the equivalent stress at different θ is never reaching the UTS, condition that is instead verified along the radial path that passes through the hole (*Path 2*).

Moreover, from the plots it is not difficult to notice that the holes tend to ovalize along the circumferential direction (as shown also in Figure 93), since on the edges of the hole the hoop stress (S1) is zero and the radial stress (S2) is negative, hence it induces a compressive deformation.

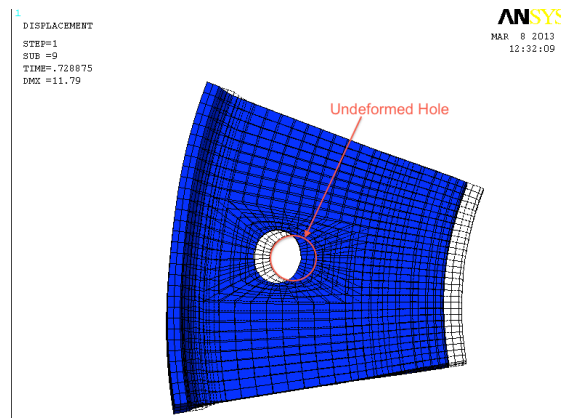


Figure 93: Deformed and undeformed shapes

The *rim peel burst* is a rather rare failure mode, verified when the disk in the web area fails in keeping the rim attached to the bore, due to a prevalent effect of the radial stress over the

hoop stress. From the case studied before, one limiting case, if the only load is the centrifugal force, might be for example the configuration with 12 holes of 50 mm diameter, since the radial and the hoop stress reach the same value in the area between the holes. It has been investigated, to confirm this idea, the same case of the disk with holes of 50 mm, but increasing the number of holes up to 36 and from the contour plot of equivalent stress in Figure 94 it is possible to notice how this is maximum along the circumference, which indicates the predominance of *rim peel* over *hoop mode*.

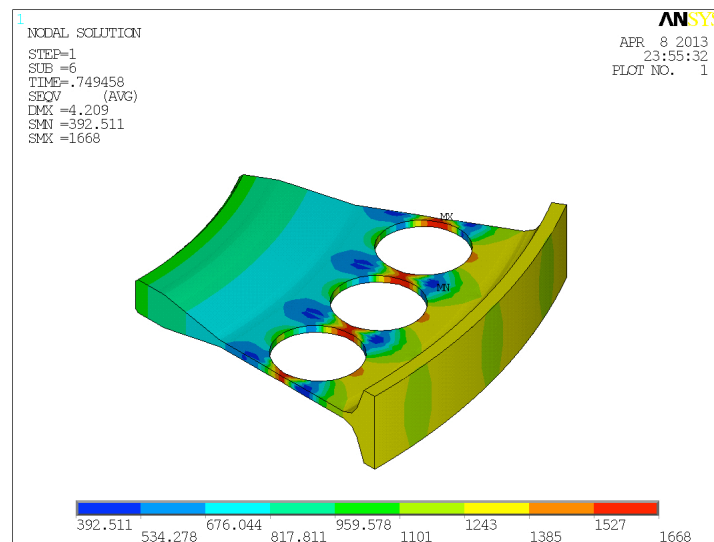


Figure 94: Contour plot of the equivalent stress: disk with 36 holes ($d = 50 \text{ mm}$)

Comparing the two contour plots of the von Mises equivalent stress showed in Figure 94 and 95 it is possible to see that the area at maximum stress is different if considering the *rim peel* (Figure 94), since this is located in the gap between the holes. Also the composition of the equivalent stress is different: in the *hoop mode* burst, where the maximum stress is maximum along the radial direction (Figure 95) the greatest contribution to it derives from the hoop stress, since the radial stress is taken as zero at the holes boundary; on the other side, the *rim peel* the greatest component of the equivalent stress in the peak area is the radial stress (Figure 94).

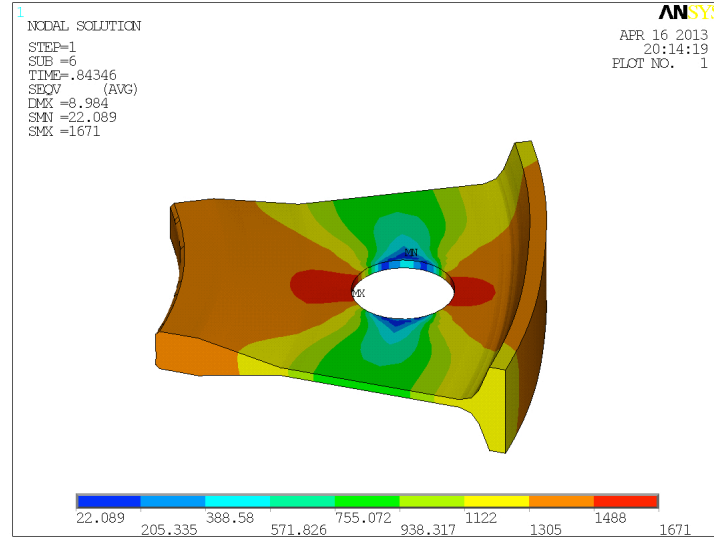


Figure 95: Contour plot of the equivalent stress: disk with 12 holes ($d = 50 \text{ mm}$)

CHAPTER 8

EQUIVALENT TWO-DIMENSIONAL MODEL FOR HOLED DISKS

The three-dimensional model created in the previous chapter can be considered as a reference when studying the inertial instability through a Finite Element analysis. The results, in fact, show that Ansys correctly recognizes the burst conditions for both *hoop mode burst* and *rim peel burst* if the *Large Displacement* is used on that kind of model. However, this kind of analysis has a significant drawback, since the complexity of the model requires really time demanding calculations.

The challenge, then, is to build an equivalent two-dimensional model that can consider the presence of holes in the web area in order to perform a burst analysis in much less time. Moreover, the Robinson criteria can be applied on a 2D case as done in Chapter 6, with the only constrain that Robinson is only working if *hoop mode burst* is considered.

In this chapter, then, a modified two-dimensional model is presented and, for a bunch of selected configurations among the ones presented in Chapter 7, the burst limit is found considering both the value given by the FE code as the substep corresponding to instability, and the one found by applying the Robinson's criterion.

The considered configurations in terms of number of holes and dimensions are considering a

disk with 5 holes and one with 12 holes, with holes of diameter equal to 10 mm, 30 mm and 50 mm.

8.1 Model description: geometry and material properties

Starting from the geometry described in Section 6.1, the presence of holes can be modeled modifying the material properties of the disk in the region in which holes are present.

This has been done by considering a suitable orthotropic material in the region in which holes are present and scaling the values of all the mechanical properties by a ratio that depends on the removed material, namely the number of holes.

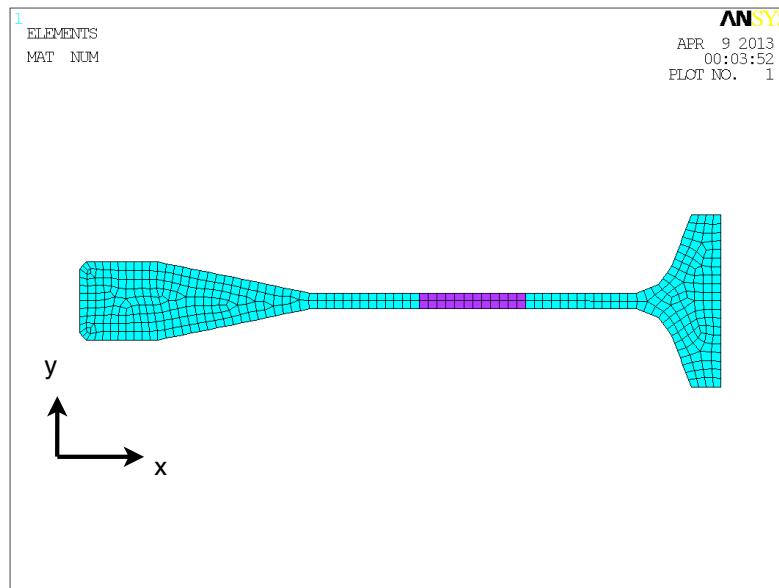


Figure 96: Bi-dimensional model with orthotropic material in the holes region

In figure 96 it is possible to see the meshed model for one particular configuration: the highlighted elements are those which consider the new orthotropic material and this area is as much wide as the holes diameter.

An orthotropic material has generally three axes of elastic symmetry, so it presents a matrix of elastic coefficient is characterized by 9 parameters. Its mechanical properties are different along each axis, thus the orthotropic materials are anisotropic materials.

So, the material model that has been set in the holes area is using an *linear orthotropic* material model with scaled values with respect to the isotropic material in the radial and the axial direction, while all the values in the tangential direction are zero.

The proposed scaling in a cylindrical coordinate system is the following:

$$\begin{aligned}
 E_z = E_r = E \cdot \gamma & & E_\theta = 0 \\
 \nu_{rz} = \nu \cdot \gamma & & \nu_{r\theta} = \nu_{z\theta} = 0 \\
 G_{rz} = \frac{E_r}{2(1 + \nu_{rz})} & & G_{r\theta} = G_{z\theta} = 0 \\
 \rho = \rho \cdot \gamma & &
 \end{aligned}$$

where:

- $\gamma = Truevolume/Fullvolume$ is the material properties scaling factor;
- E is the longitudinal modulus of elasticity;
- G is the shear modulus;
- ν is the Poisson's ratio;
- ρ is the density.

Since Ansys does not accept zero values for the modulus of elasticity and for the shear modulus, those values have been substituted with 1, which is very close to 0 if compared to the numbers that usually characterize those two parameters. Besides, considering that we are dealing with a Cartesian reference frame used in the geometry generation (and also shown in Figure 96), $r = x$, $z = y$ and $\theta = z$.

For what concerns the other part of the disk, the material model is configured as isotropic considering the mean real material curve used for the study conducted in the previous chapter and shown in Figure 72. In this way it is possible to carry out a comparison between the results obtained by using this bi-dimensional configuration, the Robinson's criterion and the three-dimensional model (that is used as a reference).

8.2 Burst limit comparison with the 3D model and the Robinson's criterion

Having set up a two-dimensional model that considers the presence of holes, it is possible to present a comparison between the results obtained using the *Large Displacement* option in Ansys over both the 2D model and the 3D model and, eventually, consider the results obtained

by applying the Robinson's criterion.

Using a two-dimensional model, in fact, it is possible to implement Robinson extracting the average circumferential stress at a specific substep and, then, use the proportionality defined by the formula in Equation 3.39.

The solution options used to run the *Large Displacement* simulation on the new model are the following:

- *Automatic time stepping*: Off and 300 substeps considered for the load increments, with the set global angular velocity of 1500 rad/s ;
- *Line search*: On, which tells the software to use the Newton-Raphson method for the non-linear calculation.

Robinson, on the other hand, does not consider any deflection, so the *Small Displacement* option should be used to calculate the average hoop stress ($\sigma_{c,m}$) or, equivalently, the *Large Displacement* results can be used having care to look for $\sigma_{c,m}$ for loads that are not causing plasticization.

In the following table the burst speeds obtained by using those three methods over the selected geometries are listed.

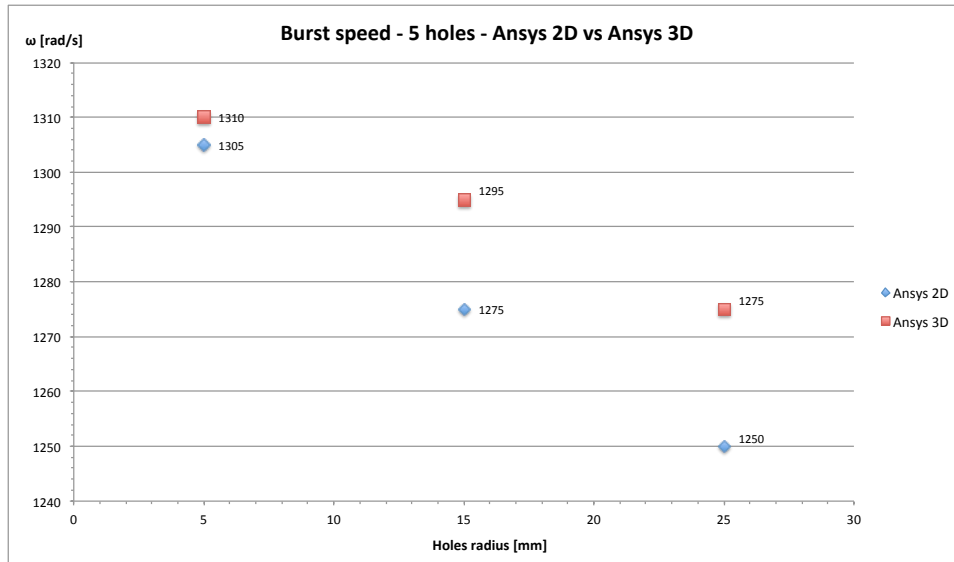
TABLE XIII: BURST SPEED FOR HOLED DISKS USING ANSYS 2D, ANSYS 3D AND ROBINSON'S CRITERION

<i>Holes and dimension</i>	<i>Ansys 3D-LD [rad/s]</i>	<i>Ansys 2D-LD [rad/s]</i>	<i>Robinson [rad/s]</i>
5 Holes - $d = 10\text{ mm}$	1310	1305	1339
5 Holes - $d = 30\text{ mm}$	1295	1275	1341
5 Holes - $d = 50\text{ mm}$	1275	1250	1346
12 Holes - $d = 10\text{ mm}$	1309	1305	1339
12 Holes - $d = 30\text{ mm}$	1285	1280	1345
12 Holes - $d = 50\text{ mm}$	1270	1260	1256

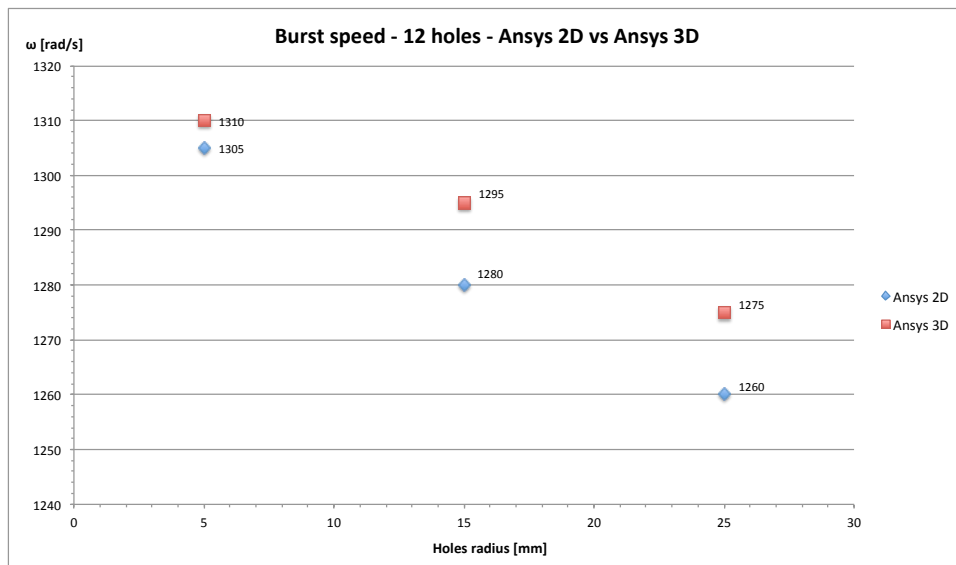
The values from Table XIII can be represented graphically in the plane $\omega - \text{No. of holes}$ in order to compare the results obtained using the two-dimensional model with the ones of the previous chapter. From the plots is much easier to understand graphically if either the elasto-plastic analysis using the modified 2D model and Robinon's criterion are proposing results comparable with the ones obtained with the 3D model described in Chapter 7.

Figure 97 shows that the two-dimensional model gives back some reasonable results if the burst limit is identified as the value at which the solution diverge.

The trend obtained, in fact, follows quite well the one pointed out by the study conducted on the three-dimensional model: burst speed, hence, is lower if larger holes are considered; while increasing the number of holes from 5 to 12, differences in terms of burst speed are as bigger as the dimension of holes increases.



(a) 5 Holes



(b) 12 Holes

Figure 97: Comparison 2D model vs 3D model

Comparing, instead, the tendencies of stresses obtained in the two-dimensional model with those in the three-dimensional analysis for the particular case of a disk with 5 holes of 30 mm diameter, it is possible to see whether the modified 2D model is following the same stress tendency along the radial direction.

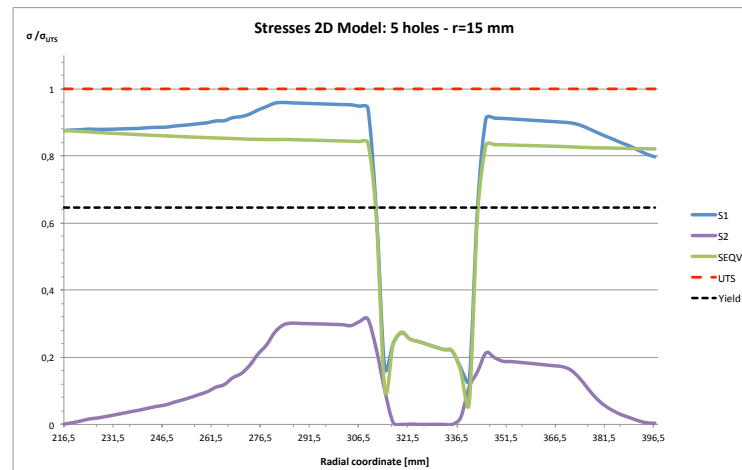


Figure 98: Stress along the radius - 2D model (5 holes, $d = 30$ mm)

As it is possible to see comparing Figure 98 and 99, the new two-dimensional model presents a different evolution of stresses if compared to the two paths highlighted for the three-dimensional one. In particular, some non-real results are displayed in the hole area. This is due to the definition of the orthotropic material that was set in order to correctly recognize

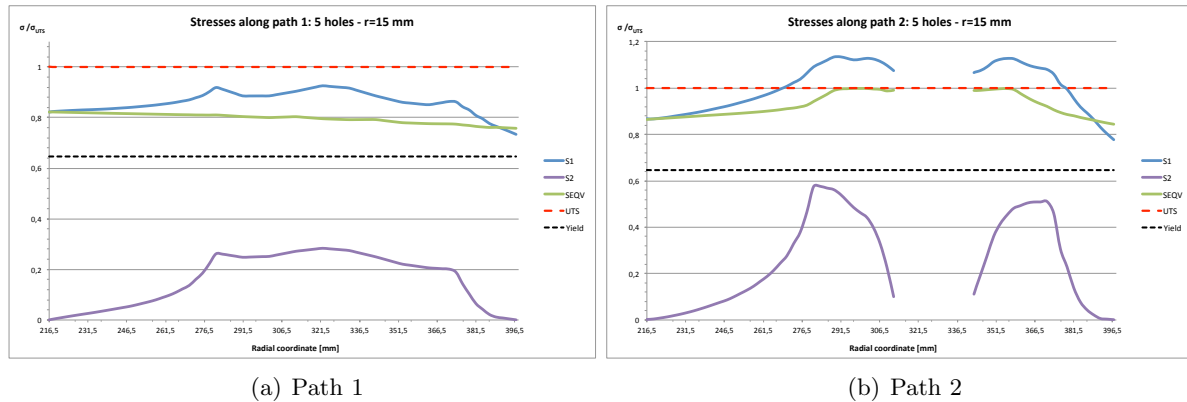
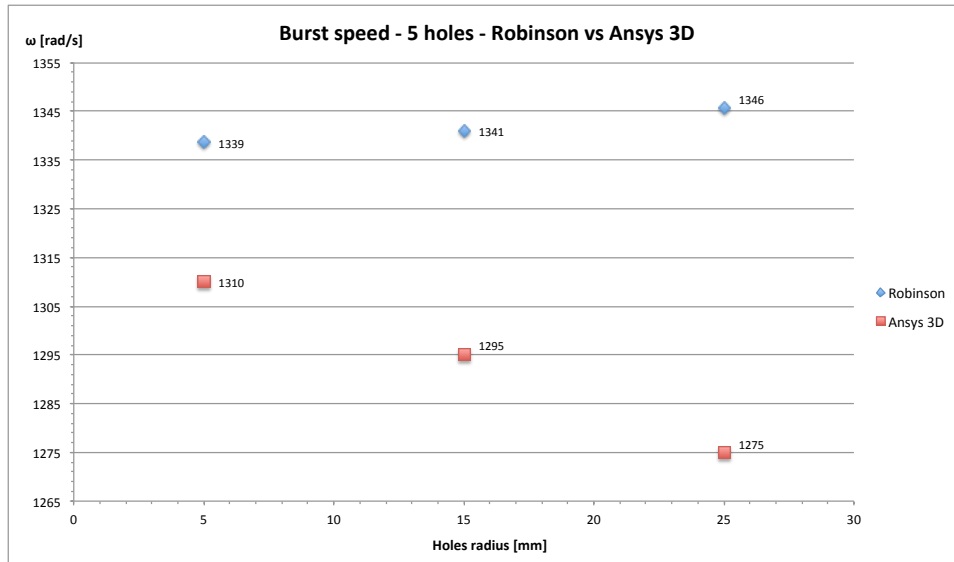


Figure 99: Stress paths along the radius - 3D model (5 holes, $d = 30 \text{ mm}$)

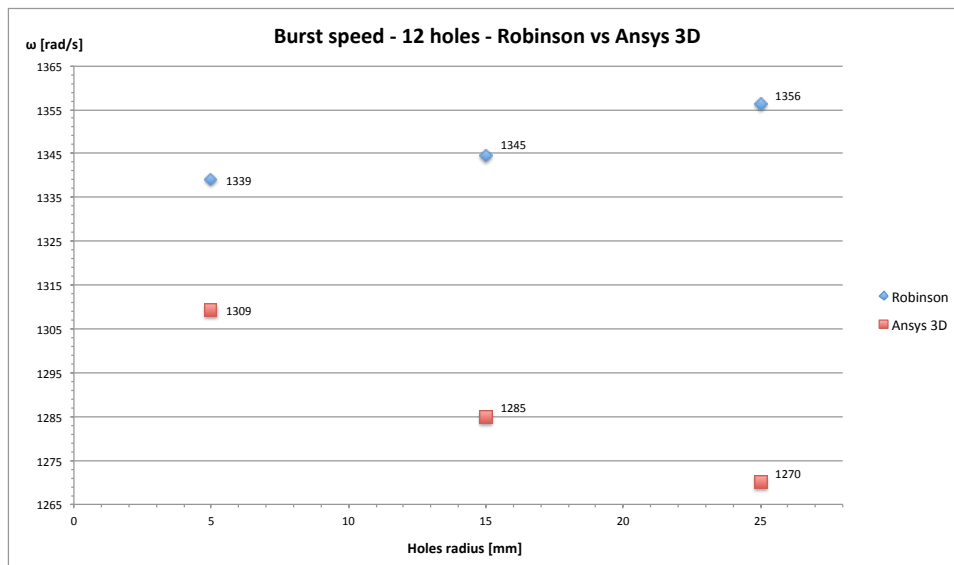
the variations in term of burst speed as the holes configurations vary. Neglecting this part of the disk and considering only the other results on the elements modeled with the isotropic material, instead, stresses are sort of an averaged value from those obtained following the two paths (traced at different angles).

It can be concluded that the bi-dimensional model created here, with the orthotropic material instead of holes, can be correctly compared to the reference 3D model if looking at the burst speed, but it doesn't give enough information regarding the stresses, meaning that it does not identify the mode of fracture.

On the other hand, a totally different trend in terms of burst speed is obtained using the Robinson's criterion. This completely fails in recognizing the presence of holes as clearly shown in Figure 100, where the tendency obtained applying the proportionality expressed by Robinson



(a) 5 Holes



(b) 12 Holes

Figure 100: Comparison Robinson vs 3D model

is diverging from the results achieved using the *Large Displacement* option in Ansys over the 3D model.

Robinson's criterion gives much larger values for burst speed for each configuration and those values tend to increase as the number of holes and their dimensions increase, in countertrend to what was pointed out using the numerical method on both the other studied models.

A reason to this result can be derived thinking about the way the formula is working when the material in the holes area is changing. The Robinson's formula (Equation 3.39) considers only the hoop stress occurring in the disk at a certain rotational speed and the ultimate strength, those values are used to carry out a proportion and to find the bust limit.

With the material model set up in the new bi-dimensional model, however, the tangential stiffness is ideally null, so the holes area gives a zero contribution to the average hoop stress. At the same time, the scaling of the material properties has been done also on the density of the material. This causes a reduction on the centrifugal load ($\Phi_V = m r \omega^2$), and for this reason the burst speed increases for greater material removals (larger holes).

As a proof, the same calculations have been repeated scaling the materials in all its mechanical properties, except for the density. As expected, with this setting, the average hoop stresses found are the same for all the holes configurations, no matter of their number or dimensions.

This allows to state that the Robinson's criterion is certainly failing if used on this particular kind of model that substitutes the holes with an orthotropic material: Robinson considers the

proposed scaling used for the material only because when dealing with the density reduction in a region of the body, while the change in Young's modulus don't affect at all the burst. Looking at the formula showed in Equation 6.1, in fact, only density and σ_{UTS} are present, while the Young's modulus, E , is not present at all.

CHAPTER 9

CONCLUSIONS AND FURTHER DELOPMENTS

The research work carried out to complete this thesis allows, in conclusion, to show how the study of the burst condition of turbine rotor disks is possible using in the commercial Finite Element code Ansys both a two-dimensional model and a three-dimensional one.

The initial considerations developed from previous research in the field on inertial instability, can be extended confirming that burst is actually following this hypothesis and it is a strain dominated phenomenon, since the effect of the material curve are largely influencing the results in the elasto-plastic analysis conducted using the *Large Displacement* option. This kind of simulation, much more realistic than the one using the *Small Displacement* consider the update of the geometry, thus the increase of the inertial load due to the radial deflection of the disk is eventually causing an unbearable situation for the disk and its failure, as shown in Chapter 5.

The main goal of this thesis was, however, to focus the study on a non-axisymmetric disk, that can consider the effects of redundant geometry interruptions, such as holes in the web area or the presence of slots in the rim.

For this reason, after showing the effectiveness of the two-dimensional model for a solid axisymmetric disk, this has been compared with a three-dimensional model that is using the cyclic symmetry feature of Ansys. This new model perfectly matches with the first one, and it can be used as a reference in the elasto-plastic analysis for burst speed in presence of holes in the

web area, like it was done in Chapter 7.

The implementation of a three-dimensional model in Ansys is very useful in order to understand the behavior at burst of the disk: it emerged from the simulation that inertial instability is still the dominant phenomenon that cause failure of the disk, even in presence of holes, and that usually burst can be classified as *hoop mode burst*, since the failure more likely occurs along the radial direction and fracture starts near the hole. However, it was proven that as the pitch between holes is reduced (for example the holes dimension increases or the number of holes is very high) burst can eventually be in the *rim peel* mode, which is not even considered by the semi-empirical theory developed by Robinson.

A keypoint of the this research topic is, in fact, to bring into discussion the application of the Robinson's criterion, which is still largely used for its easiness. This formula gives some acceptable results if applied on axisymmetric disks: even if it does not consider the plastic deformations, but only the ultimate strength of the material, the results are quite close (in a conservative way) to those obtained by Ansys. For this reason, this criterion is usually accepted as a rule of thumb when studying burst for an axisymmetric structure.

Totally different results were found, instead, in case of a holed disk: in this case Robinson clearly fails in following the correct trend in terms of burst speed reduction when the number of holes and their dimension increase. Moreover, Robinson is not considering at all the possible

rim peel burst condition, hence it should not be considered as a reliable method to investigate burst in case holes are present in the disk.

In order to apply the analytic formula, in Chapter 8 it has been presented a new two-dimensional model that uses a scaled orthotropic material so that it is possible to consider the presence of holes in the web area. The elasto-plastic numerical analysis has been performed with quite accurate results in terms of burst also for this new model, but with much less time demanding calculations than the three-dimensional one.

So in conclusion it is possible to affirm two things. First of all Robinson's criterion is not as reliable as many companies in the aerospace industry think: it doesn't consider at all the effects of a plasticity of material overestimating the value of burst and it is not properly working in case of holed disk. Secondly a three-dimensional model set as shown in this thesis correctly recognizes the burst condition for both *hoop mode burst* and *rim peel burst*, and also provides a lot of information regarding the distribution of stresses in the disk at loads before burst.

However, this kind of analysis is very time demanding, so it has been shown that in case of *hoop mode burst* of a disk with holes in the web area, a two-dimensional model as the one described in Chapter 8 can be used in order to have an general indication about the entity of the burst speed, even if it does not give enough details on the stress occurring in the structure, for which the application of the three-dimensional study has revealed to be fundamental.

Future studies may start from the results presented here. In particular, more complex geometries can be studied using *Large Displacement* simulations in Ansys for both three and two dimensions. For example the presence of blade slots or connecting flanges can be implemented, as well as the load due to the force applied on blades or the effects of thermal loads.

Moreover, the setup of the two-dimensional model can be refined, investigating more deeply the effects of the scaling of the orthotropic material in presence of non-axisymmetries, looking both at the burst speed variations and stress tendencies, so that this kind of model can be used as a preliminary study on the design of rotating disks.

CITED LITERATURE

1. Hill, P. and Peterson, C.: *Mechanics and Thermodynamics of Propulsion*. Addison-Wesley, 1992.
2. Squarcella, N.: Calcolo della velocità di scoppio per dischi rotanti. Master's thesis, Politecnico di Torino, 2013.
3. Ugural, A. and Fenster, S.: *Advanced Strength and Applied Elasticity*. Pearson Education, 2003.
4. Mazière, M., Besson, J., Forest, S., Tanguy, B., Chalons, H., and Vogel, F.: Overspeed burst of elastoviscoplastic rotating disks - part 1: Analytical and numerical stability analyses. *European Journal of Mechanics - A/Solids*, 28(1):36 – 44, 2009.
5. Mazière, M., Besson, J., Forest, S., Tanguy, B., Chalons, H., and Vogel, F.: Overspeed burst of elastoviscoplastic rotating disks - part 2: Burst of a superalloy turbine disk. *European Journal of Mechanics - A/Solids*, 28(3):428 – 432, 2009.
6. Bhaumik, S., Bhaskaran, T., Rangaraju, R., Venkataswamy, M., Parameswara, M., and Krishnan, R.: Failure of turbine rotor disk of an aircraft engine. *Engineering Failure Analysis*, 9(3):287 – 301, 2002.
7. Bert, C. W. and Paul, T. K.: Failure analysis of rotating disks. *International Journal of Solids and Structures*, 32(89):1307 – 1318, 1995.
8. Shikida, M., Kanayama, Y., and Ohnami, M.: A study on high-speed disk bursting strength. *Bulletin of JSME*, 23(181):1035–1042, 1980.
9. EASA: *CS-E 840 - Rotor Integrity*. Certification Specifications for Engines, 2009.
10. FAA: *FAR 33.27 - Turbine, compressor, fan, and turbosupercharger rotor overspeed*. Federal Aviation Regulations, 2011.
11. Garganese, G.: Analisi elasto plastica per il calcolo della velocità di scoppio dei dischi. Master's thesis, Politecnico di Torino, 2011.
12. Grammel, R.: Ein neues verfahren zur berechnung rotierender schein. *Dinglers Polytechnisches Journal*, (338):217, 1923.
13. Manson, S. S.: Determination of elastic stresses in gas-turbine disks. *NACA Technical Note No. 871*, 1947.
14. Callister, W. and Rethwisch, D.: *Materials Science and Engineering: An Introduction*. John Wiley & Sons, 2010.
15. Hill, R.: *The Mathematical Theory of Plasticity*. Oxford University Press, 1998.

CITED LITERATURE (continued)

16. Ramberg, W. and Osgood, W. R.: Description of stress-strain curves by three parameters. *NACA Technical Note No. 902*, 1943.
17. Weiss, H. and Prager, W.: The bursting speed of a rotating plastic disc. *DTIC Technical Report No. 96*, 1953.
18. Robinson, E.: Bursting tests of steam-turbine disk wheels. *Trans. ASME 66*, page 373, 1944.
19. Waldren, N. E., Percy, M. J., and Mellor, P. B.: Burst strength of rotating discs. In *Proceedings of the Institution of Mechanical Engineers*, volume 180, pages 111–130, 1965.
20. Belingardi, G.: *Il metodo degli elementi finiti nella progettazione meccanica*. Levrotto & Bella, 1998.
21. *Ansys v.11 Manual*.
22. Percy, M., Ball, K., and Mellor, P.: An experimental study of the burst strength of rotating disks. *International Journal of Mechanical Sciences*, 16(11):809 – 817, 1974.
23. Spence, R. B., Lau, S. C., and Brunelle, E. J.: Stress redistribution and instability of rotating beams and disks. *AIAA Journal*, 9(4):758–759, 1971.
24. Tutuncu, N.: Effect of anisotropy on inertio-elastic instability of rotating disks. *International journal of solids and structures*, 37(51):7609 – 7616, 2000.
25. Timoshenko, S. and Goodier, J.: *Theory of elasticity*. McGraw-Hill, 1969.
26. Holms, A. G. and Jenkins, J. E.: Effect of strength and ductility on burst characteristics of rotating disks. *NACA Technical Note No. 1667*, 1948.
27. Gola, M.: *Lecture notes on rotating disks*. Politecnico di Torino, 2012.
28. Bertini, L.: *Lecture notes on computer aided machine design*. Università di Pisa, 2010.
29. Percy, M. and Mellor, P.: Theoretical prediction of tensile instability conditions in rotating disks. *International Journal of Mechanical Sciences*, 6(6):421 – 434, 1964.
30. Barack, W. N. and Domas, P.: An improved turbine disk design to increase reliability of aircraft jet engine. Technical report, NASA CR-135033, 1976.

VITA

NAME: Stefano Chianese

EDUCATION: Alta Scuola Politecnica, Milan, Italy, 2013

M.Sc., Mechanical Engineering, Politecnico di Torino, Italy, 2013

M.Sc. Mechanical Engineering, University of Illinois at Chicago, 2013

B.Sc., Mechanical Engineering, Politecnico di Torino, Italy, 2011

PUBLICATIONS: Cerquitelli, T., Chianese, S., Ferrero Merlino, C., Raimondi, F., Scapecchia, G., Spagnuolo, M., Zolotukhina, I.: Internet technologies to support SME internationalization. In: *Information systems and small and medium-sized enterprises (SMEs): state of art of IS research in SMEs*, eds. J. Devos, H. Van Landeghem and D. Deschoolmeester. Springer, 2013.